

Atoms and Molecules Immersed in a Bose-Einstein Condensate

by

Yiqi Ni

Submitted to the Department of Physics
in partial fulfillment of the requirements for the degree of

Ph.D

at the

MASSACHUSETTS INSTITUTE OF TECHNOLOGY

May 2023

© Massachusetts Institute of Technology 2023. All rights reserved.

Author
Department of Physics
April 15, 2023

Certified by
Martin Zwierlein
Thomas A. Frank (1977) Professor of Physics
Thesis Supervisor

Accepted by
TBD
Chairman, Department Committee on Graduate Theses

Atoms and Molecules Immersed in a Bose-Einstein Condensate

by

Yiqi Ni

Submitted to the Department of Physics
on April 15, 2023, in partial fulfillment of the
requirements for the degree of
Ph.D

Abstract

In this thesis work, I demonstrate the creation of dipolar $^{23}\text{Na}^{40}\text{K}$ molecules in their absolute ground state directly from Bose polarons, which are dressed fermionic ^{40}K impurities immersed in a ^{23}Na Bose-Einstein condensate. In contrast to Feshbach molecules, Bose polarons at negative scattering length are long-lived in the presence of the BEC. We demonstrate direct photoassociation from Bose polarons to electronically excited molecular states, dark resonance spectroscopy of the absolute ground state molecular state, and finally stimulated rapid adiabatic passage (STIRAP) of Bose polarons into the molecular ground state, all in the presence of the Na BEC. This leads to a dense molecular gas at temperatures on the order of 70 nK immersed inside a $T/T_c = 0.1$ BEC.

Thesis Supervisor: Martin Zwierlein
Title: Thomas A. Frank (1977) Professor of Physics

Acknowledgments

Write acknowledgements to Martin, Carsten, Alex, Zoe, Eric, Yiming, Parth....

Contents

1	Introduction	12
1.1	Pathways to ground state molecules	13
1.2	Fermi 1 Apparatus	17
1.3	STIRAP laser system	20
1.3.1	ULE cavity	20
1.3.2	Interference filter diode laser with intra-cavity EOM	22
1.3.3	Frequency doubling bow-tie cavity	24
1.4	Outline	26
2	Bose-Fermi Mixture	27
2.1	Feshbach resonances of $^{23}\text{Na}^{40}\text{K}$	27
2.1.1	Two-body thermalization	28
2.1.2	Feshbach molecule binding energy	30
2.2	Bose polaron Chevy ansatz	33
2.3	Three-body physics	39
2.3.1	Three-body recombination	39
2.3.2	Efimov resonances	42
3	Photoassociation	48
3.1	Analogy to three-body recombination	48
3.2	Franck-Condon description of photoassociation	49
3.3	Photoassociating Feshbach molecules	51
3.3.1	Feshbach molecule photoassociation coupling strength	53

3.4	Photoassociating a quasi-particle	55
3.5	Polaron photoassociation spectrum	55
3.6	Photoassociative linear response	58
3.7	Nonlinear response: continuum participation	60
3.8	Photoassociation enhancement from strong interaction	64
3.9	Inelastic loss rate	65
4	Creating ground state dipolar molecules from Feshbach molecules	69
4.1	Autler-Townes spectroscopy	70
4.2	Dark resonance spectroscopy	71
4.3	Coherent two-photon creation of ground state molecules	75
4.4	Ground state molecule lifetime	78
4.5	Atom removal	81
4.6	STIRAP efficiency	83
5	A new pathway to the dipolar molecule ground state from Bose polarons	88
5.1	Contact is all you need	89
5.2	Single photon dynamics	91
5.3	Dark resonance spectroscopy of polaron	92
5.3.1	Dark resonance spectrum of three transitions	95
5.4	Coherent creation of ground state dipolar molecules inside a BEC . .	96
5.5	Dipolar ground state molecule lifetime inside of a BEC	101
5.6	Outlook	102
5.6.1	Comparison with Feshbach molecule approach	105
5.7	Simple STIRAP model	107
5.7.1	STIRAP in over-damped regime	108
5.7.2	Free-particle continuum influence	111
5.7.3	Polaron to ground state molecule via the triplet-rich excited state	115

6 Outlook	117
6.1 Box trap	117
6.2 Microwave dressing	117
6.3 Down-leg dressing	117
6.4 Molecule microscope	117
A STIRAP Laser System	118
A.1 Pound-Drever-Hall lock	120
A.2 Intra-cavity EOM Interference Filter Lasers	120
B Theoretical description of Bose polaron	121
C Atom calibrations	122
C.1 Boson atom number calibration	122
C.1.1 Gaussian and bimodal fits	123
C.1.2 Temperature calibration	124
C.1.3 Atom number and BEC critical temperature	126
C.2 Fermion atom number	128
C.3 Two component boson density	129
C.4 Local density analysis	130
C.5 Thermal boson line density	131
C.6 Thermal boson column density	132

List of Figures

1-1	Two pathways of creating ultracold ground state molecules.	14
1-2	Molecular impurities dressed by helium droplets.	15
1-3	Creation of cold and ultracold molecules achieved in different regimes.	16
1-4	Optical elements for plug and ODT traps at north side of the science chamber.	18
1-5	Optical elements for creating ground state molecules at south side of the science chamber.	19
1-6	High finesse ULE cavity linewidth measurement.	21
1-7	Interference diode laser design featuring an intra-cavity EOM.	23
1-8	Frequency doubling crystal enhanced by a bow-tie cavity.	24
1-9	Frequency doubling cavity output power and beatnode measurement.	25
2-1	$^{23}\text{Na}^{40}\text{K}$ Feshbach resonance landscape.	29
2-2	Radio-frequency association of $^{23}\text{Na}^{40}\text{K}$ Feshbach molecule.	31
2-3	NaK Feshbach molecule binding energy dependence on magnetic field.	32
2-4	Energy spectrum of Bose polaron from variational ansatz.	36
2-5	Contact and size of Bose polaron from variational ansatz.	38
2-6	Illustration of a three-body recombination event among a fermion and two bosons.	40
2-7	Measurement of $^{23}\text{Na}^{40}\text{K}$ three-body recombination rate from [18]. . .	41
2-8	Efimov energy spectrum and Efimov resonances from [36].	43
2-9	Observation of Efimov resonance via recombination rate minimum. .	45
2-10	Efimov scaling factor vs mass balance.	47

3-1	The three-body recombination analogy to the photoassociation process.	49
3-2	Photoassociation spectroscopy of $^{23}\text{Na}^{40}\text{K}$ Feshbach molecules	52
3-3	$^{23}\text{Na}^{40}\text{K}$ Feshbach molecules photoassociation time dynamics.	54
3-4	Photoassociation spectra of attractively interacting Bose-Fermi mixture.	57
3-5	Photoassociation spectroscopy of attractively interacting $^{23}\text{Na}^{40}\text{K}$ mixture.	59
3-6	Polaron photoassociation linear response of three excited state manifolds.	61
3-7	Polaron nonlinear photoassociation response of attractively interacting Bose polaron.	63
3-8	Photoassociative formation rate γ of attractively interacting polarons and weakly-bound Feshbach molecules.	66
3-9	The loss rate β of attractively interacting polarons and weakly-bound Feshbach molecules.	68
4-1	Autler-Townes spectroscopy of Feshbach molecules.	71
4-2	Observation of ground state molecules using dark resonance spectroscopy	72
4-3	Coherence time measurement via dark state population time dynamics.	74
4-4	Observation of ground state molecule population coherent evolution during the STIRAP ramp.	76
4-5	Two photon resonance spectroscopy of Feshbach molecules.	77
4-6	Ground state molecule lifetime in a dilute boson bath.	79
4-7	Demonstration of efficient ^{23}Na and ^{40}K atoms removal with resonant laser light.	82
4-8	STIRAP efficiency as function of pulse duration.	85
4-9	Observation of STIRAP transfer efficiency as a function of laser powers.	87
5-1	Pathways to the absolute rovibrational ground state molecules.	90
5-2	Polaron photoassociation spectral red-shift.	93
5-3	Polaron photoassociation time dynamics.	94

5-4	Observation of polaron coupling to the absolute ground state via dark resonance spectroscopy.	95
5-5	Dark resonance spectroscopy of the triplet rich manifold.	97
5-6	Dark resonance spectroscopy of the singlet rich manifold.	98
5-7	Down-leg coupling strength relation to optical power.	99
5-8	Relative up-leg and down-leg coupling strength via 3 excited states. .	100
5-9	STIRAP two-photon resonance spectrum of attractively interacting Bose polaron.	102
5-10	Coherent population transfer from strongly interacting Bose polarons to the absolute ground state molecules via two-photon STIRAP. . . .	103
5-11	Dipolar ground state molecule lifetime inside of a BEC.	104
5-12	Typical Feshbach molecule STIRAP with rf association efficiency included.	106
5-13	Time evolution of the three level system during STIRAP.	109
5-14	Damping effects on energy gap at the STIRAP critical moment. . . .	110
5-15	Dressed state energy evolution during STIRAP ramp in the over-damped regime.	112
5-16	Free-particle continuum participation during STIRAP.	113
5-17	Dressed state energy gaps in relation with single photon detuning. .	114
5-18	STIRAP time evolution from strongly interacting Bose polarons to ground state molecules via the triplet-rich excited state.	116
A-1	PDH lock optical and electronics schematics.	119
A-2	STIRAP laser error signal power spectrum.	120
C-1	First Gaussian fit to ^{23}Na	123
C-2	Second Gaussian fit to ^{23}Na	124
C-3	Final bimodal fit to ^{23}Na	125
C-4	Measurement of ^{23}Na temperature from thermal wing.	126
C-5	Onset of the BEC amplitudes near condensate transition temperature T_c	127

C-6	On set of the BEC amplitudes near condensate transition temperature.	128
C-7	Calibration fermion and bosons atom number.	129
C-8	Density distribution of two component boson model.	131
C-9	Local density analysis.	132
C-10	Thermal boson density distribution.	133
C-11	134
C-12	134
C-13	135

List of Tables

2.1	Feshbach resonance positions B_0 and resonance width Δ_B between $\text{Na} 1,1\rangle$ and $\text{K} 9/2,-7/2\rangle$. $a_{bg} = -710 a_0$ is the inter-species background scattering length.	29
2.2	Feshbach resonance positions B_0 and resonance width Δ_B between $\text{Na} 1,1\rangle$ and $\text{K} 9/2,-9/2\rangle$. $a_{bg} = -730 a_0$ is the background inter-species scattering length.	29
3.1	Experimental parameters for polaron photoassociation spectroscopy.	58
3.2	Summary of fit results shown in Fig. 3-7. Numbers in the parenthesis are standard deviations of fit results from 4 detunings.	62
5.1	List of recent experiments on converting Bose-Fermi mixtures to ground state molecules.	107

Chapter 1

Introduction

Atomic, molecular, and optical (AMO) physicists strive for precise control of quantum interactions. Quantum degeneracy realized by cooling atoms to ultracold temperature regime is an acclaimed example. This breakthrough in ultracold atoms has produced many renowned experiments, including bosons undergoing a Bose-Einstein condensate (BEC) phase transition, the crossover between Bardeen-Cooper-Schrieffer (BCS) and BEC in two-component fermions, and the transition from a superfluid to a Mott insulator state with atoms trapped in an optical lattice. Applying high numerical aperture objectives onto these experiments achieves single particle resolution and pushes the AMO experiments to a new height. Nevertheless, neutral alkali atoms typically have point-like s-wave interactions that are elegantly captured by Tan's contact description.

Dipolar molecules present a unique platform to realize long-range anisotropic interactions that are beyond the simple contact description. Neutral dipolar molecules are highly scalable with on-demand dipolar interactions, in contrast to ions which have relatively low density due to the always-on Coulomb interaction [23]. Dipolar molecules have large interaction energy: orders of magnitude larger than highly magnetic atoms due to the nature of electric and magnetic dipole interaction ($(\frac{1 \text{ Debye}}{1 \text{ Bohr magneton}} \times c)^2 \approx 10^4$). Comparing to highly excited Rydberg atoms, isolated dipolar molecules have much longer lifetime which is a crucial ingredient to realize many body system with new types of novel orders [12].

Bringing dipolar molecules into the realm of quantum degeneracy has been a decades-long endeavor for AMO experimentalists. Each milestones in achieving lower temperature and higher phase-space density brought opportunities in atomic physics, like realizing non-trivial many-body systems [8] and improving precision metrologies [51]. The ongoing progress in cooling molecules to lower temperature are creating a similar wealth of opportunities [10]. Dipolar molecules, sometimes called ‘physicist’s molecule’, are the simplest molecules consisting of two heterogeneous atoms. However, even in their simplest format, cooling molecules is a challenging task. Unlike alkali atoms that have nearly closed optical transitions, molecules possess rich rotational and vibrational states associated to each electronic potential. Such rich rovibrational structures make direct laser cooling of molecules challenging: excited molecules can relax to many lower-lying rovibrational states, which can lead to escape from the desired optical transition loop. Certain types of molecules have semi-closed optical transitions which make them ideal for direct laser cooling with helps of many ‘repump lasers’, which rescue escaped molecules by ‘repumping’ them back to cycling states [74]. The recent state-of-art experiment on direct laser cooling of CaF molecules reaches phase-space density around 10^{-9} at 0.35 mK temperature [2], after which molecules are subsequently loaded into optical tweezers for further quantum controls [3]. Many other approaches to molecule cooling like buffer gas cooling [41] and Stark deceleration [73] are being developed, but these methods result molecule phase-space density far away from achieving quantum degeneracy.

1.1 Pathways to ground state molecules

So far, the most successful strategy in achieving high phase-space density molecules in ultracold temperature regime is to leverage cooling techniques developed for alkali atoms as much as possible. Fig. 1-1a demonstrates 3-step ground state molecule creation via Feshbach molecules: 1) create ultracold atomic mixture, 2) associate the free atom pairs in the mixture to weakly-bound Feshbach molecules, 3) coherently transfer weakly-bound molecules into the absolute rovibrational ground state

molecules via a two-photon Raman process protocol called stimulated rapid adiabatic passage (STIRAP). Chapter 4 in this thesis follows this strategy to create fermionic dipolar molecules that are made of bosonic ^{23}Na and fermionic ^{40}K . Association of weakly-bound molecule via Feshbach resonances have limited efficiency which usually imposes a limiting factor. Moreover, weakly-bound Feshbach molecules have rapid loss rate with surrounding atoms due to three-body recombination, which makes creating ground state molecules inside a BEC extremely challenging. Chapter 5 employs a new pathway that directly create ground state molecules from the strongly interacting Bose-Fermi mixture. Shown in Fig. 1-1b, ground state molecules are directly created from the strongly interacting Bose-Fermi mixture, bypassing the weakly-bound Feshbach molecule association stage.

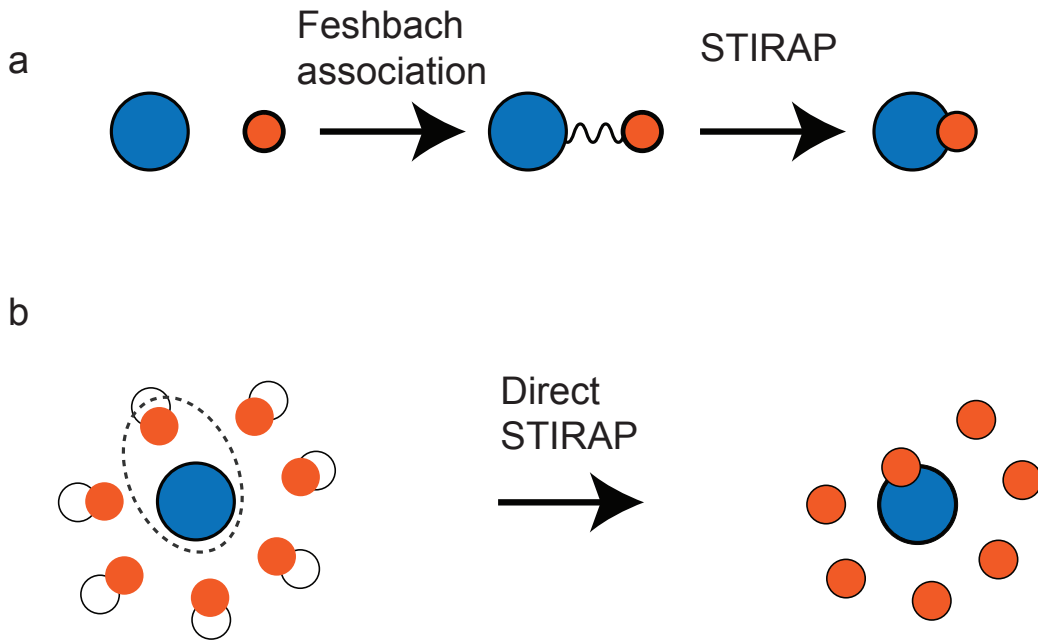


Figure 1-1: Two pathways of creating ultracold ground state molecules. a. The most common method for bi-alkali experiments involves the association of free atom pairs to weakly-bound Feshbach molecules via Feshbach resonances. Subsequent STIRAP pulses coherently convert Feshbach molecules to ground state molecules. b. A new pathway of producing ground state molecule directly from strongly interacting Bose-Fermi mixture. The ground state molecules are immersed inside dense bosonic bath, creating opportunities for studying molecule interactions with the bath.

The ground state molecules are immersed inside a BEC as a result of direct STIRAP transfer, which opens up a new opportunity realize dipolar molecules interacting with a highly quantum degenerate bath. Previous experiments have trapped molecules inside helium nano-droplets, creating a cold environment at a temperature of approximately 0.1 K. As shown in Fig. 1-2, the presence of a superfluid helium bath significantly alters the rotational spectrum of a molecule, and this alteration depends on the fermionic or bosonic nature of the bath. In [48], the authors present a quantum many-body approach that simplifies the understanding of this rotational constant dressing. However, realizing angulon at single quantum level requires creating molecules at ultracold temperature. Fig. 1-3 summarizes the existing

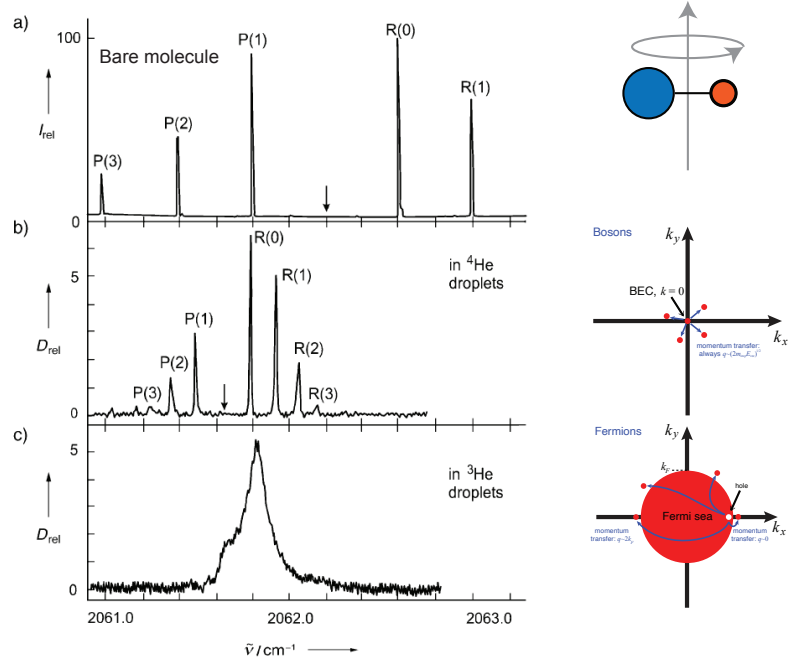


Figure 1-2: Molecular impurities dressed by helium droplets. Figure contents are adapted from [78] and [48]. a. Bare molecule rotational spectrum. In rigid rotor model, molecule rotational spectrum are describe by $E_J = \hbar B_{rot} J(J + 1)$, where B_{rot} is the molecule rotational constant related to the molecule moment of inertial I : $B_{rot} = \frac{\hbar^2}{2I}$. b. Rotational spectrum of molecules immersed inside bosonic ${}^4\text{He}$, and c. inside fermionic ${}^3\text{He}$. The rotational spectrum are drastically changed due to the rotation constant dressing by the background helium bath, which depends its fermionic or bosonic statistics.

molecule cooling schemes and highlights that the Bose polaron+STIRAP pathway brings dressed molecule impurity physics into ultracold temperature regime.

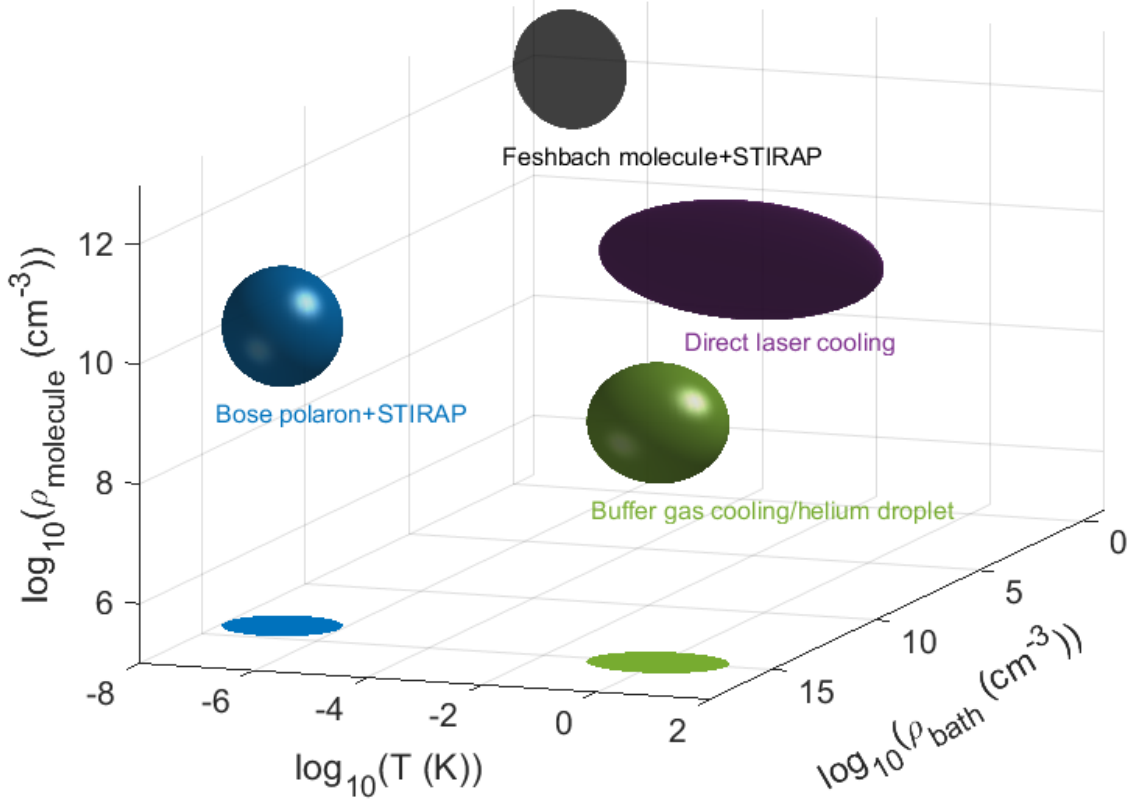


Figure 1-3: Creation of cold and ultracold molecules achieved in different regimes. The vertical axis of the plot indicates the molecule density $\rho_{molecule}$; the horizontal axes indicate the molecule temperature T, and the surrounding bath density ρ_{bath} . Creating molecules via STIRAP (shown in gray and blue spheres) is currently the only method that has successfully produced molecules in the quantum degenerate regime. Buffer gas cooling (shown in green) is a common method that uses helium as a buffer medium to cool molecules to around 0.1-1 K. Some molecules can be directly laser cooled (shown in purple), typically after initial buffer cooling. For instance, recent state-of-the-art experiments with CaF molecules have reached temperatures of approximately $350 \mu\text{K}$ from a magneto-optical trap [2], which can be further cooled down to around $10 \mu\text{K}$ inside optical tweezers [3].

1.2 Fermi 1 Apparatus

Fermi 1 is built as a versatile machine for multiple-species mixture experiments. Our apparatus can be divided into 3 segments: the Na oven chamber, the K oven chamber, and the science chamber. Fig. ?? and ?? demonstrate two Zeeman slowers connect potassium and sodium oven chambers to the science chamber. As the first-stage cooling, Zeeman slowers produce high density fluxes of ^{23}Na and ^{40}K atom that are captured in a magneto-optical trap (MOT) in the science chamber. ^{23}Na and ^{40}K atoms are subsequently loaded into a ‘plug trap’, which is a linear magnetic trap whose center is ‘plugged’ by a 532 nm laser, which provides repulsive potentials for both species to avoid ‘Majorana losses’. During this second-stage cooling, hot ^{23}Na atoms are selectively removed from the trap via radio-frequency knife, which evaporatively cools ^{23}Na atoms themselves, and sympathetically cools ^{40}K atoms. The magnetic trap evaporation complete before ^{23}Na atoms form a BEC to avoid rapid three-body losses among $^{23}\text{Na}^{40}\text{K}$ mixture. The mixture is transferred into a crossed optical dipole trap (ODT) for the third-stage evaporative cooling by lowering the ODT trap depth. We apply a uniform magnetic field of 60 G to induce inter-species scattering length of $+500 a_0$ during the 10 s ODT cooling, which optimizes the ODT cooling efficiency. Since the trapping potential of ^{40}K atoms is deeper than that of ^{23}Na in the 1064 nm ODT, we have experimentally found that the number of ^{40}K atoms is minimally affected during the ODT cooling process. After the final stage of cooling in the ODT, the quantum degenerate Bose-Fermi mixtures are ready for further scientific explorations that are described in detail in later chapters. Fig. 1-4 shows the simplified optical elements that enable the magnetic trap plug and optical trapping of the mixture. Fig. 1-5 illustrates the optical elements for STIRAP, which are located on the south side of the experiment chamber. We dedicate the next section for a new STIRAP laser source that will power future molecule creation in Fermi 1.

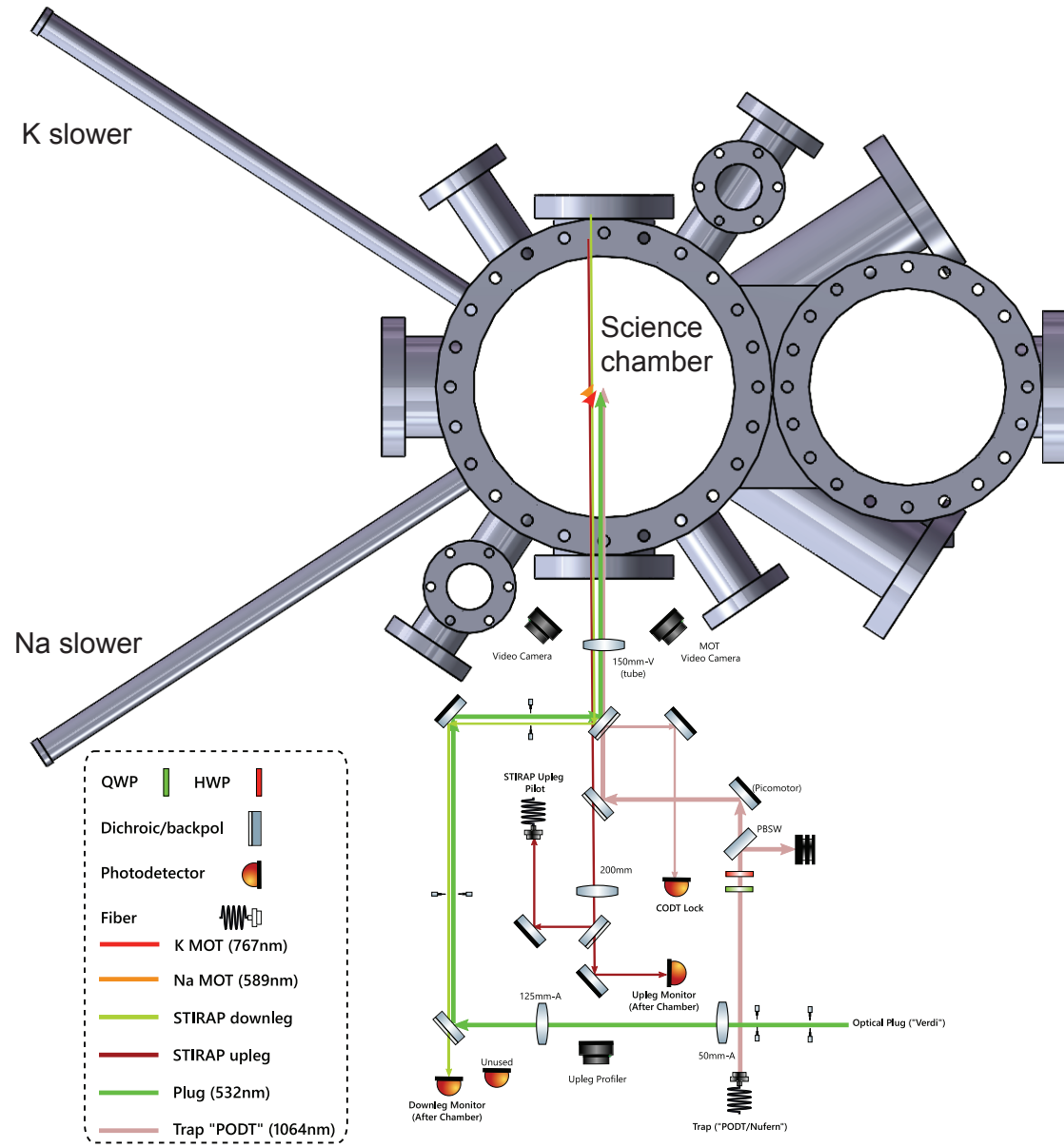


Figure 1-4: Optical elements for plug and ODT traps at north side of the science chamber. Photo credit to Yiming and Alex.

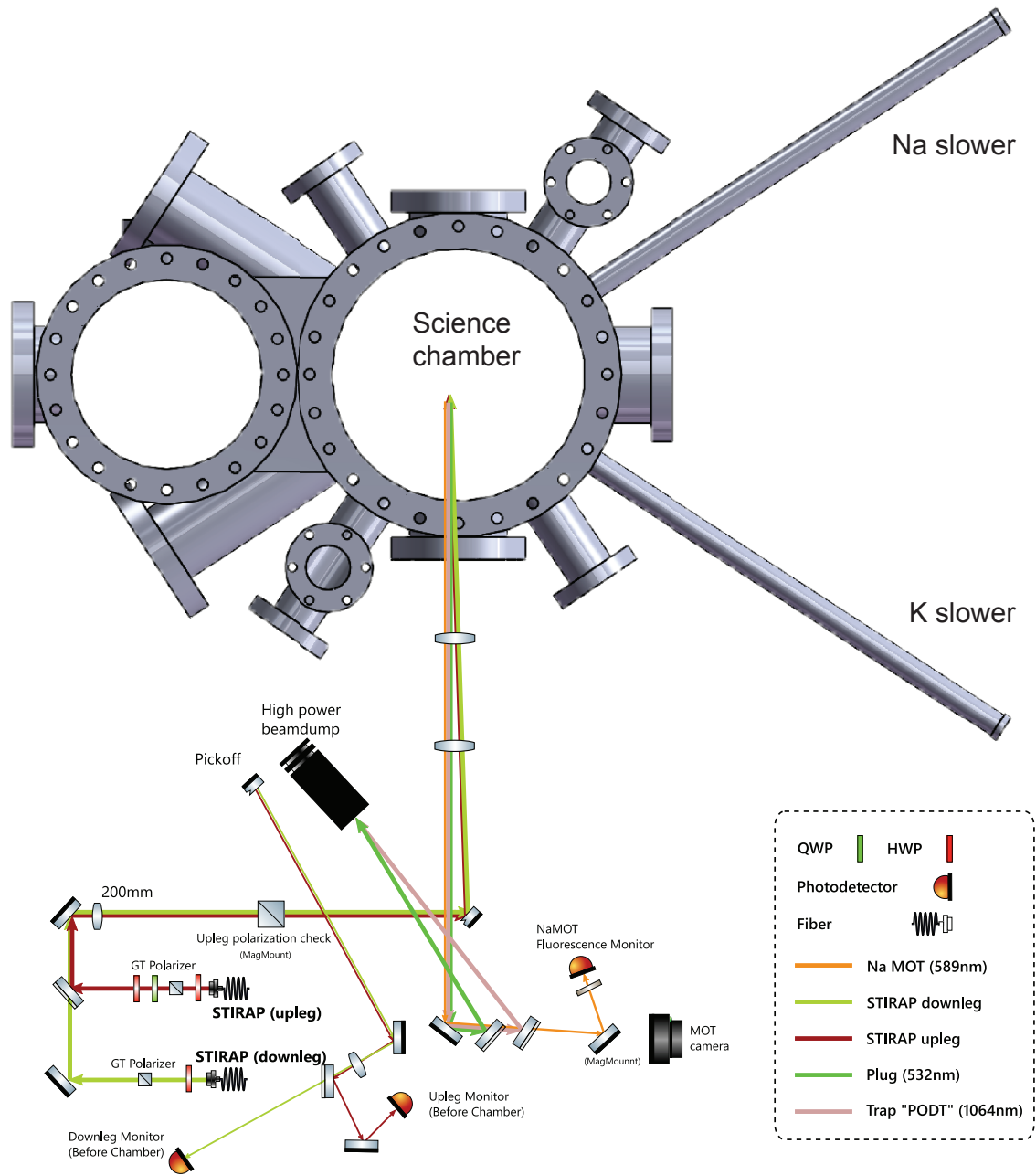


Figure 1-5: Optical elements for creating ground state molecules at south side of the science chamber. Photo credit to Yiming and Alex.

1.3 STIRAP laser system

The coherence of the laser is one of the most crucial factors in achieving high transfer efficiency in optical adiabatic population transfer techniques, such as STIRAP. $^{23}\text{Na}^{40}\text{K}$ ground state molecules have $\hbar \times (156.251 \text{ THz})$ binding energy [56]. The frequency difference between the up-leg and down-leg lasers facilitates the STIRAP transfer and bridges the large energy gap between free atom pairs and $^{23}\text{Na}^{40}\text{K}$ ground state molecules. A successful STIRAP transfer requires both absolute laser frequency accuracy and relative phase coherence between the up/down-leg lasers. To satisfy these two stringent requirements, we employ a high-finesse ultra-low expansion (ULE) cavity.

1.3.1 ULE cavity

The ultra-low expansion (ULE) cavity, which has high reflective cavity mirrors, acts as a precise and stable ‘ruler’ that lasers can reference to. We character the ULE cavity manufactured by Stablized Laser System, which consists of a cylindrical cavity assembly (ATF-6010-4) hosted in a special vacuum housing (VH6010-4). Fig. 1-6 inset illustrates the schematic for the ULE cavity linewidth measurement. Half of the incident 1134 nm probe beam, shown in black, is split to the reference photodiode shown in orange, while the other half is used for locking the laser to the ULE cavity via Pounder-Drever-Hall (PDH) technique. The probing laser locked to the ULE leads to the maximum transmission of the ULE cavity, which is measured by the transmission photodiode shown in blue. At time $t = 0$, the probe beam is switched off and reference photodiode signal rapidly drops to 0 in time scale limited by the optical switch speed and photodiode response. Meanwhile the ULE transmission light is observed to have a much slower decay with exponential constant $\tau_{ULE} = 4 \mu\text{s}$, which corresponds to the ULE cavity linewidth of $(2\pi)41 \text{ kHz}$. This 1134 nm light comes from our new diode laser design, which will be frequency doubled to replace the previously used dye laser.

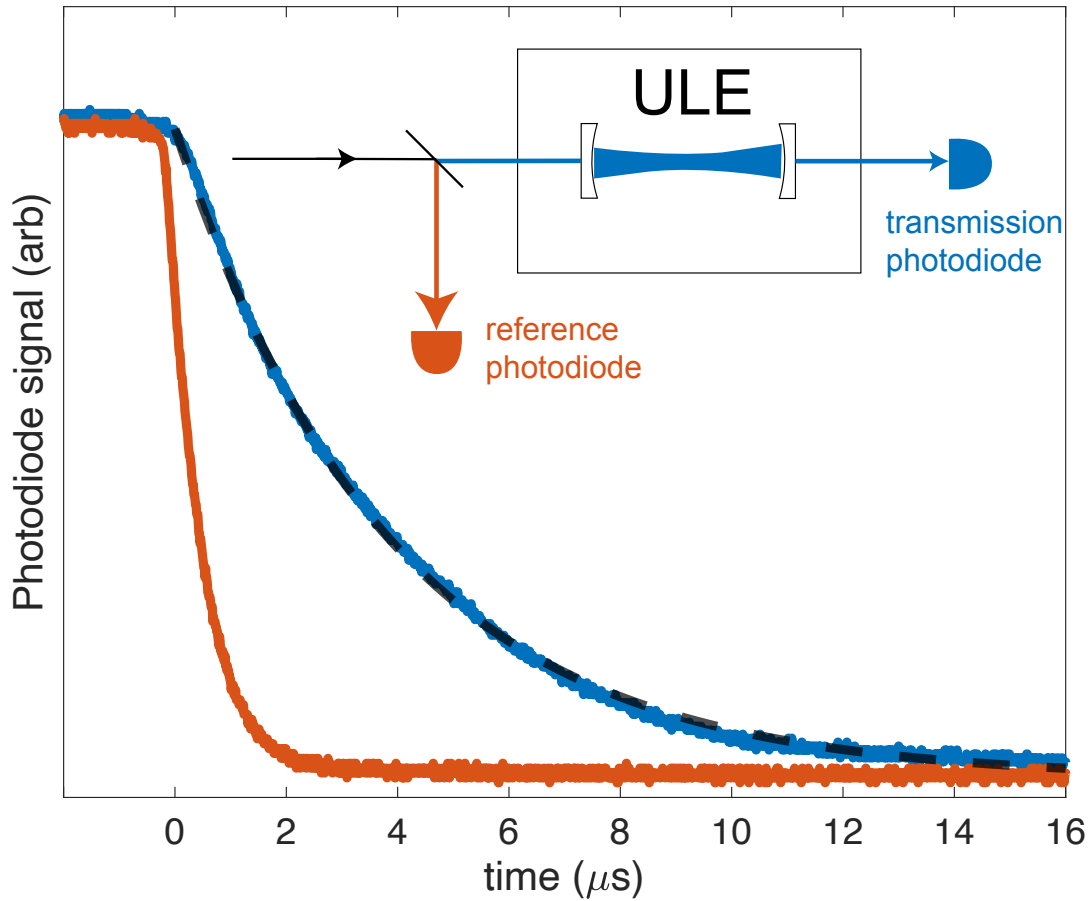


Figure 1-6: High finesse ULE cavity linewidth measurement. The incident 1134 nm wavelength laser is split into two paths: half of the light goes directly into a reference photodiode; another half of the light goes into the ULE cavity whose transmission light is measured on the transmission photodiode. The laser is initially ($t < 0$) locked to the ULE cavity, therefore the ULE almost fully transmits the incident light. The light field is switched off at $t = 0$. The reference photodiode signal, shown in orange, goes down to 0 in the time scale given by the photodiode and optical shutter response. Meanwhile, the transmission photodiode signal, shown in blue, measures a slow decay signal due to light field that is built up inside of the high-finesse ULE cavity. The transmission photodiode signal is fitted with an exponential decay function $V = V_0 e^{-\tau_{ULE} t}$, which yields $\tau_{ULE} = 4 \mu\text{s}$, and ULE cavity linewidth $\delta\omega_{ULE} = 1/\tau_{ULE} = (2\pi)41 \text{ kHz}$.

1.3.2 Interference filter diode laser with intra-cavity EOM

Up-leg and down-leg coupling for previous ground state molecule experiments at Fermi 1 were achieved using a M-square titanium-sapphire laser and a Coherent 899 ring dye laser. The Coherent 899 ring dye laser serves as a robust down-leg light source that couples the electronically excited state and the ground state. Its wide wavelength range and high power were instrumental in the initial search for $^{23}\text{Na}^{40}\text{K}$ ground state molecules at Fermi1 [56, 57]. However, periodic maintenance such as dye changes and cleaning of the dye circulator are required for its operation. We are introducing a new diode laser solution to replace the dye laser, which reduces the laser footprint and requires much less maintenance overhead than the dye laser. We use a 1134 nm quantum dot laser diode (Innolume GC-1160-90-TO-200-A) as a fundamental light source, which is locked to the ULE cavity, to address the inconveniently located 567 nm down-leg transition that lacks a direct diode laser solution. The 1134 nm laser is then fed into a frequency doubling bow-tie cavity that efficiently produces the 567 nm light required for molecule creation. The quantum dot diode has a frequency-phase lag issue in the current modulation, which presents a challenge for locking the laser to the ULE cavity by actuating the diode current. To circumvent this issue, we place an intra-cavity electro-optical modulator (EOM) inside the diode laser feedback mechanism. The EOM has a flat frequency-phase response from DC to 500 kHz, making it an ideal laser locking actuator. The EOM (Qubig EO-DC-5M-BC) has a special Brewster angle cut at both facets to avoid unwanted interference inside the EOM crystal. The laser cavity becomes considerably longer than typical grating diode lasers by the EOM addition. To ensure single-mode laser operation, we introduce an interference filter (Omega Optical 3065481) as a coarse frequency selector. The filter has a 0.1 nm FWHM filter width with >80% transmission. As shown in Fig. 1-7, the interference filter is mounted on a low-thermal profile 1/2" mirror mount (Newport ST05-F2H) at an angle of approximately 6 degrees. By tuning the interference filter angle, a lasing wavelength range of 1132 to 1136 nm can be achieved. As the laser cavity output coupler, a backside-polished mirror (Thorlabs BB1-E02P), that reflects

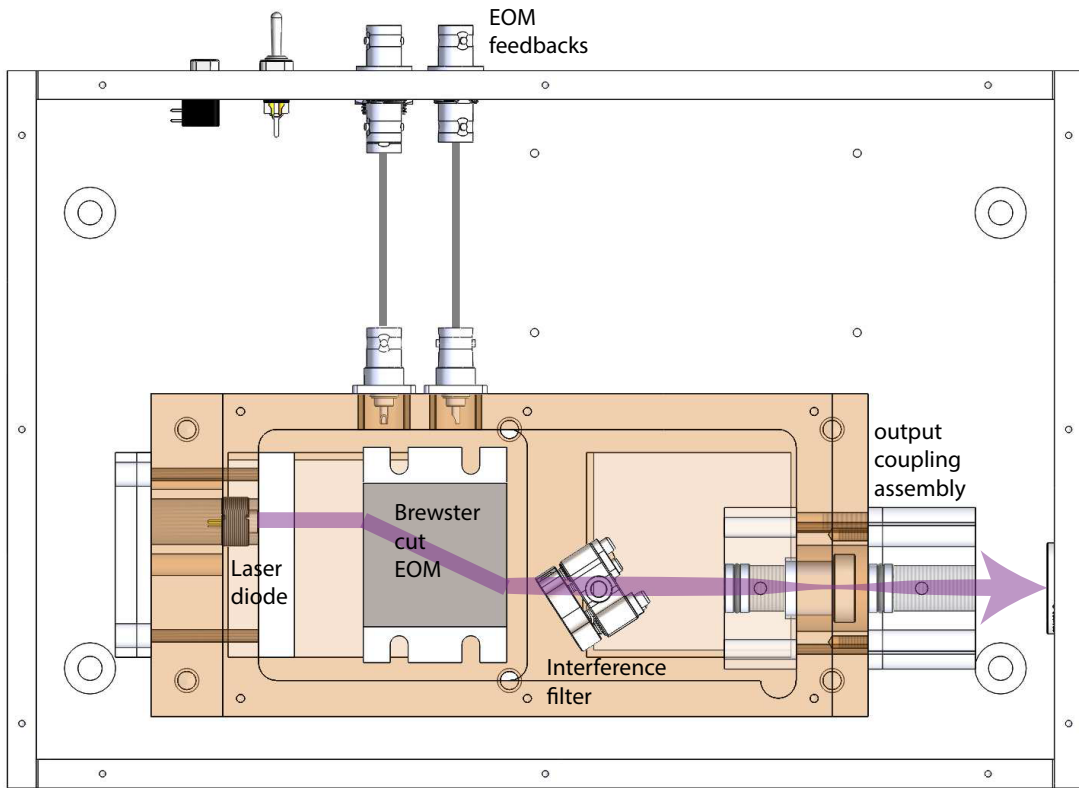


Figure 1-7: Interference diode laser design featuring an intra-cavity EOM. The laser cavity, shown in brown, is milled from a single-piece high-tensile brass block (CW704R). The laser cavity has Thorlabs SM-05 threads for easy installation of commercial components from Thorlabs. The collimated laser diode outputs enter the intra-cavity EOM, which has Brewster angle cuts on both facets. A low thermal profile mirror mount (Newport ST05-R2H) holds the interference filter, which provides coarse lasing wavelength selection. The output coupling assembly consists of a pair of cat-eye lenses and a back-polished mirror that is glued to a ring piezo. The back-polished mirror reflects approximately 15% of the 1134 nm light, providing laser cavity sufficient feedback for lasing. The ring piezo is a low-frequency (< 1 kHz) actuator that changes the laser cavity length.

back approximately 15% power, is placed in the middle of a cat-eye lens pair. The output coupler mirror is attached to a ring piezo, which serves as the laser lock actuator at low frequency range (< 1 kHz). Two electrodes are attached to the intra-cavity EOM for independent laser phase actuation. We have experimentally found that feedback on a single EOM electrode is sufficient to achieve sub-kHz laser linewidth. The 1134 nm diode laser, which has an output power of 40 mW with 320

mA current drive, is used as the input for the frequency doubling cavity.

1.3.3 Frequency doubling bow-tie cavity

Shown in fig. 1-8, the 1134 nm to 567 nm frequency doubling is achieved by a KNbO₃ non-linear crystal manufactured by LEOS solutions, which is located inside a bow-tie cavity to enhance the frequency doubling efficiency. The non-linear crystal's temperature is actively stabilized at 57 °C for achieving critical phase matching. The bow-tie cavity has four mirrors, highly reflective for the 1134 nm fundamental light, and only the output coupling mirror is highly transmissive for the frequency doubled 567 nm light. The 40 mW of 1134 nm light generates 4 mW of 567 nm light, which is

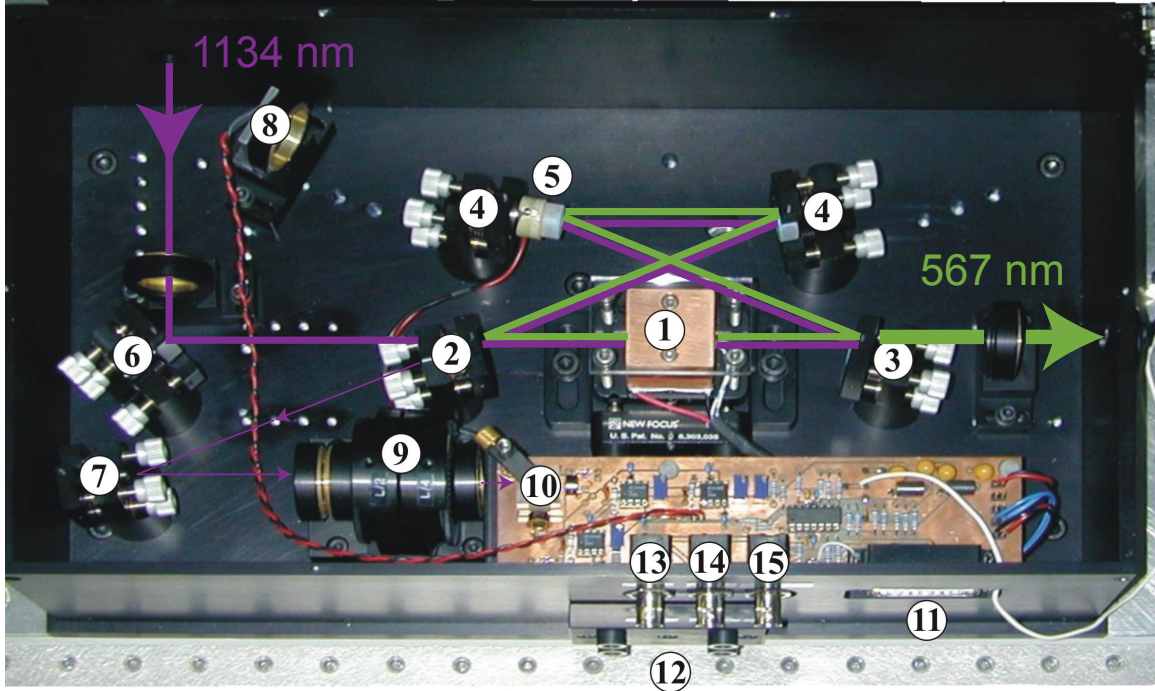


Figure 1-8: Frequency doubling crystal enhanced by a bow-tie cavity. Image is adapted from the LEOS manual. The non-linear crystal is placed inside a temperature-controlled housing, shown in ①. The bow-tie cavity is formed by four mirrors, shown in ②③④, that build up the fundamental 1134 nm light field to enhance the frequency doubling efficiency. The output coupling mirror ③ has high transmission for the frequency doubled light, allowing it to exit the cavity and be used for molecule creations. The cavity length is actively stabilized from actuating the piezo shown in ⑤ to ensure maximum laser power output using the Hänsch–Couillaud lock technique.

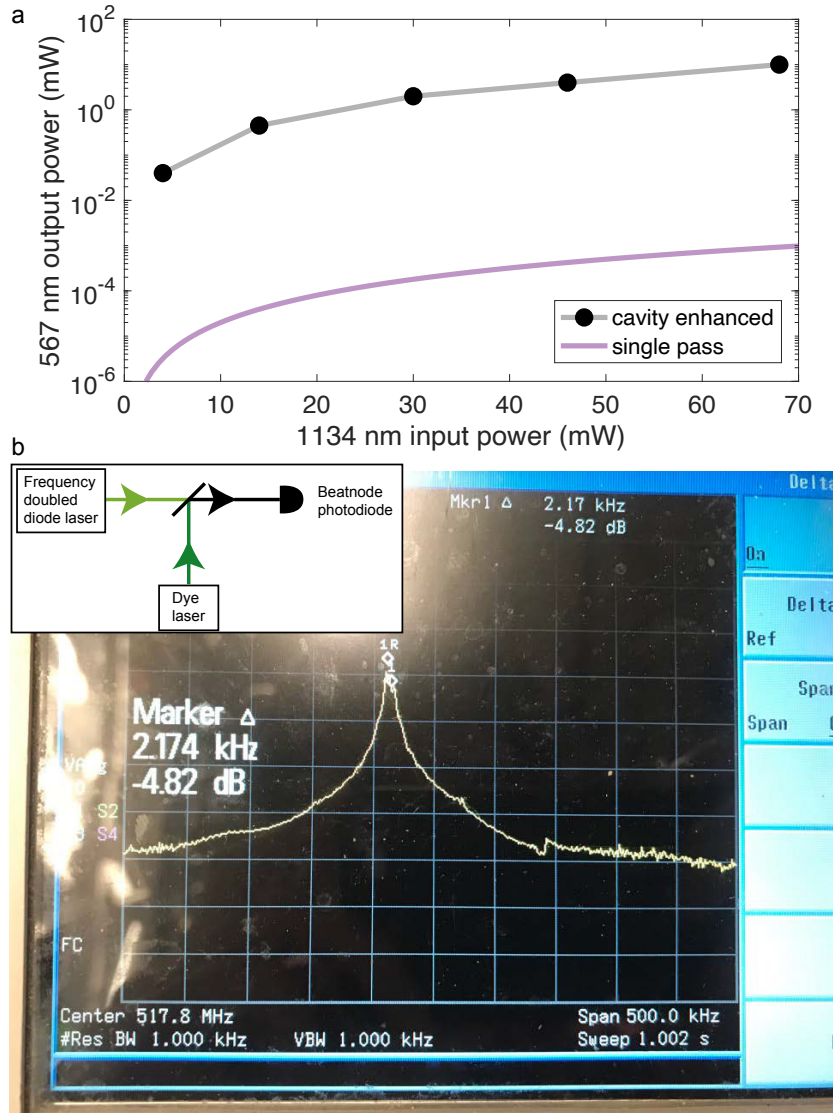


Figure 1-9: a. Frequency doubling cavity output power. The bow-tie cavity significantly enhances the non-linear crystal's frequency doubling efficiency, increasing it by almost five orders of magnitude at the diode laser output power range. The black dots on the graph represent the measured cavity-enhanced output power at 567 nm relative to the input power at 1134 nm. The purple line corresponds to the non-linear crystal's single-pass efficiency, which is $\eta_{1pass} = 2 \times 10^{-4} \text{ W}^{-1}$. b. Beatnode measurement between the frequency doubled diode laser and dye laser. Two 567 nm light sources that are derived from the dye laser and frequency doubled diode laser are overlapped onto the beatnode photodiode. The resulting beatnote signal is measured on a radio-frequency analyzer and found to be centered at 517.8 MHz with a 3 dB linewidth of less than 2 kHz. This narrow linewidth is a remarkable achievement, given that the 1134 nm diode laser and dye laser are completely uncorrelated and are locked to two different ULE cavities located on separate optical tables. This result demonstrates the highly effective active laser frequency stabilization employed in our experiments.

sufficient to produce strong down-leg coupling strength for STIRAP. To cross-check the new 567 nm light source coherence, we produce a beatnode signal of the dye laser and the new light source, which are locked to two independent ULE cavities. Fig. 1-9 shows that the beatnode signal has a < 2 kHz 3 dB linewidth. The beatnode signal linewidth is mainly limited by the dye laser lock noise, proving the feasibility of creating ground state molecules with the new diode laser solution.

1.4 Outline

Chapter 2 provides an overview of the collisional properties of the $^{23}\text{Na}^{40}\text{K}$ system, starting with the two-body elastic collisions induced by Feshbach resonances between lowest hyperfine states, followed by the inelastic collisions caused by three-body recombination that lead to Efimov-related physics. Chapter 2 concludes with a description of a single Chevy ansatz, which elegantly describes the strongly interacting Bose-Fermi mixture with the Bose polaron quasi-particle picture. In Chapter 3, we discuss the photoassociation of Feshbach molecules and attractively interacting Bose polaron. The participation of the free-particle continuum strongly influences the Bose polaron quasi-particle photoassociation response. Chapter 4 demonstrates the traditional pathway of creating ground state molecules, starting from Feshbach molecules. We use technical tools to diagnose and identify limiting factors of ground state molecule creation, from our laser systems to ambient noises. In Chapter 5, we introduce a new pathway of creating ground state molecules directly from attractively interacting Bose polaron, which is a pioneering work presented in this thesis. Finally, Chapter 6 presents conclusions and outlooks for the Fermi 1 molecule work.

Chapter 2

Bose-Fermi Mixture

In this chapter, we will explore the importance of tunable interactions between ultracold quantum gases in realizing non-trivial many-body systems, particularly in the case of the ^{23}Na - ^{40}K mixture. The hyperfine ground states of bosonic ^{23}Na and fermionic ^{40}K exhibit rich Feshbach resonances, providing essential tools to control the inter-species interactions. Notably, when fermions are at the impurity limit, the Bose-Fermi mixture can be described in terms of Bose polaron quasi-particle. Strong elastic interactions among bosons and fermions also give rise to inelastic collisions caused by three-body recombinations. Specifically, two bosons and a fermion can form a trimer that modulates the inelastic collision rate and influences the Bose polaron quasi-particle self energy.

2.1 Feshbach resonances of $^{23}\text{Na}^{40}\text{K}$

Previously Fermi 1 reported the Feshbach resonance between $\text{Na}|1, 1\rangle$, $\text{K}|9/2, -5/2\rangle$ in detail [83]. In this section, we focus on the Feshbach resonance between $\text{Na}|1, 1\rangle$, $\text{K}|9/2, -7/2\rangle$ and $\text{K}|9/2, -9/2\rangle$. The hyperfine state $\text{K}|9/2, -9/2\rangle$ has the desired optical cycling transitions, making it an ideal state for absorption imaging. We characterize the Feshbach resonance of $^{23}\text{Na}^{40}\text{K}$ using two separate methods: two-body thermalization [81] and radio-frequency (RF) association spectroscopy to measure the Feshbach molecule binding energy.

2.1.1 Two-body thermalization

We prepare the ^{23}Na - ^{40}K Bose-Fermi mixture in the 1064 nm optical dipole trap at a temperature of approximately 100 nK, with bosonic ^{23}Na above the condensate temperature. After ramping the magnetic field to the value of interest, we apply a short optical pulse at 790 nm that is near-resonant with the ^{40}K atoms but far detuned from the ^{23}Na atoms. This optical pulse preferentially heats up the ^{40}K atoms without perturbing the temperature of the ^{23}Na atoms. After the mixture goes through a fixed thermalization time, we measure the width of the ^{40}K cloud, which is proportional to its temperature. The large inter-species scattering length induces fast thermalization between ^{23}Na and ^{40}K , resulting in a smaller ^{40}K cloud width. The two-body thermalization method has the advantage of avoiding complications from atom number loss due to inelastic collisions. We use a phenomenological model that incorporates overlapping resonances to describe the inter-species scattering length. Although not a precise description, this model provides an adequate approximation [20].

$$a(B) = a_{bg} \prod_{i=1}^N \left(1 + \frac{\Delta_{B_i}}{B - B_{0i}}\right) \quad (2.1)$$

a_{bg} represents the background scattering length, B_{0i} denotes the resonance position, and Δ_{B_i} is the corresponding resonance width. The scattering length of the system reaches a maximum value at the magnetic field B_0 , and reaches zero at $B_{zero} = B_0 + \Delta_B$. To determine the scattering length, we assigned the magnetic field where the highest thermalization rate is observed to B_0 , and the magnetic field where the slowest thermalization rate was observed to B_{zero} . Feshbach resonance parameters between $\text{Na}|1, 1\rangle$ and $\text{K}|9/2, -7/2\rangle$ are summarized in Table 2.1, while the $\text{Na}|1, 1\rangle$ and $\text{K}|9/2, -9/2\rangle$ resonances are summarized in Table 2.2. Fig. 2-1 shows the overlapping Feshbach resonance landscape, which is a powerful tool for realizing Bose-Fermi many-body systems in Fermi 1.

B_0 (G)	81.65	90.4	110.3
Δ_B (G)	0.3	6.5	17.05

Table 2.1: Feshbach resonance positions B_0 and resonance width Δ_B between $\text{Na}|1, 1\rangle$ and $\text{K}|9/2, -7/2\rangle$. $a_{bg} = -710 a_0$ is the inter-species background scattering length.

B_0 (G)	78.35	89.8
Δ_B (G)	5.8	9.55

Table 2.2: Feshbach resonance positions B_0 and resonance width Δ_B between $\text{Na}|1, 1\rangle$ and $\text{K}|9/2, -9/2\rangle$. $a_{bg} = -730 a_0$ is the background inter-species scattering length.

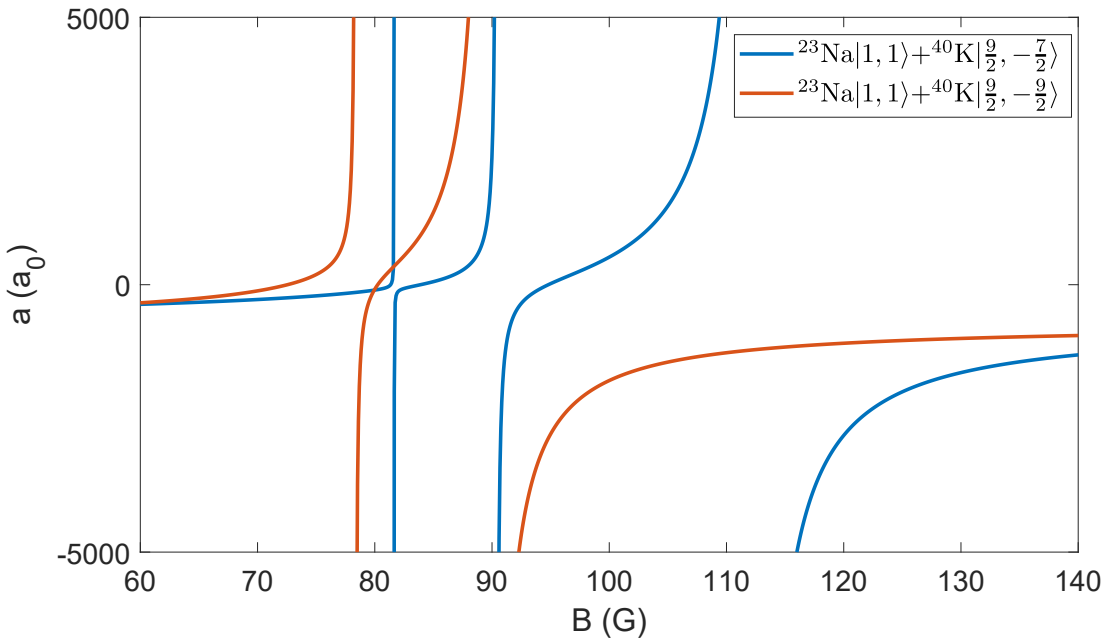


Figure 2-1: $^{23}\text{Na}^{40}\text{K}$ Feshbach resonance landscape. The two lowest ^{40}K hyperfine ground states $|9/2, -7/2\rangle$ (in blue) and $|9/2, -9/2\rangle$ (in orange) have rich Feshbach resonances with $^{23}\text{Na}|1, 1\rangle$ in an experimentally accessible magnetic field range. Typically, we set the magnetic field at 60 G during ODT evaporation to induce a negative inter-species scattering length of $-500 a_0$. We often prepare the mixture at the magnetic field of 80.3 G, which corresponds to the nearly overlapping zero crossing of the inter-species scattering length, because it offers the advantage of stability between $^{40}\text{K}|9/2, -7/2\rangle$ and $|9/2, -9/2\rangle$ with $^{23}\text{Na}|1, 1\rangle$. In this thesis work, we commonly use the 78.35 G Feshbach resonances to create a strongly interacting Bose-Fermi mixture. We typically use 80 to 90 G region to create $^{23}\text{Na}|1, 1\rangle+|9/2, -9/2\rangle$ Feshbach molecules, and 100 to 110 G region to create $^{23}\text{Na}|1, 1\rangle+|9/2, -7/2\rangle$ molecules.

2.1.2 Feshbach molecule binding energy

Feshbach molecules are weakly-bound molecules unique to ultracold quantum gases. These weakly-bound molecules emerge near a Feshbach resonance, and extend to positive scattering length and gains binding energy. There are various methods for creating and detecting Feshbach molecules. Two common methods are magnetic field sweep through a Feshbach resonance and radio-frequency (rf) association. In our experiments, we utilize the rich pattern of inter-species Feshbach resonances shown in Fig. 2-1 and associate Feshbach molecules via rf association, which has the advantage of producing a background-free signal. To create ^{40}K $|9/2, -9/2\rangle$ Feshbach molecules, we use a Landau-Zener rf pulse to transfer all ^{40}K atoms into its $|9/2, -7/2\rangle$ state at 80.3 G. We then rapidly ramp the magnetic field to the final value, with a 5 ms wait time before applying the molecule rf association pulse. Fig. 2-2 demonstrates the rf association of Feshbach molecules with a binding energy of $E_b/h = -80$ kHz at a magnetic field of 85.7 G. The atomic peak centers at $\nu_{rf} - 22.846$ MHz = 0, which is related to the transfer of ^{40}K hyperfine state from $m_F = -7/2$ to $-9/2$, providing a precise calibration of the magnetic field. The second peak at a higher rf frequency indicates the weakly-bound Feshbach molecular state that has lower energy than the free atomic ^{40}K $|9/2, -9/2\rangle$ state.

Fig. 2-3 summarizes the dependence of Feshbach molecule binding energy on magnetic field. Fig. 2-3a shows molecules formed from the ^{23}Na $|1, 1\rangle + ^{40}\text{K}$ $|9/2, -9/2\rangle$ state, and Fig. 2-3b shows molecules formed from the ^{23}Na $|1, 1\rangle + ^{40}\text{K}$ $|9/2, -7/2\rangle$ state. The binding energy dependence on energy is captured by the formula $E_b = \frac{\hbar^2}{2m_{red}(a-\bar{a})^2}$, where \bar{a} is the mean scattering length, or Feshbach molecule binding energy at resonance. The scattering length a relation to magnetic field B is approximated by Eqn. 2.1. We utilize Feshbach molecule as initial state to create excited state molecules in Chapter 3, and to create ground state molecules in Chapter 4. However, Feshbach molecules suffer rapid losses due to inelastic collisions with residue atoms, which presents an obstacle of creating ground state molecules using Feshbach molecules as the initial state. In the following section, we will discuss the

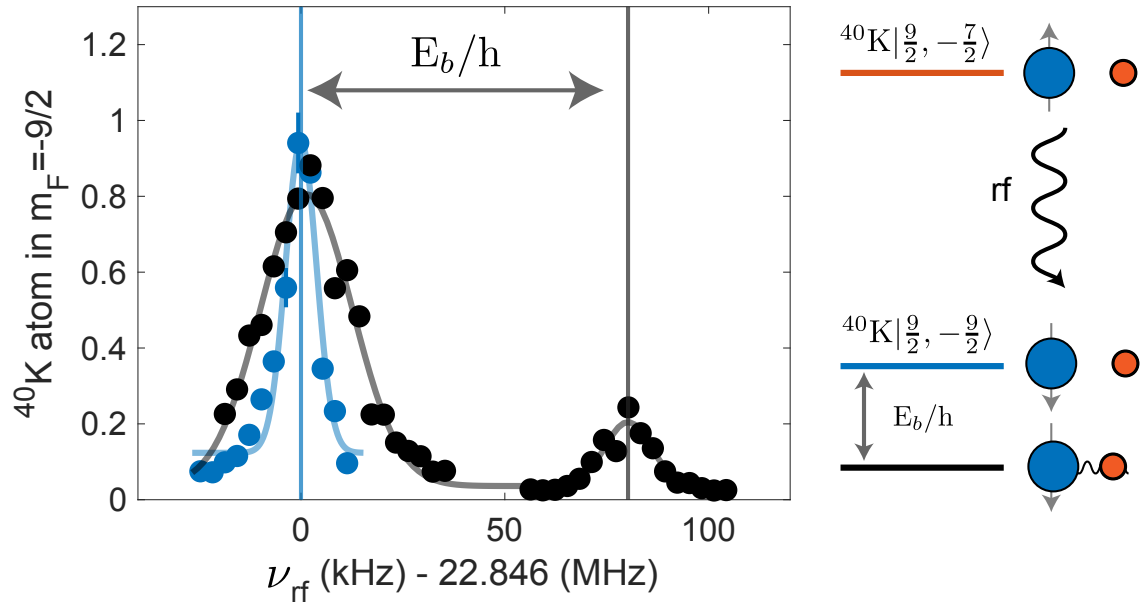


Figure 2-2: Radio-frequency association of $^{23}\text{Na}^{40}\text{K}$ Feshbach molecule. At a magnetic field of 85.7 G, we apply a square-shaped rf pulse to transfer the initial $^{23}\text{Na} |1, 1\rangle$ and $^{40}\text{K} |9/2, -7/2\rangle$ mixture to the final state, either the atomic state of $^{23}\text{Na} |1, 1\rangle + ^{40}\text{K} |9/2, -9/2\rangle$, or the weakly-bound Feshbach molecules with a binding energy E_b that is energetically below the atomic state. The blue dots represent the rf spectrum obtained for magnetic field calibration, where only ^{40}K atoms are present. In the absence of ^{23}Na , atomic state of $^{40}\text{K} |9/2, -9/2\rangle$ is the only final state, which provides an accurate magnetic field calibration. The broadening of the atomic peak in the Feshbach molecule association spectrum, shown in black, can be attributed to a combination of broadening induced by high rf power and mixture inter-species interactions [83, 87].

three-body physics responsible for the inelastic collisions.

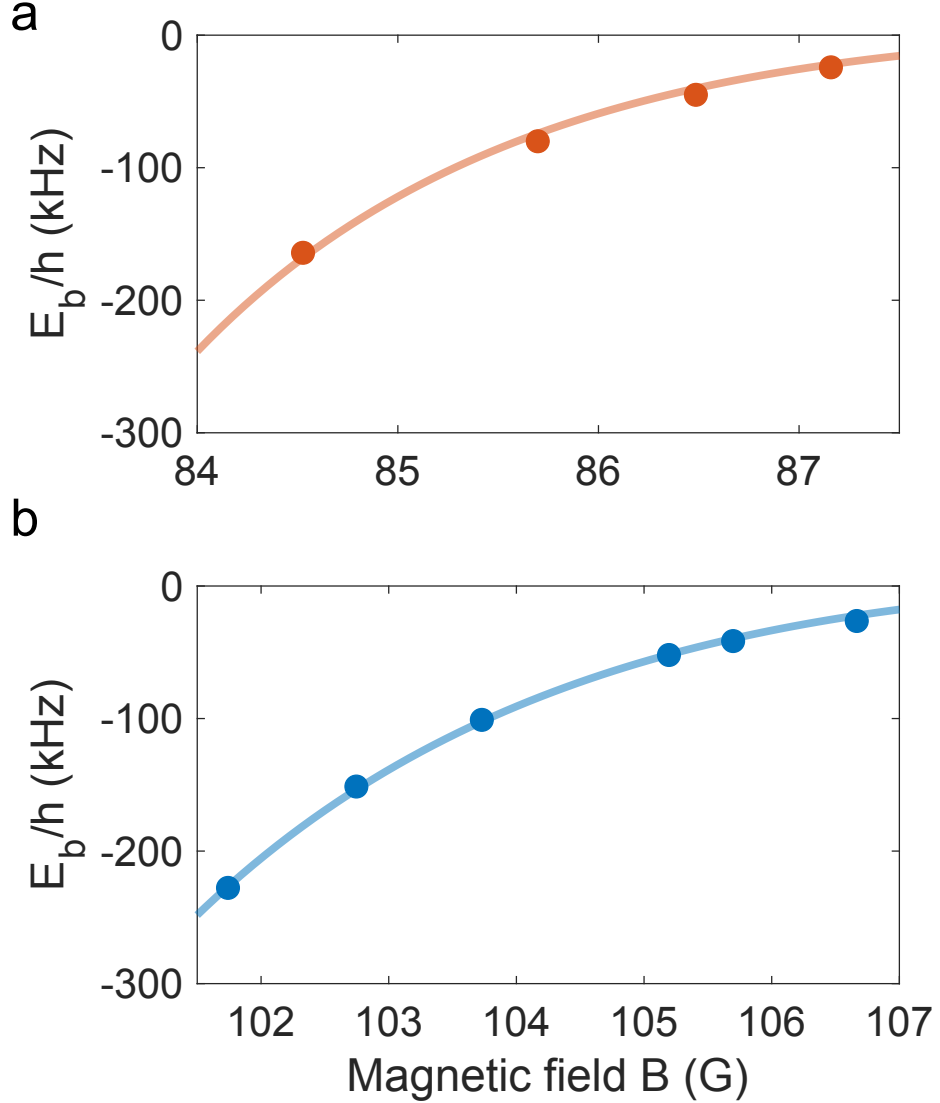


Figure 2-3: $^{23}\text{Na}^{40}\text{K}$ Feshbach molecule binding energy dependence on magnetic field. a. Molecule binding energy of $^{23}\text{Na}|1, 1\rangle ^{40}\text{K}|9/2, -9/2\rangle$ near the $B_0 = 89.8$ G Feshbach resonance, and b. molecule binding energy of $^{23}\text{Na}|1, 1\rangle ^{40}\text{K}|9/2, -7/2\rangle$ near the $B_0 = 110.3$ G Feshbach resonance. The initial atom sample is prepared with ^{40}K in $m_F = -7/2$ (-9/2) before the rf molecule association pulse for a (b). Feshbach molecule binding energies E_b are determined by the energy difference between the atomic and molecular peak in the rf association spectroscopy. Solid blue and orange lines are fit results based on $E_b = \frac{\hbar^2}{2m_{red}(a-\bar{a})^2}$, which captures the binding energy approximately quadratic dependence to the magnetic field.

2.2 Bose polaron Chevy ansatz

It has been a long-standing topic in many-body physics to understand the properties of impurities immersed inside a quantum degenerate bath. For instance, an electron moving through lattice of ionic cores induces the phonon excitations from the underlying lattice. This self-induced electron-phonon interaction significantly alters the bare electron properties such as particle self-energy and effective mass. The lattice-dressed electron, which was first theorized by Landau [46] and Pekar [61] who named it the polaron, is a textbook example of quasiparticle formulation. Experimentally testing the bare particle that is dressed by the medium via mutual interaction reveal the emergent many-body physics. Ultracold quantum gas systems provide certain advantages. Unlike solid-state system where the electron-phonon coupling strength is fixed in a given material, ultracold quantum gases with interaction precisely controlled by Feshbach resonances allows continuous tuning of the same system from weakly to strongly, and repulsively to attractively interacting polarons. The dressing of impurities into quasiparticles in a ultracold atom experiments was first observed in the case of the Fermi polaron, which is an atomic impurity embedded in a Fermi sea [67, 53, 45, 44, 17, 66, 86]. In this thesis work, we emphasis on experimental study of the Bose polaron, which is a impurity dressed by a Bose-Einstein condensate (BEC). Experimental evidences of Bose polaron effects were observed in many AMO experiments [58, 84, 40, 24, 65, 16]. In particular at Fermi 1, we used spatially resolved radio-frequency spectroscopy to study the fate of strongly interacting Bose polaron near quantum criticality point by immersing fermionic ${}^{40}\text{K}$ impurities inside a ${}^{23}\text{Na}$ BEC [87]. Along with experimental investigations of Bose polarons, there has been a plethora of theoretical works on this topic [77, 64, 21, 37, 80, 70, 90]. In this section, we introduce a theoretical framework that uses a variational ansatz to describe essential properties of Bose polaron quasiparticles. It was Chevy who first proposed to use this type of trial wavefunction ansatz which successfully captured the essential characteristics of the Fermi polaron [19]. Authors in [49] further extended Chevy ansatz to Bose polarons. The solution presents a stable attractive polaron branch, which

smoothly evolves from negative to positive scattering length and eventually merges with the Feshbach molecules. Furthermore the solution provides a repulsive polaron branch with finite lifetime that only exists at positive scattering length. We use the following Hamiltonian to describe the underlying fermionic impurity interaction with the condensate:

$$H = \sum_k \epsilon_b(k) b_k^\dagger b_k + \sum_k \epsilon_f(k) f_k^\dagger f_k + \frac{g_{bf}}{V} \sum_{k,k',q} b_{k'}^\dagger f_{q-k'}^\dagger f_{q-k} b_k \quad (2.2)$$

The Hamiltonian consists of summation of boson (fermion) kinetic energy term $\epsilon_b(k)$ ($\epsilon_f(k)$), and the interaction term. Fermi initially proposed using a delta function to model short-range interactions in position space, approximating that inter-particle potential details are not relevant since physics is solely determined by the outcome particle phase shifts [32]. As a result of the impurity coupling to the condensate via this point-like contact potential in position space, the interaction is a constant $g_{bf} = \frac{2\pi a_{bf}}{m_{red}}$ in momentum space, which is a function of the inter-species scattering length a_{bf} . This Fermi's pseudopotential approach simplifies calculations at weakly interacting regime, but it typically causes divergences at interaction unitarity when $a_{bf} \rightarrow \infty$. This divergences can be circumvented by renormalizing the coupling parameter g_{bf} to a more physical quantity such as inter-particle spacing near the interaction unitarity [91],

$$\frac{1}{g_{bf}} = \frac{m_{red}}{2\pi a_{bf}} - \frac{1}{V} \sum_k \frac{2m_{red}}{k^2} \quad (2.3)$$

The coupling parameter g_{bf} has two competing terms: at large scattering length where a_{bf} diverges, g_{bf} is determined by the second kinetic energy term that relates to inter-particle spacing. At small scattering length limit, g_{bf} is still determined by a_{bf} . Next we insert the Chevy ansatz, which is a trial wavefunction that is proposed for the Bose polaron in [49],

$$|\Psi^{(q)}\rangle = (\psi_0^q f_q^\dagger + \sum_{k \neq 0} \psi_k^{(q)} f_{q-k}^\dagger b_k^\dagger) |\text{BEC}\rangle \quad (2.4)$$

When the fermion interacts with the surrounding BEC, it creates excitations that the $k = 0$ bosons have certain probability of being scattered into the $k \neq 0$ states. In return, the fermion itself also gets dressed by these bosonic excitations and becomes a Bose polaron quasiparticle. Therefore this trial wavefunction is a coherent superposition of two parts: $\psi_0^q f_q^\dagger |BEC\rangle$ quasiparticle residue that is delocalized in position space, and $\sum_{k \neq 0} \psi_k^{(q)} f_{q-k}^\dagger b_k^\dagger |BEC\rangle$ a localized part that has the same distribution as a Feshbach molecule. We employ the variational method to calculate the ground state energy of this trial wavefunction. The variational approach utilized here is very similar to the one used by Bardeen, Cooper, and Schrieffer (BCS) to calculate the emergence of Cooper pairs in superconductors [4]. The ground state of the system as the variational minimum is given by $\frac{\partial \langle \Psi | H - E | \Psi \rangle}{\partial \psi^*} = 0$, where E is the variational energy that also acts as a Lagrangian multiplier to ensure wavefunction is normalized $\langle \Psi | \Psi \rangle = 1$. With derivation details spared in the Appendix B, we arrive to the self-consistent equation:

$$E(q) = \epsilon_f(q) + \frac{n_B}{\frac{1}{g_{bf}} - \frac{1}{V} \sum_k \frac{1}{E(q) - \epsilon_f(q-k) - \epsilon_b(k)}} \quad (2.5)$$

This self-consistent polaron energy equation can be solved numerically for each quasiparticle mode q , along with the polaron effective mass m^* .

$$E(q) = E(q=0) + \frac{q^2}{2m^*} + \mathcal{O}(q^3) \quad (2.6)$$

Shown in Fig 2-4, we highlight the numerically solved polaron self-energy $E(q=0)$, which has an attractive and a repulsive branch. The interaction strength in x-axis is plotted in $(k_n a)^{-1}$, where $k_n = (6\pi^2 n_B)^{1/3}$ is the inter-boson distance, and a is the inter-species scattering length. The energy in y-axis is normalized by the BEC degeneracy energy $E_n = \frac{\hbar^2 k_n^2}{4m_{red}}$. The repulsive polaron solution shown as red in Fig. 2-4 is a metastable branch. The repulsive polaron possesses a complex energy due to the imaginary part of its self-energy (indicated as the red dashed line), resulting in a finite lifetime. The instability of the repulsive polaron is attributed to the number and

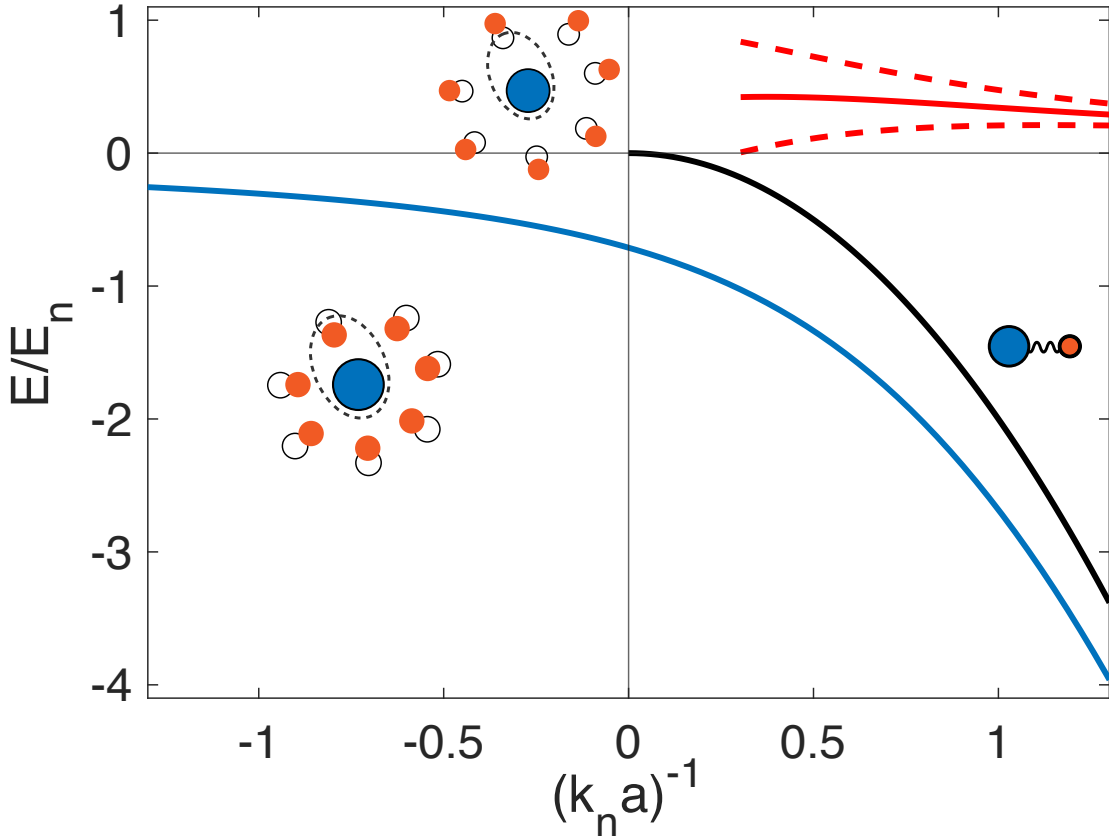


Figure 2-4: Energy spectrum of Bose polaron from variational ansatz. We numerically solve the self-consistent equation 2.6, which gives us two branches. The red curve represents the repulsive polaron branch, which has a complex energy. The repulsive polaron has a positive real energy shown as red solid line, as the red dashed line $Re(E) \pm Im(E)/2$ shows the associated imaginary energy. The imaginary energy results finite lifetime of the repulsive polaron, resulting its instability. The blue curve demonstrates the attractive polaron branch, which has negative and pure real energy, representing the system ground state. The attractive polaron evolves continuously from weak interaction $(k_n a)^{-1} \ll -1$, to strong interaction $(k_n a)^{-1} \rightarrow 0$, and at $(k_n a)^{-1} \gg 1$ it eventually merges with the Feshbach molecule branch shown as the black curve.

phase fluctuations of the surrounding BEC [38]. As the interaction strength increases, the repulsive polaron experiences increasingly significant perturbations from the BEC fluctuations. This leads to the termination of the repulsive polaron in the strongly interacting regime, where the imaginary part of the self-energy becomes larger than the real part $Im(E) > Re(E)$. The metastable repulsive polaron eventually decays to the system ground state, represented by the attractive polaron branch depicted in blue. The attractive polaron branch smoothly evolves from negative to positive scattering length. At weakly interacting regime $(k_n a)^{-1} \ll -1$, also known as Fröhlich polaron, we recover the mean-field energy $E_{MF} = \frac{2\pi a n_B}{m_{red}}$. The attractive polaron remains well-behaved at the interaction unitarity $(k_n a)^{-1} = 0$, as a result of the coupling constant renormalization in Eqn. 2.3. The attractive polaron eventually merges with the Feshbach molecule branch (shown in black line) at $(k_n a)^{-1} \gg 1$. The molecular character of the polaron comes from the localized part of the wavefunction $\sum_{k \neq 0} \psi_k^{(q)} f_{q-k}^\dagger b_k^\dagger |BEC\rangle$, which in position space has form of $\frac{1}{r} e^{-\kappa r}$, identical to a Feshbach molecule. Therefore the attractive polaron can be intuitively pictured as a dressed molecule with a molecular size r determined by the polaron energy E ,

$$r = \sqrt{\frac{\hbar^2}{2m_{red}(-E)}} \quad (2.7)$$

The change of polaron energy in relation with the scattering length also reveals the contact C , which is universal many-body quantity,

$$C = \frac{8\pi m_{red}}{\hbar^2} \frac{\partial(-E)}{\partial(a^{-1})}. \quad (2.8)$$

It is this molecular nature of Bose polaron that enables us to create ground state molecules, which will be experimentally realized in Chapter 3 and 5. The attractive polaron is the system ground state when there is only elastic collision.

In the next section, we discuss inelastic collision which leads to finite lifetime of the Bose-Fermi mixture.

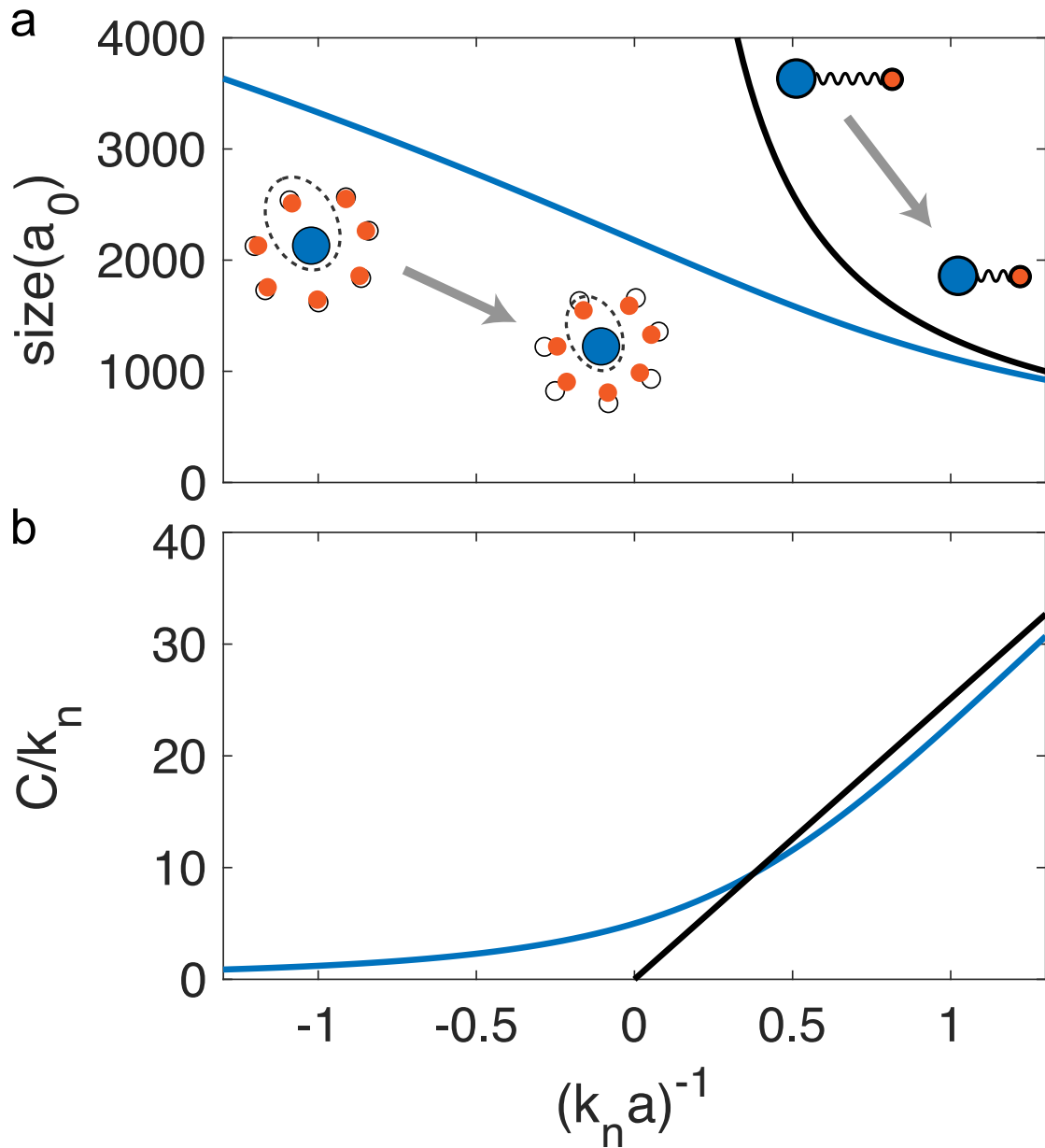


Figure 2-5: Contact and size of Bose polaron from variational ansatz. a. Effective size of the attractive polaron in comparison with the Feshbach molecule. As the attractively polaron continuously evolves from negative to positive scattering length, the effective molecular size of the polaron shrinks as the polaron energy decreases. b. Contact of the attractive polaron in comparison with the Feshbach molecule.

2.3 Three-body physics

The Bose-Fermi mixture of ^{23}Na - ^{40}K provides a rich testing ground for exploring three-body problems that is beyond two-body physics. In this section, we will discuss the population loss in the Bose-Fermi mixture due to inelastic collisions from three-body recombinations, which involve two bosons and a fermion. The rate of three-body recombination has a strong dependence on the inter-species scattering length a to its 4th power, making it a significant factor to consider in experiments. In the second part of this section, we will discuss the effects of three-body resonances, also known as Efimov resonances, which modify the inelastic collisions on top of this broad three-body recombination rate $\propto a^4$.

2.3.1 Three-body recombination

Two-body collisions are generally preserved to be elastic because of conservation of momentum and energy. However, inelastic collision happens when a third particle participates the collision event. As shown in Fig. 2-6, two bosons (orange) and a fermion (blue) form a collision complex, with a radius set by the inter-species scattering length a . The outcome of the complex is a recombination, where the fermion and a boson form a molecule, releasing kinetic energy that is carried away by the molecule and the second boson. The released energy typically causes the molecule and the boson to leave the trap, leading to a loss of population. Based on [31], we provide a qualitative estimation on the rate of three-body recombination L_3 at zero-temperature limit, which successfully gives $L_3 \propto a^4$ relation. The three-body recombination rate sets event probability p_3 per unit volume and per unit time as $p_3 = L_3 n_F n_B^2$. Within the event radius set by scattering length a , the boson-fermi scattering rate per volume can be estimated as $n_F n_B \sigma v$, where $\sigma = 8\pi a^2$ is the inter-species two-body scattering cross-section area. At the zero temperature limit, the size of collision complex also sets the collision velocity $v \propto 1/a$. The presence of a second boson in the collision complex, with a probability $\approx n_B a^3$, facilitates the formation of molecule and carries away the released molecule binding energy with

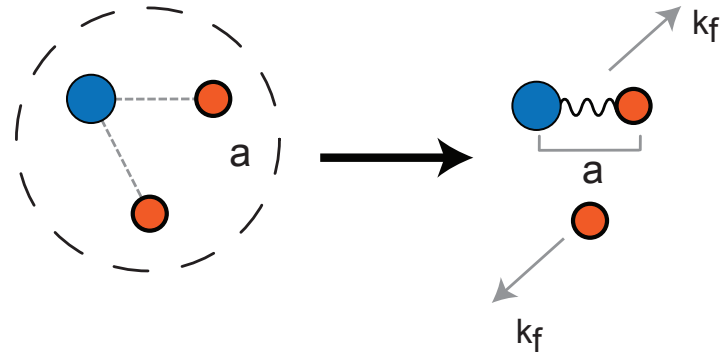


Figure 2-6: Illustration of a three-body recombination event among a fermion and two bosons. Three orange circles represent three identical bosons within radius a , where they go through a three-body recombination process. A weakly-bound molecule with size a and a third particle are the end product of the recombination. The molecule releases its binding energy $E_b \approx \hbar/(ma^2)$ that is carried away by both the molecule and the third atom with equal momentum k_f .

a unity probability. As a result, $p_3 \approx (n_F n_B \sigma v)(n_B a^3)$, and we arrive the three-body recombination rate $L_3 \propto a^4$. The full quantum calculation on the three-body recombination was first estimated for 3 identical bosons [31], and later extended to Bose-Fermi mixture at zero temperature limit in [39], and at finite temperature in [62].

Experimentally, the three-body recombination rate can be measured via the mixture population lifetime that is function of boson and fermion density together with L_3 :

$$\frac{dn_F}{dt} = \frac{1}{2} \frac{dn_B}{dt} = -L_3 n_F n_B^2 \quad (2.9)$$

The boson density typically decays much faster due to three-body recombination involves 2 bosons, while at boson majority limit, fermions follow an exponential decay curve. The lifetime of the mixture is therefore a good indicator of the three-body recombination rate, which can be compared to theoretical predictions based on the zero-temperature model. Fig. 2-7 demonstrates the $^{23}\text{Na}^{40}\text{K}$ mixture three-body recombination rate measurement across a Feshbach resonance, which was observed by [18]. We observe a similar three-body recombination rate at Fermi 1, which we will discuss in Chapter 3. The zero-temperature theory predicts a L_3 enhancement

around $-100 a_0$ due to onset of the first three-body bound state, which is related to Efimov physics. We will discuss Efimov resonances and related observations at Fermi 1 in the next section.

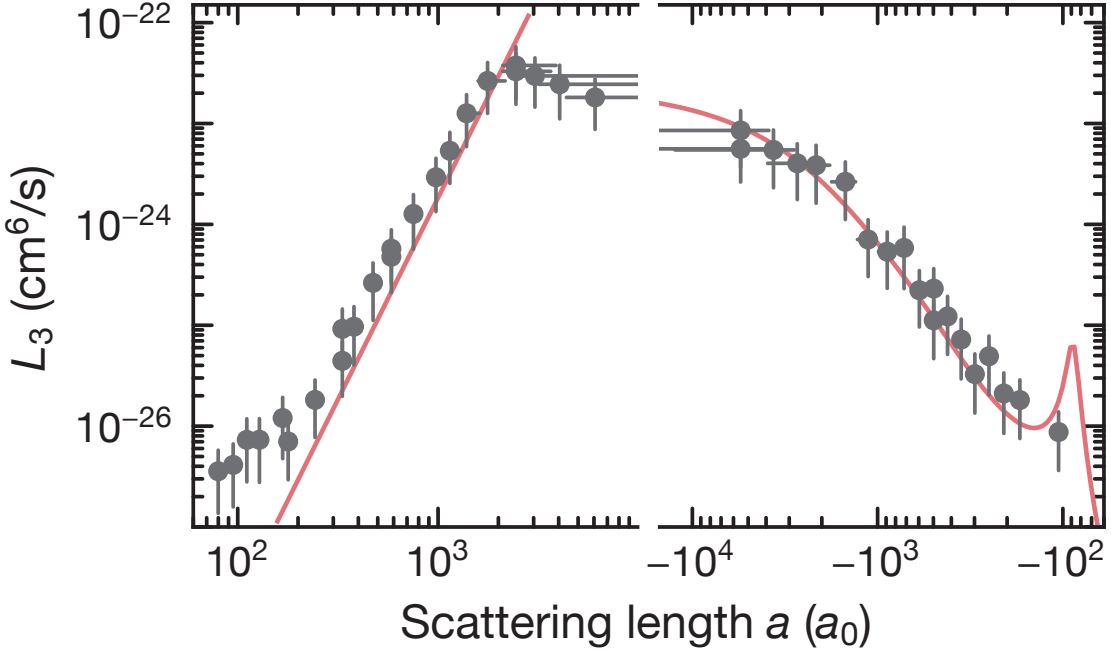


Figure 2-7: Measurement of $^{23}\text{Na}^{40}\text{K}$ three-body recombination rate from [18]. The three-body recombination rate L_3 is described by a zero-temperature theory based on a numerically solved effective field model [39]. The red solid line shows the fitted zero-temperature theory, which $L_3 = \xi \frac{\hbar^2}{m_{red}} a^4$. The effective field method reproduces L_3 with a broad trend proportional to a^4 , with a coefficient ξ due to Efimov physics. ξ depends on the mixture mass ratio, van der Waals range, and width of the Efimov resonance. See Eqn. (13) in [39] for the full expression of ξ .

2.3.2 Efimov resonances

Efimov universality, originally proposed by Efimov [30], describes three-body dynamics using few physical quantities. For instance, three identical bosons are theorized to have infinite series of three-body bound states – Efimov states. The Efimov state energy spectrum display a discrete scaling invariance as infinitely many three-body bound states exist in series governed by Efimov scaling factor $\lambda = e^\pi \approx 23$. As shown in Fig. 2-8, the first Efimov state starts at the negative scattering length $a_-^{(1)}$ that is typically close to van der Waals range r_{vdW} . The first Efimov state energy $E_*^{(1)}$ at interaction unitarity $a^{-1} \rightarrow 0$ is determined by its wavevector $\kappa_*^{(1)}$ that is close to $1/a_-^{(1)}$, therefore $E_*^{(1)} \approx \frac{\hbar^2}{2m_{red}(a_-^{(1)})^2}$, where m_{red} is two body reduced mass. In summary, Efimov states follows the discrete invariance by the Efimov scaling factor λ as:

- $a_-^{(n+1)} = \lambda a_-^{(n)}$
- $a_*^{(n+1)} = \lambda a_*^{(n)}$
- $E_*^{(n+1)} = \lambda^2 E_*^{(n)}$

At the positive scattering length, Efimov states are energetically lower than the two-body bound state, until Efimov states merge with the two-body bound states at scattering length a_* . Efimov universality assumes two-body resonance from a zero-range interaction potential, where the three-body problem can be reduced to single body in the hyperspherical coordinate with potential $V \approx 1/R^2$. However, realistic two-body interactions have finite length scale that is characterized as van der Waals range. For example, the first trimer bound state starts from small negative scattering length, which typically are atomic species dependent. Because small scattering length probes short-range potential details, which depends on atomic species, hyperfine states, and temperature. The first Efimov state is experimentally observed around van der Waal's range $a_-^{(1)} \approx -r_{vdW}$. This experimental phenomenon are called “van der Waals’ universality”. At large scattering length, experimental resolution is limited by rapid three-body recombination rate. Due to these two limitations, exper-

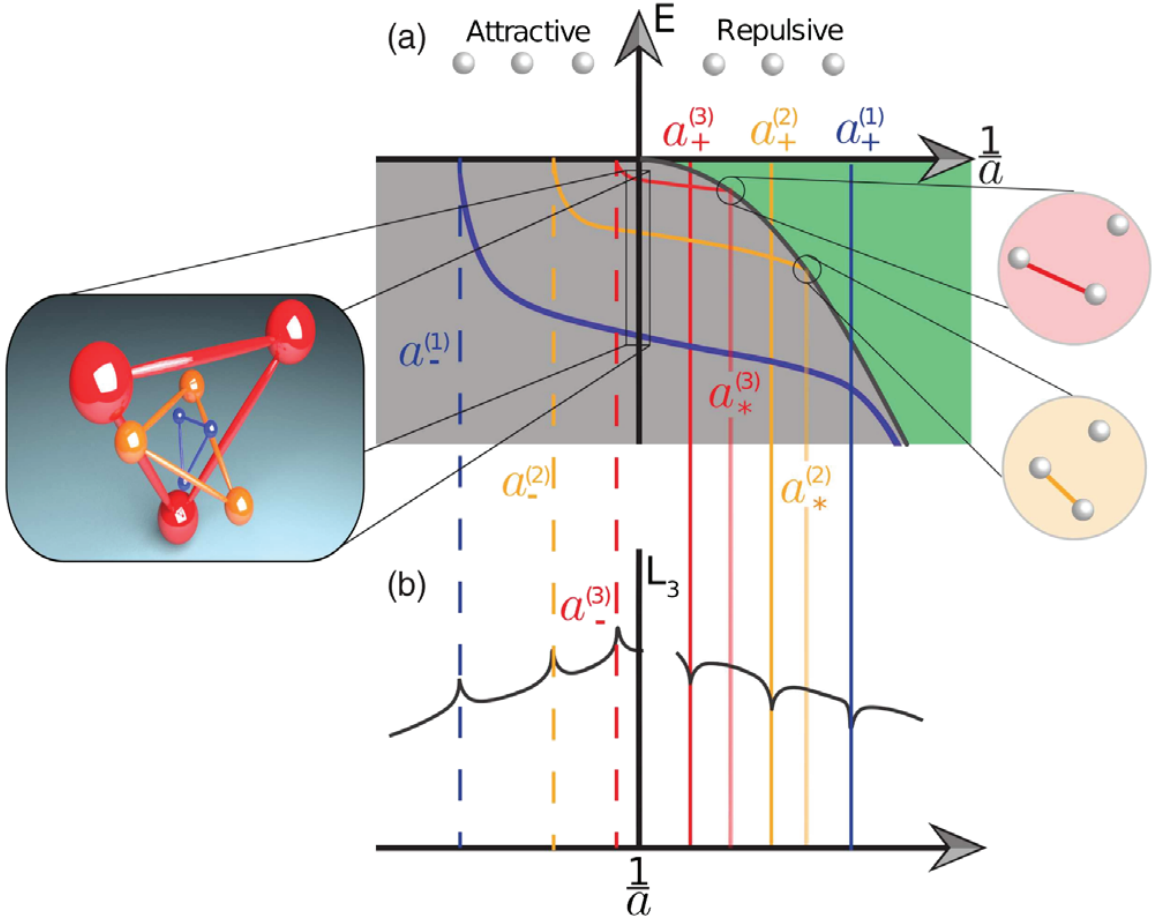


Figure 2-8: Illustration of Efimov energy spectrum and Efimov resonances from [36].
 a. Illustration of Efimov state energy spectrum. Black line illustrates the two-body bound state $E_{\text{dimer}} = \frac{\hbar^2}{2m_{\text{red}}a^2}$ that exists at positive scattering length. The first Efimov state, shown in blue, starts at negative scattering length $a_-^{(1)}$ that is close to the van der Waals range r_{vdW} . The same Efimov state has energy $E_*^{(1)}$ at unitarity $1/a \rightarrow 0$, and merges with the two-body bound state from below at scattering length $a_*^{(1)}$. The discrete invariance is manifested in each consecutive Efimov state and illustrated in the cartoon. b. Illustration of three-body recombination rate influenced by Efimov states. The onset of Efimov states at negative scattering enhances the three-body loss, as trimer states provide additional loss channel for the mixture. At positive scattering length destructive interference between two decay pathways at scattering length $a_+^{(1,2,3\dots)}$ causes local L_3 minimum.

imentalists have a limited range of scattering length to explore the Efimov physics [85]. Experimental study of Efimov universality is an ongoing research field, and the Efimov universal structures are usually observed via modulations on top of the three-body recombination rate L_3 . Weakly-bound Feshbach molecules are absent at negative scattering length, therefore trimers are the closest decay channel for the mixture. Therefore at the onsets of Efimov bound states $a = a_-^{1,2,3\dots}$, where trimers are closest to the mixture in the free-particle continuum, three-body recombination rate is enhanced. At positive scattering, atoms have two decay channels, dimers and trimers, which can interfere. As results, three-body recombination rates have local minimum from two decay pathways destructive interference, or local maximum from constructive interference.

Fig. 2-9 demonstrates our experimental observation of a three-body recombination minimum at 80.8 G due to the destructive interference from a nearby Efimov bound state. We prepare the mixture at their hyperfine ground states, ${}^{23}\text{Na}|1,1\rangle$ and ${}^{40}\text{K}|9/2, -9/2\rangle$, and temperature of 100 nK, where bosons are above condensate temperature. As shown in Fig. 2-9a, we precisely determine the two-body scattering length zero at 80.3 G, by performing the ${}^{23}\text{Na}{}^{40}\text{K}$ cross thermalization technique discussed in Section 2.1.1. In the cross thermalization between ${}^{23}\text{Na}$ and ${}^{40}\text{K}$ is only a function of two-body elastic scattering, therefore independent of three-body recombination. To determine the three-body recombination minimum, we provide the mixture with a 20 s of three-body recombination time in the ODT. The remaining mixture population was then measured via absorption image. The minimum three-body recombination leads to maximum mixture population survival in the end. As shown in Fig. 2-9b, a minimum recombination rate is observed at 80.8 G, signaling population decay interference due to the underlying Efimov state.

Efimov originally predicted $\lambda = e^\pi \approx 23$ based on three identical bosons with zero-range interaction potential. However, the Efimov scaling factor for Bose-Fermi mixtures has more subtleties and requires more careful treatment. The Efimov scaling factor λ is mixture-dependent by the following two factors,

- Fermion and boson mass ratio: m_F/m_B

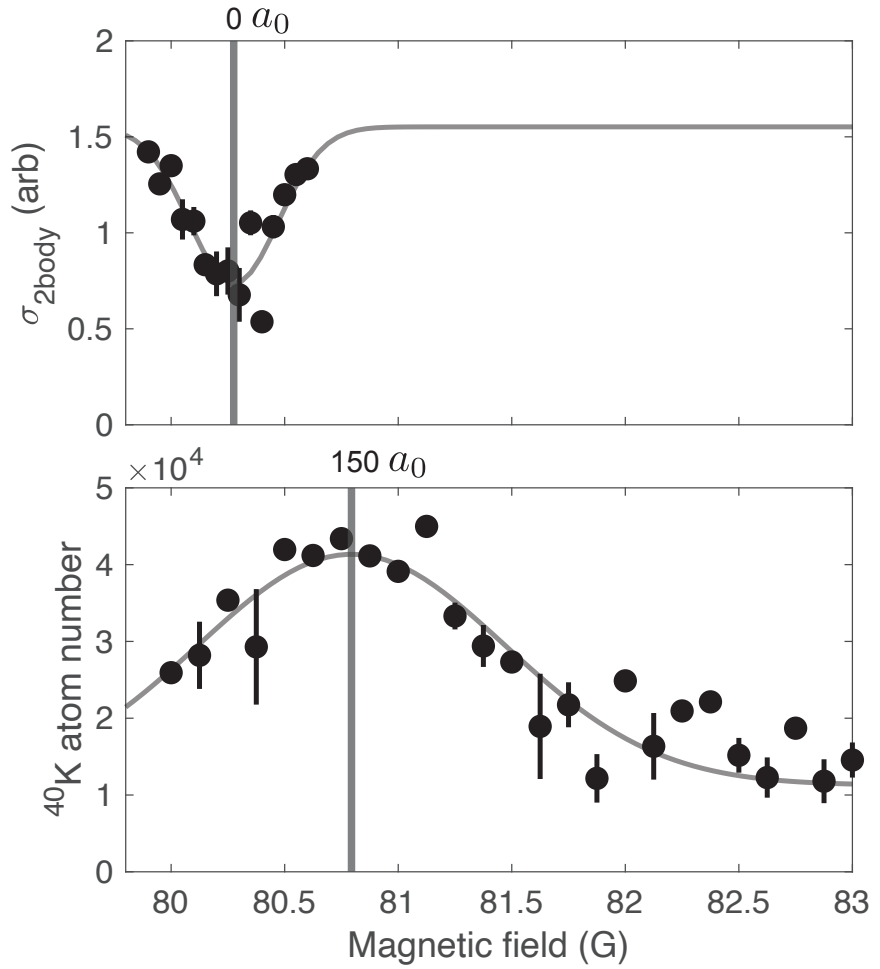


Figure 2-9: Observation of Efimov resonance via recombination rate minimum. a. Measurement of two-body scattering length zero via two-body cross thermalization. We determine zero scattering length at magnetic field of 80.3 G, where ^{40}K has minimum cross thermalization rate with ^{23}Na atoms. The two-body thermalization rate, measured via atomic cloud shape, is independent of population loss due to inelastic collision. b. Measurement of minimum three-body recombination rate. After a 20 s three-body recombination time for the $^{23}\text{Na}^{40}\text{K}$ mixture, we measure the remaining atoms, and observe that at 80.8 G, the minimum three-body recombination rate leads to the maximum surviving ^{40}K population.

- Inter-species scattering length a_{bf} and boson-boson scattering length a_{bb}

In the case of $^{23}\text{Na}^{40}\text{K}$ mixture, inter-species interaction is dominant over weak boson-boson scattering ($a_{bb} \approx 55 a_0$). Therefore we consider $^{23}\text{Na}^{40}\text{K}$ as ‘case i’ in [62], where we can neglect boson-boson interaction which simplifies the calculation. The mass of ^{40}K and ^{23}Na of $m_F/m_B = 1.7$ leads to a ‘Efimov unfavored’ scenario [36]. Fig. 2-10 shows the Efimov scaling factor versus mixture mass ratio m_F/m_B . Relation of λ to mass ratio m_F/m_B is very much unforgiving in the heavy fermion, plus weak inter-boson interaction regime. For our $^{23}\text{Na}^{40}\text{K}$ mixture, we calculate $s_0 = 0.285$, or in terms of scaling factor $\lambda = e^{\pi/s_0} = 6 \times 10^4$. Therefore, we assign the observed three-body recombination minimum at scattering length $a = 150 a_0$ to the destructive interference between the decay pathways of the dimer and the first Efimov bound state, which is the only experimentally accessible Efimov bound state for $^{23}\text{Na}^{40}\text{K}$.

In conclusion, the rich Feshbach resonances of $^{23}\text{Na}^{40}\text{K}$ is a gift that enabled us to realize strongly interacting many-body systems. The strong two-body elastic scattering gain in a system can also lead to an increase in three-body recombination events, which can impose experimental restrictions. In Chapters 3 and 5 we will discuss the creation of dipolar molecules in a Goldilocks regime, where the elastic interactions are strong enough to form a strongly interacting Bose polaron system, while still allowing for a sufficient mixture lifetime. It is also an interesting direction in the future to observe the Efimov bound state influence on the Bose polaron binding energy.

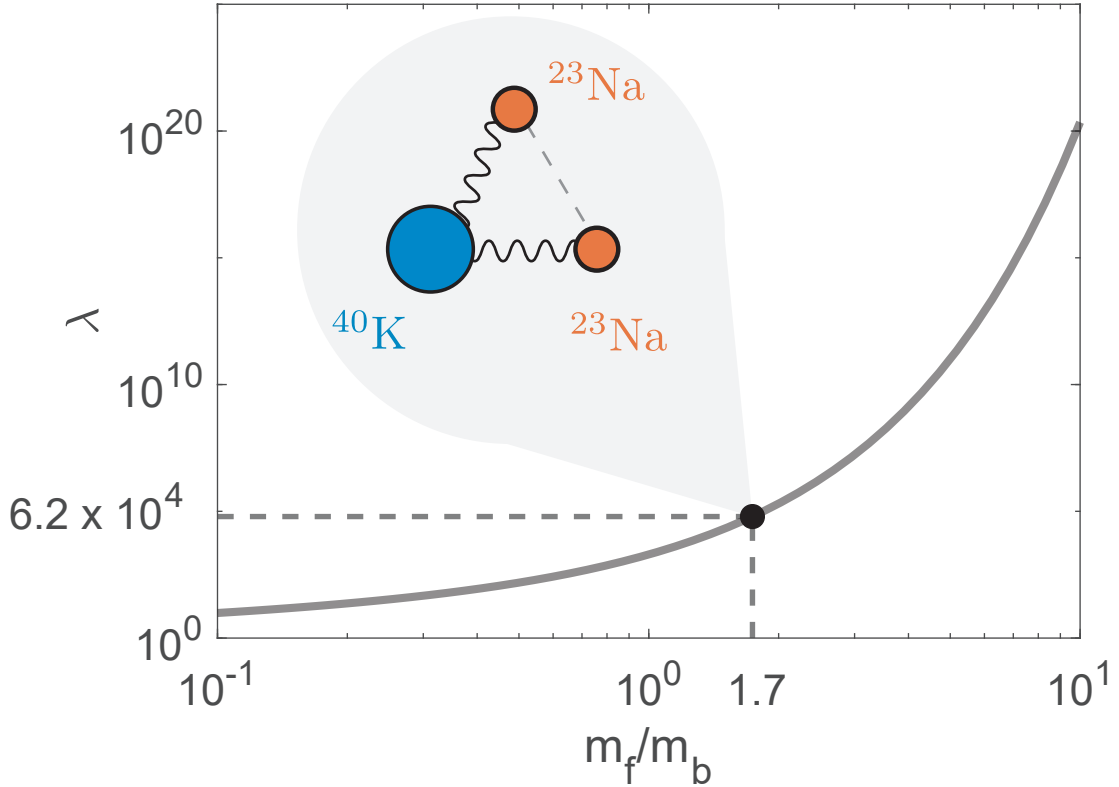


Figure 2-10: Efimov scaling factor vs mass balance. The solid curve represents the Efimov scaling factor, as a function of the mixture mass ratio $\frac{m_F}{m_B}$, which is obtained by numerically solve Eqn. (8) in [62]. The Efimov scaling factor, displayed in logarithmic scale on the y-axis, exhibits a steep increase as a function of the mixture mass ratio $\frac{m_F}{m_B}$. This poses a significant challenge for experimental realization of multiple Efimov states in the $^{23}\text{Na}^{40}\text{K}$ mixture. The inset cartoon illustrates the inter-species interaction a_{bf} between $^{23}\text{Na}^{40}\text{K}$ dominates over the boson-boson interaction. Inter-boson scattering length $a_{bb} \approx 55 a_0$ remains constantly weak at the magnetic field range 60 to 140 G, where a_{bf} dominates.

Chapter 3

Photoassociation

Photoassociation is a crucial step in the process of creating ground state molecules from atomic samples, and it has a rich history in AMO physics [42]. In this chapter we first introduce the Franck-Condon principle, which is an intuitive model for understanding photoassociation spectra. Second, we will discuss the photoassociation of Feshbach molecules, which are a traditional initial state for creating ground state molecules in bi-alkali experiments. Third, we will present our study on photoassociating Bose-Fermi mixture that has strongly attractive interactions, which can be described in terms of Bose polarons quasi-particles. Unlike Feshbach molecules, polarons are not weakly-bound states but are instead quasi-particles that are close to the free-particle continuum. Therefore, we observe a strong influence of the continuum on the photoassociation spectrum, which leads to nonlinear effects.

3.1 Analogy to three-body recombination

We can draw a simple analogy between photoassociation (photoassociation) and three-body recombination discussed in Section 2.3.1. Instead of a third atom participating in the recombination process, an incident photon acts as the third collisional partner that photoexcites an atom pair into the electronically excited molecule. The $^{23}\text{Na}^{40}\text{K}$ electronically excited state has spontaneously decay rate $\gamma_e/2\pi = 10 \text{ MHz}$, or $\approx 10 \text{ ns}$ lifetime before it decays to lower molecular states. The absorption imaging beams,

which are resonant with ^{23}Na and ^{40}K atoms, are not resonant with molecules, making them invisible to the imaging system. This results in a loss of signal for photoassociated molecules during the imaging process. High-precision control of photoassociation laser enables new avenues to probe the mixture property in addition to rf spectroscopy.

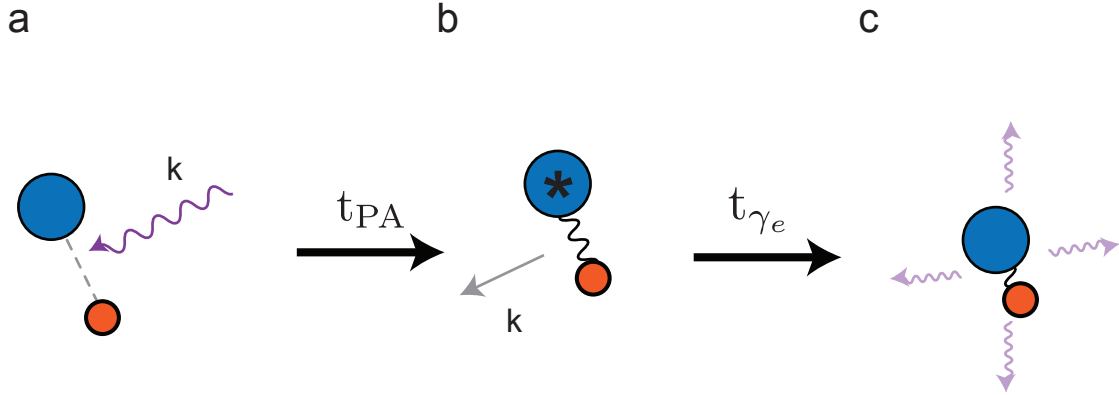


Figure 3-1: The three-body recombination analogy to the photoassociation process. a. Three initial collisional partners consists of ^{23}Na and ^{40}K atom pair, and a photoassociation photon with momentum k . b. In the photoassociation time window of t_{PA} , the atom pair is promoted to an electronically excited molecule by absorbing the photon through stimulated absorption. c. The electronically excited molecule only has a short lifetime of $t_{\gamma_e} \approx 10$ ns before it spontaneously emits a photon and decays to a tight-bound molecule. The imaging beams, which are resonant with atoms, do not interact with molecules, resulting in the photoassociation signal appearing as a negative signal in the atomic counts.

3.2 Franck-Condon description of photoassociation

James Franck proposed an intuitive approximation of the photoassociation process, where the electron transits rapidly from one molecular potential to another, compared to the nuclear vibrational motion. As a result, the nuclear vibrational motion remains in the same position and velocity after the electronic transition [34]. This concept is known as the Franck-Condon principle, named after Franck and Condon, who later formulated photoabsorption/emission quantitatively using wave mechanics. Franck-Condon principle successfully predicted early molecular absorption and

emission spectrum between different vibrational states, and still instrumental in understanding modern photoassociation transitions. Advances in AMO experiments, such as sub-kHz linewidth laser and Bose-Fermi mixture at ultracold temperature $T < 100$ nK ($k_B T/h < 2$ kHz), has brought photoassociation spectroscopy to the single quantum level. As a result, we are now able to experimentally resolve features within each vibrational manifold of the molecules, including their rotational, fine, and hyperfine structures. A photoassociation laser can promote an atom pair into a bound molecular state by stimulated absorption. Franck-Condon principle approximates photoassociative rate in the following way. Based on Born-Oppenheimer approximation, a molecule wavefunction $|\psi_m\rangle$ can be separated into the heavy nuclear part $|\psi_n\rangle$, and the light electronic portion $|\psi_e\rangle$: $|\psi_m\rangle = |\psi_n\rangle |\psi_e\rangle$. The electric dipole transition that promotes the initial atom pair state $|\psi_a^i\rangle$ to the electronically excited state $|\psi_m^f\rangle$ is driven by the electric field E from the photoassociation laser, which provides a coupling matrix element

$$\langle \psi_m^f | d \cdot E | \psi_a^i \rangle = \langle \psi_e^f | d_e \cdot E | \psi_e^i \rangle \langle \psi_n^f | \psi_n^i \rangle \quad (3.1)$$

We use the Franck-Condon factor $f_c = \langle \psi_n^f | \psi_n^i \rangle$ to describe the nuclear wavefunction overlap between the initial and final states. The transition driving electric field E is proportional to the square root of laser intensity I : $E = \sqrt{\frac{2\pi I}{c}}$. The electronic transition dipole moment $d = \langle \psi_e^f | d_e | \psi_e^i \rangle$ depends on the electronic potential and can be theoretically estimated [9]. Therefore the photoassociative formation rate Γ can be approximated by the Fermi's golden rule together with the coupling matrix:

$$\Gamma_{i \rightarrow f} = \frac{2\pi}{\gamma_e} \frac{2\pi I}{c} d^2 f_c^2 \quad (3.2)$$

The density of final state is given by the excited state spontaneous decay rate γ_e . In the next section, we perform photoassociation spectroscopy on weakly-bound Feshbach molecules.

3.3 Photoassociating Feshbach molecules

Employing the radio frequency (rf) association method described in Chapter 2.1.2, we create 60×10^3 $^{23}\text{Na}^{40}\text{K}$ Feshbach molecules with 80 kHz binding energy at a temperature of 100 nK. To perform photoassociation spectroscopy on these molecules, we use a widely tunable titanium-sapphire (TiSa) laser as the light source for the photoassociation process. The TiSa laser has a tunable wavelength range that covers all three excited states of interest. Three excited state manifolds are characterized in the previous Fermi 1 work [56], which are

- Triplet-rich excited state, with 92% triplet ($c^3\Sigma^+$) and 8% singlet ($B^1\Pi$) admixture.
- Singlet-rich excited state, with 8% triplet ($c^3\Sigma^+$) and 92% singlet ($B^1\Pi$) admixture.
- Balanced excited state, with 64% triplet ($c^3\Sigma^+$) and 36% singlet ($B^1\Pi$) admixture.

The frequency of the photoassociation laser can be controlled by adjusting the voltage of the TiSa piezo, which effectively changes the length of the laser cavity. The frequency of the photoassociation laser is read out and recorded by a high-precision wavemeter with an accuracy of ± 0.5 MHz. The photoassociation optical pulse is gated by a mechanical shutter and an acoustic-optical modulator (AOM). The photoassociation laser irradiates Feshbach molecules for $55\ \mu\text{s}$. During the $55\ \mu\text{s}$ photoassociation window, Feshbach molecules are promoted to electronically excited states, which rapidly decay down to lower bound states via spontaneous emission. The number of excited state molecules created by the photoassociation process is measured through Feshbach molecule losses. Here we choose to perform photoassociation spectroscopy between 80 kHz bound Feshbach molecules and the balanced excited state manifold. Figure 3-2a shows the photoassociation spectrum of Feshbach molecules with the laser in horizontal polarization, which is perpendicular to the magnetic field, driving $\Delta m_F = \pm 1$, or the ' σ^\pm ' transitions. Figure 3-2b shows the spectrum

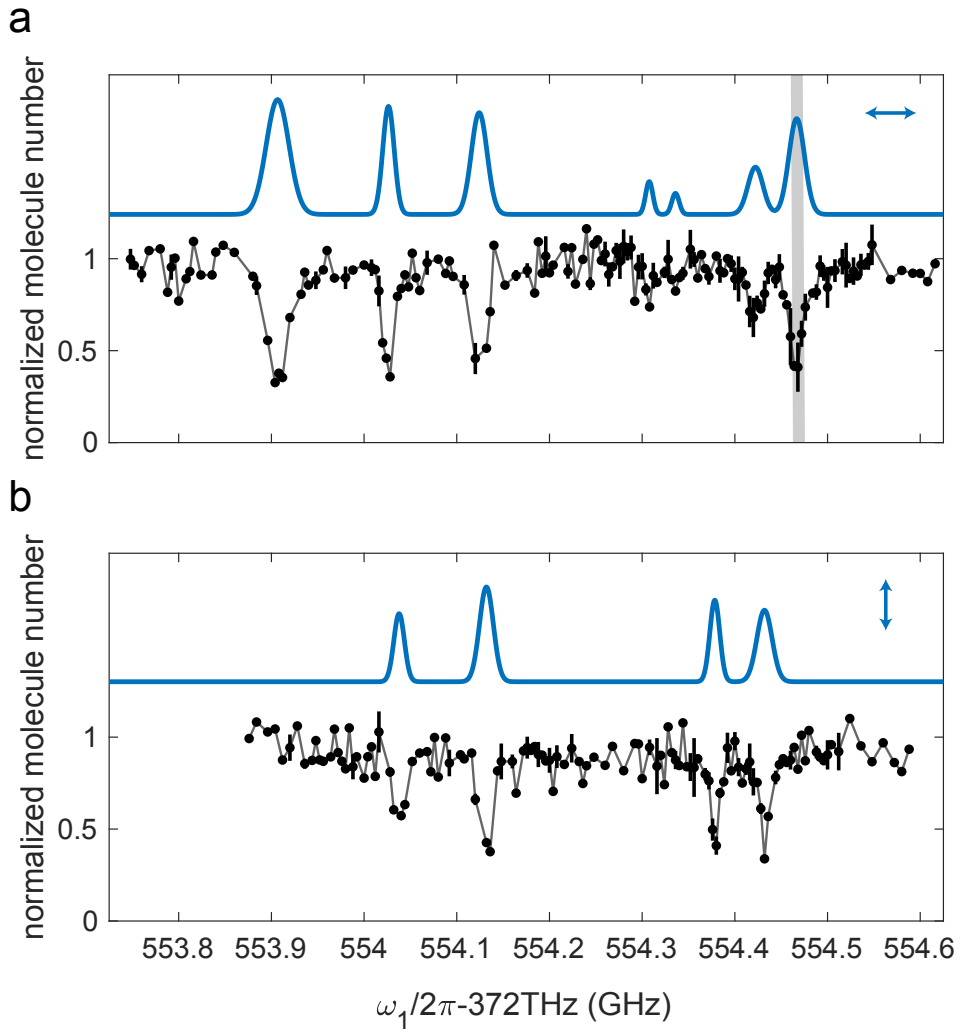


Figure 3-2: Photoassociation spectroscopy of $^{23}\text{Na}^{40}\text{K}$ Feshbach molecules, a. with laser in horizontal polarization and b. in vertical polarization. The quantization axis is provided by the vertically oriented uniform magnetic field. As the photoassociation laser comes from the side of the chamber shown in Fig. 1-5, vertical polarization drives the π transition ($\Delta m_F = 0$), while horizontal polarization drives both σ^\pm transitions ($\Delta m_F = \pm 1$). The black data points represent the number of molecules created, normalized by the population when the photoassociation laser is off-resonant, and the blue lines show multiple Gaussian fits to the data. Comparing the spectra in a and b, we observe that the $\Delta m_F = 0$ or ± 1 transitions are promoted or suppressed depending on the photoassociation laser polarization, which agrees well with the assigned transitions in our previous work [56]. Starting from the initial Feshbach molecule in the hyperfine $m_F = -7/2$ state, we typically choose the transition highlighted in gray to create the absolute ground state molecule in the hyperfine $m_F = -5/2$ state.

with the photoassociation laser in vertical polarization, driving $\Delta m_F = 0$, or the ‘ π ’ transitions. Starting from the initial Feshbach molecule that is in the hyperfine $m_F = m_F^{Na} + m_F^K = -7/2$ state, the transition highlighted in Fig. 3-2 is typically chosen to create the absolute ground state molecule that is in hyperfine $m_F = -5/2$ state [57]. The next section characterizes the photoassociation coupling strength of this highlighted transition.

3.3.1 Feshbach molecule photoassociation coupling strength

A rapid photoassociation coupling rate is critical for creating ground state molecules, as it allows for adiabatic population transfer within a limited coherence time window. To ensure optimal spatial alignment, we overlap the photoassociation laser with its counter-propagating ODT beam by trapping of ^{40}K atoms. In the absence of ^{23}Na , ^{40}K atoms are stably trapped in the 372 THz light field. To maintain high laser stability during the measurement of Feshbach molecule photoassociation coupling strength, we lock the TiSa laser to the ULE cavity using the Pound-Drever-Hall (PDH) technique [28]. The laser frequency is set to be resonant with the transition highlighted in Fig. 3-2a. We employ a double pass AOM, as shown in Fig. A-1, to bridge the frequency difference between a ULE cavity lock mode and the photoassociation transition of interest. Fig. 3-3 shows the resonant photoassociation coupling strength measurement by varying photoassociation time. The number of remaining $^{23}\text{Na}^{40}\text{K}$ Feshbach molecules follows an exponential time decay, as a result of Fermi’s golden rule: $N(t) = N_0 e^{-\Gamma t}$, where $\Gamma = \Omega_1^2/\gamma_e$ is the coupling rate derived from Eqn. 3.2. In Fig. 3-3d, we demonstrate the fastest photoassociative coupling rate achieved at 6.9 kW/cm² laser intensity (1 W optical power), resulting in an exponential decay constant of $\tau = 0.94 \mu\text{s}$. From this, we estimate the photoassociation Rabi rate to be $\Omega_1 = (2\pi)1.2 \text{ MHz}/\sqrt{\text{kW/cm}^2}$, consistent with values reported in our previous works [56, 57]. Next, we explore photoassociation of Bose polaron quasi-particles, using the technique developed here for Feshbach molecules.

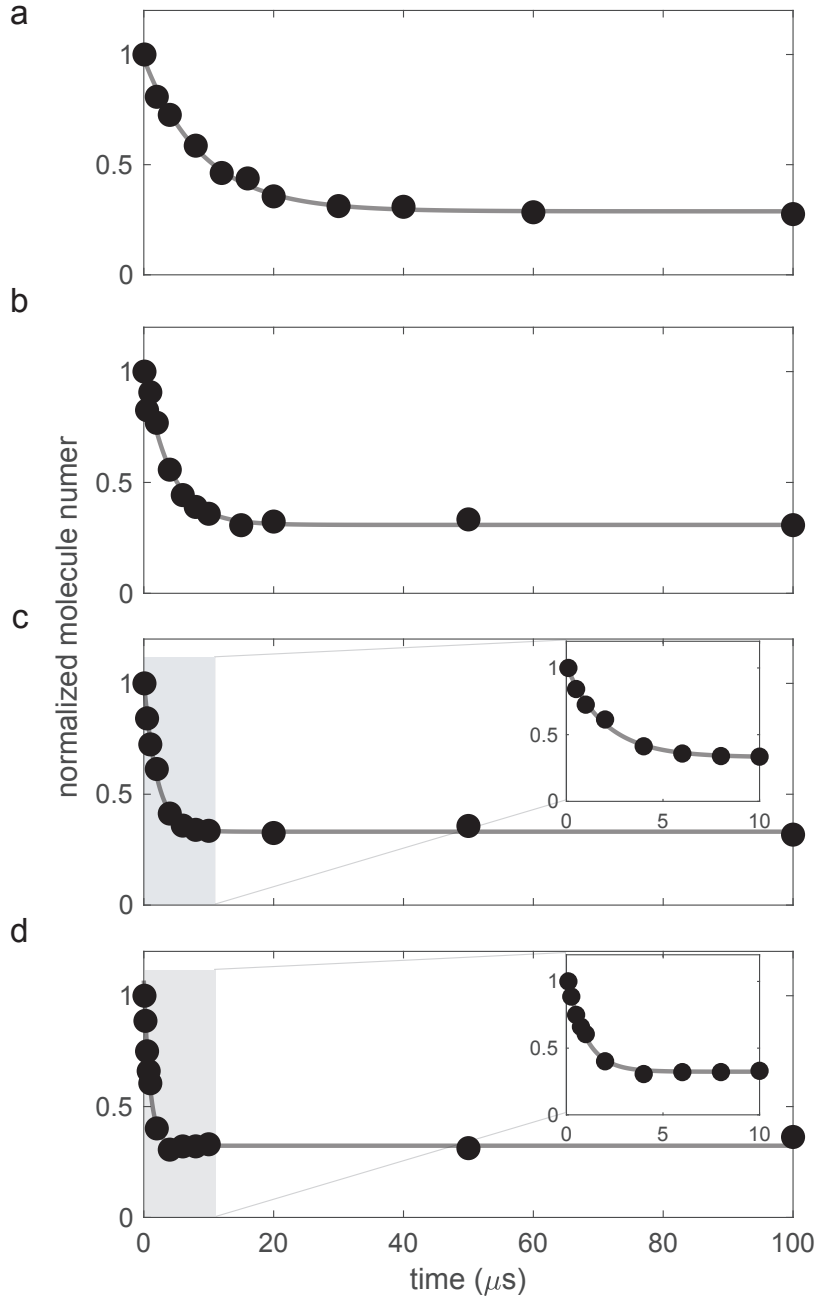


Figure 3-3: $^{23}\text{Na}^{40}\text{K}$ Feshbach molecules photoassociation time dynamics. The photoassociation laser is locked to the ULE cavity in horizontal polarization at a frequency that resonates with the transition highlighted in Fig. 3-2. We choose four different optical power levels for the laser, shown in a. 230 mW (1.6 kW/cm²), b. 530 mW (3.7 kW/cm²), c. 730 mW (5.0 kW/cm²), and d. 1 W (6.9 kW/cm²), to demonstrate the photoassociation time dynamics. Insets in c and d are included to better resolve the photoassociation data at short times, within the 0 to 10 μ s range.

3.4 Photoassociating a quasi-particle

In this section, we investigate the photoassociation properties of an attractively interacting Bose-Fermi mixture using the same technique developed for Feshbach molecules. At fermionic impurity limit, the Bose-Fermi mixture can be described as Bose polaron quasi-particles. Polarons can be intuitively pictured as Feshbach molecules dressed by the surrounding bosonic bath. Unlike weakly-bound Feshbach molecules that are well-defined bound states, the molecular properties of a Bose polaron purely come from its interaction with the bosonic bath. The quasi-particle self-energy characterizes the polaron molecular size, which depends on the inter-species interaction strength and the dressing bath density. Notably, we observe a fifty-fold increase in the polaron photoassociation formation rate from the weakly to the strongly interacting regime. To create ground state molecules via STIRAP, it is crucial to have a strong photoassociation coupling strength and stable initial states. We compare the photoassociation rate and lifetime of attractively interacting Bose polarons to Feshbach molecules, which are the de facto initial states for creating ground molecules in bi-alkali experiments. However, Feshbach molecules suffer from rapid three-body losses in a high-density boson environment, despite their favorable photoassociation coupling rate as we demonstrated in the last section. In contrast, attractively interacting Bose polarons have a sufficient photoassociation coupling to the excited state, and orders of magnitude long lifetime than Feshbach molecules in the same bosonic bath, even in the near unitarity-limited interaction regime. Therefore, the attractively interacting Bose polaron is in a Goldilocks region for creating ground state molecules inside a BEC.

3.5 Polaron photoassociation spectrum

We start with Bose-Fermi mixture with atoms at their respective ground hyperfine states $|1, 1\rangle$ and $|9/2, -9/2\rangle$. After the evaporative cooling in ODT trap, we prepare the mixture at temperature $T \approx 70$ nK with trapping frequencies $(\omega_x, \omega_y, \omega_z)/2\pi =$

(120, 116, 10) Hz. A magnetic field gradient is applied to levitate both species, which cancels the gravitational sag due to ^{23}Na ^{40}K mass difference. As a result, fermions are fully immersed with bosons at 81 G where three-body losses between ^{23}Na ^{40}K mixture are minimal. By controlling the initial atom loading time, we can create mixtures in two regimes: 1. ^{23}Na atoms form a BEC ($T/T_c = 0.1$) with peak density $n_B = 7 \times 10^{13} \text{ cm}^{-3}$, along with fermionic ^{40}K peak density $n_F = 2 \times 10^{11} \text{ cm}^{-3}$, 2. thermal bosons ($T/T_c = 2$) that are not dense enough to form a BEC with boson peak density $n_B = 1 \times 10^{12} \text{ cm}^{-3}$ and fermion peak density $n_F = 3 \times 10^{12} \text{ cm}^{-3}$. The magnetic field is then ramped to its final value near the Feshbach resonance at 78.4 G, where the inter-species scattering length can be tuned from $a = -500$ to -3100 a_o . We are able to explore a range of interaction strengths from $(k_n a)^{-1} = -2.5$ to -0.3 by precisely controlling the boson density n_B and scattering length a , where $k_n = (6\pi^2 n_B)^{1/3}$ represents the inter-boson distance. Following a 2 ms thermalization time, the attractively interacting mixture is illuminated by the TiSa laser in horizontal polarization. The vertical magnetic field is perpendicular to the laser polarization, allowing pairs of atoms to be photoexcited to excited molecules via σ^\pm transitions ($\Delta m_F = \pm 1$). The wavemeter is periodically calibrated to a potassium spectroscopy lock cell for experimental accuracy. The experimental parameters, summarized in Table 3.1, are chosen to resolve the sub-structures of the ^{23}Na ^{40}K electronically excited states. Fig. 3-4 shows the photoassociation spectra of a. triplet-rich, b. balanced, and c. singlet-rich excited states. The gray shaded transitions in Fig. 3-4 correspond to the transitions with the highest coupling rate within each excited state, and their linear and nonlinear photoassociation response are further investigated in later sections.

The photoassociation spectra of the attractively interacting mixture exhibit similar overall structures to those of Feshbach molecules, as previously observed [56]. However, we do not observe a clean suppression or promotion of transitions from a change in laser polarization, as clearly seen in Fig. 3-2 for Feshbach molecules, indicating that attractively interacting Bose polarons have a different spin structure than Feshbach molecules. We photoassociate attractively interacting Bose polaron to the

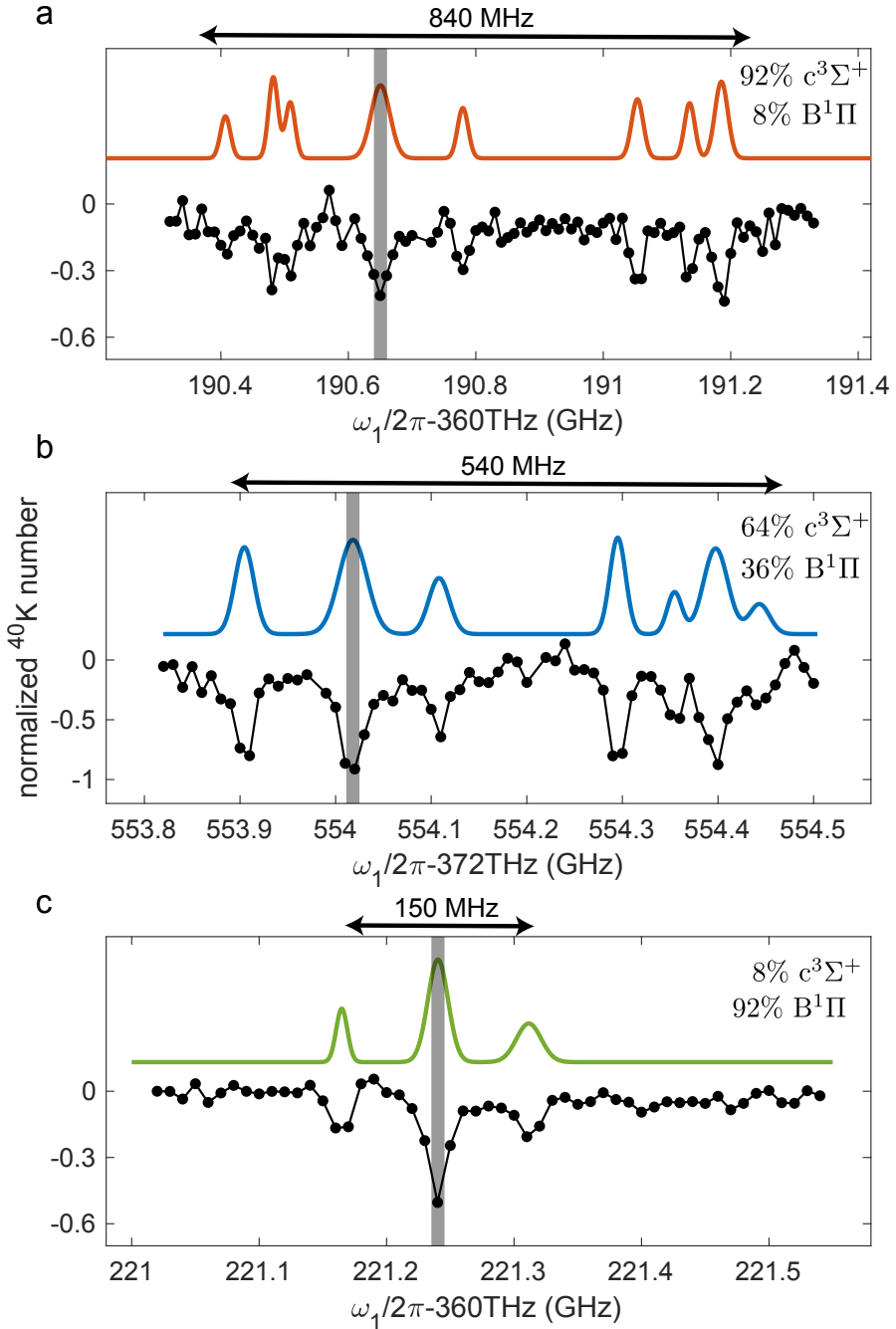


Figure 3-4: Photoassociation spectra of attractively interacting Bose-Fermi mixture. We resolve hyperfine structure of three different excited state manifolds with photoassociation laser in horizontal polarization. The triplet, balanced, and singlet dominated manifold spectra are shown in a, b, c respectively. Colored lines are multiple Gaussian fits to the data. Gray shades indicates hyperfine transitions that are studied later in detail. Experiment parameters are summarized in Table. 3.1.

	n_B (cm $^{-3}$)	n_F (cm $^{-3}$)	I (kW/cm 2)	t_{PA} (μ s)	a (a_o)
a	1×10^{12}	3×10^{12}	2.8	10	-3100
b	6×10^{13}	1×10^{12}	0.7	50	-1000
c	1×10^{12}	3×10^{12}	0.3	4000	-3100

Table 3.1: Experimental parameters associated with Fig. 3-4 photoassociation spectrum. The mixture density scattering length are chosen to resolve all subfeatures in each excited state manifold, which results different photoassociation time and laser intensity.

balanced excited state, as shown in Fig. 3-5a with laser in horizontal polarization, and shown in Fig. 3-5b with laser in vertical polarization. This lack of clear polarization selection rules for photoassociating attractively interacting Bose polarons, as compared to Feshbach molecules, is an intriguing difference that deserves further theoretical investigation. In the next section, we systematically study photoassociation linear response of the transitions that have the highest coupling rate in each excited state manifold.

3.6 Photoassociative linear response

To study the photoassociation linear response, we prepare a dilute Bose-Fermi mixture at temperature $T \approx 70$ nK with fermion peak density $n_F = 3 \times 10^{12}$ cm $^{-3}$, and boson peak density $n_B = 1 \times 10^{12}$ cm $^{-3}$. The mixture is intentionally chosen to be above the boson condensate phase transition temperature T_c (with $T/T_c = 2$) to ensure that the system is in a thermal state. Thus, we refer to the system as a ‘thermal’ mixture, or ‘thermal’ bosons, to distinguish it from a ‘dense’ mixture where a Bose-Einstein condensate (BEC) is formed. The dilute mixture, with inter-species scattering length $a = -3100 a_o$, has a long lifetime $\tau > 1$ s, which is well suited to study the photoassociation linear response in the perturbative regime. The polaron variational approach, which describes the polaron as a dressed molecule, remains valid at this weakly interacting regime. We lock the TiSa laser to the ULE cavity to realize high spectral resolution and laser frequency stability. The $^{23}\text{Na}^{40}\text{K}$ mixture undergoes photoassociation processes during a 400 μ s time window before the remaining atoms

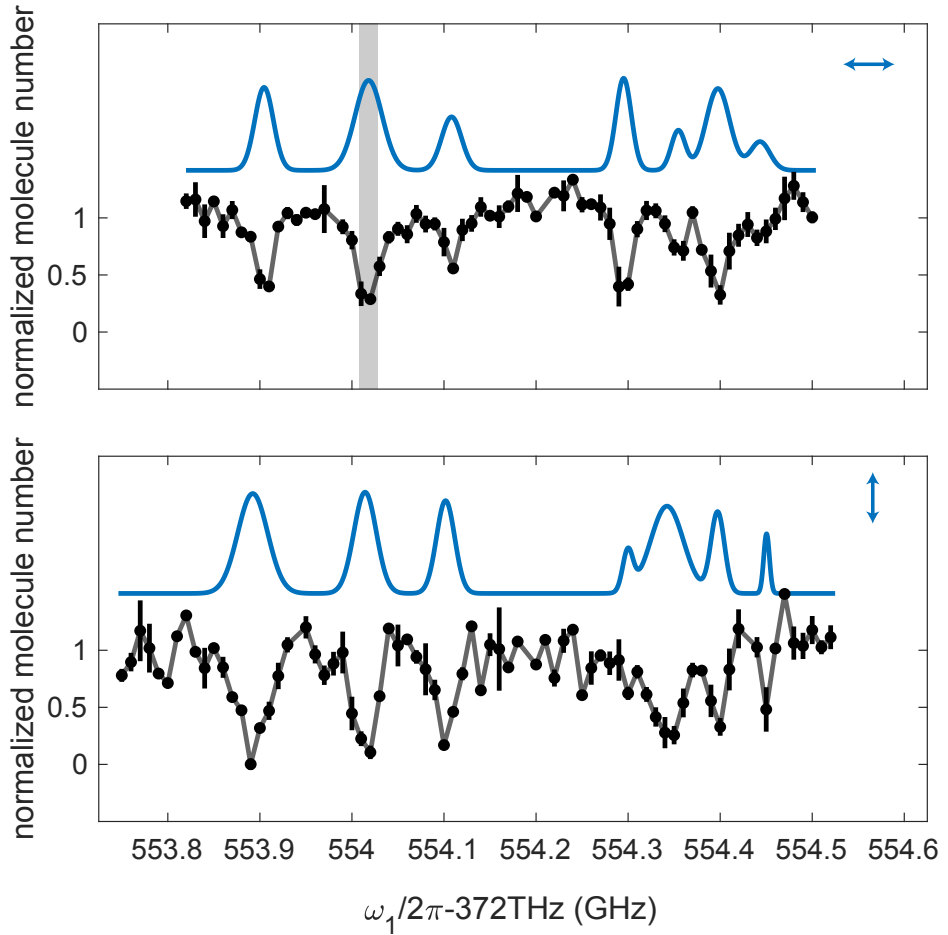


Figure 3-5: Photoassociation spectroscopy of attractively interacting $^{23}\text{Na}^{40}\text{K}$ mixture with TiSa laser in a. horizontal b. vertical polarization. During the $50 \mu\text{s}$ photoassociation window, atom pairs in attractively interacting Bose-Fermi mixture are photoexcited to the balanced electronically excited state, which has an admixture of 64% $c^3\Sigma^+$ 36% $B^1\Pi$. The photoassociation laser polarization is controlled using a Glan-Thompson polarizer, followed by $\lambda/2$ and $\lambda/4$ waveplates for final orientation of the polarization of the light field. However, unlike the Feshbach molecules as shown in Fig. 3-2, we do not observe any discernible change in the photoassociation spectra when the laser polarization is varied, indicating a difference in spin structure between attractively interacting Bose polarons and Feshbach molecules.

are imaged. Fig. 3-6 shows the linear response of number of excited state molecules created by varying the photoassociation laser intensities. The inset in the figure shows the relative linear photoassociation rate as a function of detuning, which is fitted to a Lorentzian lineshape. The relative photoassociation rate is related to the excited state triplet admixture, which arises due to the Franck-Condon principle and the molecular nature of the mixture. The $^{23}\text{Na}|1, 1\rangle$ and $^{40}\text{K}|9/2, -9/2\rangle$ state Feshbach molecules are identified to have mixed 14% singlet and 86% triplet admixture [83]. The weak dressing of the polaron leads to an inheritance of the molecular character from the Feshbach molecule, which in turn facilitates photoassociative formation. This explains the rough proportionality of the linear response rate of the photoassociation to the excited state triplet component admixture. The next section explores photoassociation at higher laser intensity where we observe nonlinear response.

3.7 Nonlinear response: continuum participation

Within the variational description of Bose-Fermi mixture, the attractive polaron is the system ground state, which is energetically below the free-particle continuum. However, in comparison to Feshbach molecules, attractive polarons are much closer to the continuum. The photoassociation laser is near resonant with the continuum, which causes the mixing of the nearby continuum with the excited state and leads to nonlinear photoassociative effects [9, 63]. This laser-induced mixing results in an effective lowering of the excited state, leading to frequency red-shifts that are linearly dependent on the intensity of the photoassociation laser. This spectral shift to lower frequency is demonstrated in Fig. ???. Fig. 3-7 demonstrates the laser induced mixing leads to nonlinear photoassociation effects in response to laser intensity and detunings among 3 electronically excited states. A semi-analytic model based on [9] qualitatively captures the saturation and suppression of photoassociative formation rate above the saturation intensity I_{sat} ,

$$K_p = K_{max} \frac{II_{sat}}{(C_\Delta \Delta + C_{E1} I)^2 + (\frac{I+I_{sat}}{2})^2} \quad (3.3)$$

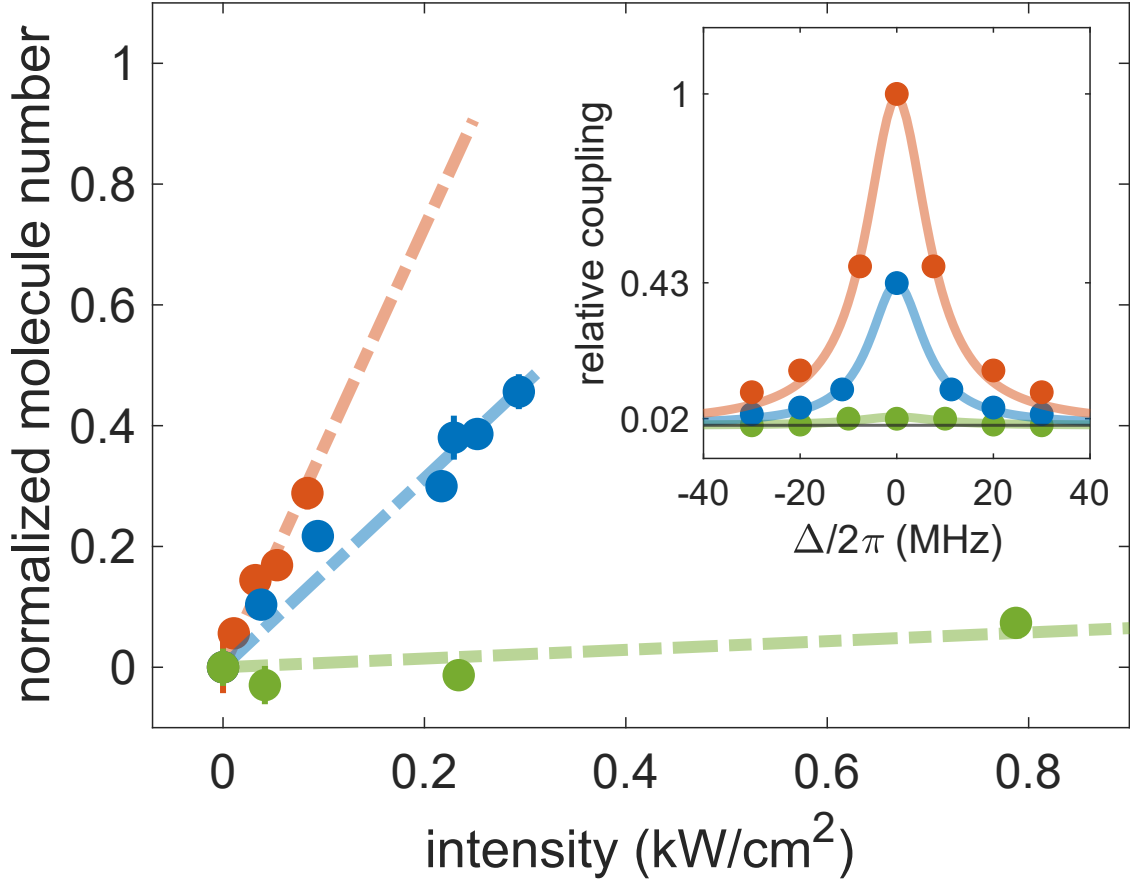


Figure 3-6: Photoassociation linear response of three excited state manifolds. photo-toassociation laser frequencies are on resonant with gray shaded shown in Fig. 3-4: orange, blue, green stand for triplet-rich, balanced, singlet-rich excited states respectively. We prepare the thermal Bose-Fermi mixture with $n_B = 1 \times 10^{12}$ $n_F = 3 \times 10^{12}$ cm^{-3} at temperature $T = 70$ nK with inter-species interaction length of -3100 a_o . We expose the mixture for 400 μs to the photoassociation laser and scan the laser intensity. Linear lines fit the number of molecules created via the photoassociation process, which gives resonant photoassociation coupling rates of 9.1 , 3.9 , 1.2 Hz/(W cm^2) for triplet-rich, balanced, and singlet-rich excited states respectively. The inset shows the relative photoassociation coupling rates measured at various laser detunings which are fitted to Lorentzian lineshapes. Since we only change the excited state character and keep the initial state the same, the photoassociation rates are predicted to be proportional to Franck-Condon factor f_c^2 as a result of the Franck-Condon principle.

I represents the photoassociation laser intensity that is experimentally controlled by an AOM. I_{sat} is the saturation intensity that is proportional to the excited state linewidth γ_e . C_{E1} describes the energy shift induced by the photoassociation laser and the free-particle continuum, while C_Δ takes into account the effect of photoassociation laser detuning Δ . The fitted parameters are summarized in the Table 3.2 below. The triplet-rich excited state has the highest coupling to the initial state, but it also experiences the strongest influence from the continuum. Conversely, the singlet-rich excited state experiences minimal continuum influence but has the weakest coupling to the initial polaron state. The balanced excited state lies in the middle ground, with strong coupling to the initial state and not under strong influence from the continuum. We believe that the potential of the triplet-rich excited state can be realized in Feshbach molecules that are far away from the free-particle continuum. Nevertheless, Feshbach molecules are less stable compared to polarons in the presence of background bosons, which will be discussed in Section 3.9. Taking into account all of the above constraints, we have identified the balanced excited state as the optimal intermediate bridge for photoassociating attractively interacting polarons and ultimately creating ground state molecules within a dense boson environment. In the next section, we bring the mixture to strongly interacting regime by forming a BEC, which drastically enhances the photoassociation rate.

Exited state manifold	K_{max} (kHz)	I_{sat} (kW/cm ²)	C_{E1}
Triplet	4(1)	2.8(0.4)	4.1(0.5)
Balanced	3(1)	2.9(0.5)	1.9(0.1)
Singlet	0.95(0.1)	8.5(1)	0.5(0.6)

Table 3.2: Summary of fit results shown in Fig. 3-7. Numbers in the parenthesis are standard deviations of fit results from 4 detunings.

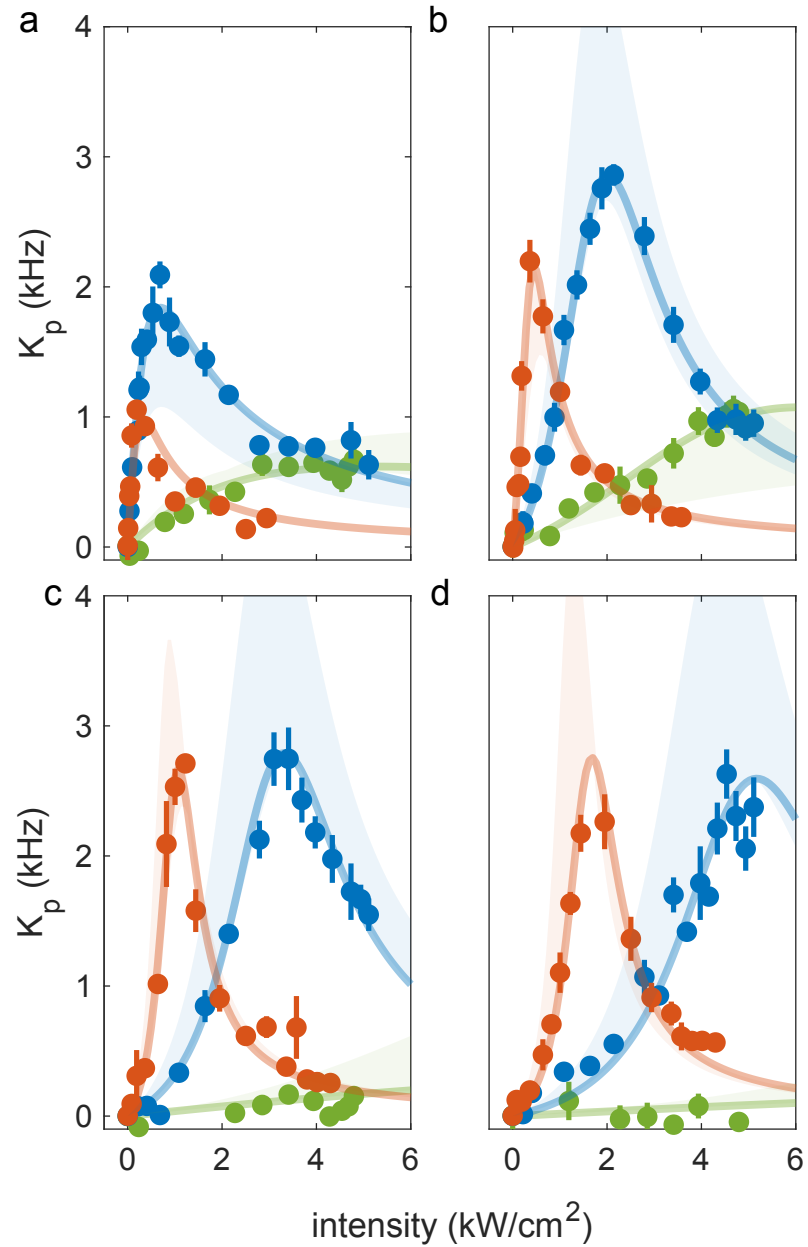


Figure 3-7: Nonlinear photoassociation response of attractively interacting Bose-Fermi mixture. Photoassociative response at high optical intensity displays nonlinear behavior, as a result of the free-particle continuum participation in the photoassociation process. a, b, c, and d show photoassociative formation rate K_p at detunings of $\Delta/2\pi = 0, -11.3, -20, -30$ MHz for the balanced excited state transition in blue, and $\Delta/2\pi = 0, -7.6, -20, -30$ MHz for the triplet-rich (singlet-rich) excited state transition in orange (green). Solid lines are fits based on Eqn. 3.3, which is a semi-analytic model derived by authors in [9]. The shaded region illustrates the deviation of the fit results from the experimental data obtained at 4 different detunings. See Table 3.2 for fit results summary.

3.8 Photoassociation enhancement from strong interaction

In this section, we present our experimental results that strong inter-species interaction strength greatly enhances the photoassociative formation rate. To understand this enhancement, we use a simple dressed molecule picture, which is based on the variational approach [49], to describe the polaron wavefunction. The dressed molecule is a superposition of molecule wavefunction $|\psi_m\rangle$, which has the same character as a weakly-bound Feshbach molecule, and delocalized free-particle component $|\psi_f\rangle$:

$$|\psi_p\rangle = Z^{1/2} |\psi_f\rangle + (1 - Z)^{1/2} |\psi_m\rangle. \quad (3.4)$$

The polaron quasi-particle residue Z describes the free-particle character of the dressed molecule, which can be experimentally varied by the inter-species interaction strength. We use a unitless parameter $(k_n a)^{-1}$ to characterize the system interaction strength, where $k_n = (6\pi^2 n_B)^{1/3}$ is the inverse inter-boson distance. Larger scattering length a , higher bosonic density n_B brings the system closer to the interaction unitarity at $(k_n a)^{-1} \rightarrow 0$. As the mixture reaches interaction unitarity $(k_n a)^{-1} \rightarrow 0$, the Bose polaron gains its quasi-particle self energy E_p , and becomes more like a molecule, less of free particles. The dressed molecule size r is determined by the polaron self-energy $E_p = -\hbar^2 / 2m_r r^2$. A smaller dressed molecule size results in a better Franck-Condon overlap with the electronically excited molecule, which leads to a stronger coupling rate for photoassociation. Fig. 3-8 shows the measurement of photoassociation coupling rate across the Feshbach resonance landscape. The blue data points represent the photoassociative formation rate γ of attractive polarons, while the black data points represent Feshbach molecules with 80 kHz binding energy. The blue line is quasi-particle residue scaled by Feshbach molecule photoassociation rate $\gamma_m(1 - Z)$, which qualitatively connects the photoassociation rate from attractively interacting polaron to the Feshbach molecule. We would like to highlight the significant enhancement in the photoassociative formation rate observed between polarons, as shown in

the inset of Fig. 3-8a and b. At the same scattering length of $a = -3000 a_o$ and temperature of $T \approx 70$ nK, increasing the boson density from 1×10^{12} to 7×10^{13} cm $^{-3}$, where the bosons form a $T/T_c = 0.1$ BEC, leads to a ten-fold increase in the photoassociative formation rate. In contrast to polarons, we can only form Feshbach molecules in a dilute boson environment, shown in Fig. 3-8c, because Feshbach molecules suffer rapid inelastic collisions with bosons, which we will discuss in the next section.

3.9 Inelastic loss rate

Strong inter-species interactions that increase mixture photoassociative formation rate also bring unwanted inelastic collisions, which lead to three-body losses. At negative scattering lengths, or attractive interactions, the probability of inelastic collisions between two bosons and a fermion increases near unitarity, leading to the formation of a $^{23}\text{Na}^{40}\text{K}$ molecule and a ^{40}K atom with a large kinetic energy released from the binding of the molecule.

$$\frac{dn_F}{dt} = -L_3 n_B^2 n_F = -\tau_p^{-1} n_F \quad (3.5)$$

At positive scattering length, a weakly-bound $^{23}\text{Na}^{40}\text{K}$ Feshbach molecule can undergo inelastic collisions with a ^{23}Na boson, leading to the molecule decaying into deep-bound $^{23}\text{Na}^{40}\text{K}$ via vibrational relaxation mechanism.

$$\frac{dn_m}{dt} = -\beta_m n_B n_m = -\tau_m^{-1} n_m \quad (3.6)$$

We extract the loss coefficient by measuring the mixture lifetime at different interaction strengths. As we perform measurements in the boson majority limit, we do not observe any change in ^{23}Na population during the measurement. Therefore, we treat n_B as a constant. We scale L_3 by the boson density, $\beta_p = L_3 n_B$, in order to compare the loss coefficient between attractive polarons and Feshbach molecules on the same scale. Fig. 3-9 summarizes the measurements of the loss rate as a function of $(k_n a)^{-1}$.

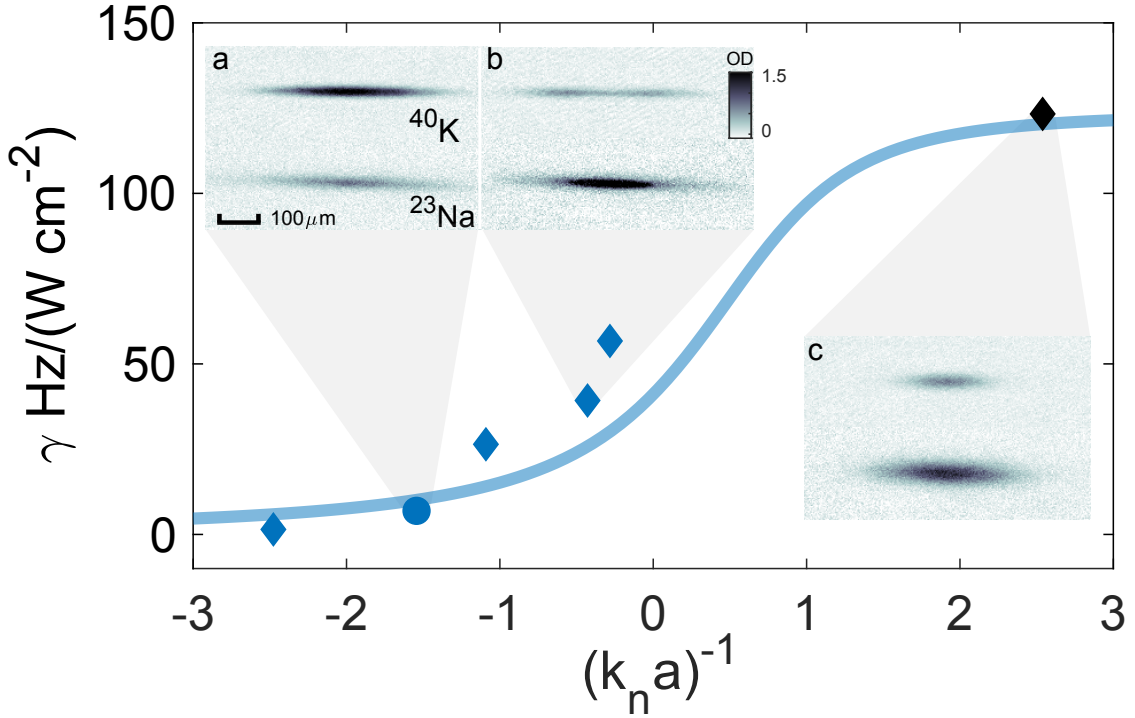


Figure 3-8: Photoassociative formation rate γ of attractively interacting polarons and weakly-bound Feshbach molecules. The black diamond represents the photoassociation rate of Feshbach molecules with 80 kHz binding energy. Blue diamond and circle represent photoassociation rate of attractive polaron. The circles and diamonds represent two methods used to measure the photoassociation rates: the circles represent the photoassociation rate extracted from an exponential fit to the photoassociation time evolution, while the diamonds represent the photoassociation linear response shown in Fig. 3-6. The blue line, based on the variational description of the polaron, smoothly connects γ from the attractive polaron to the Feshbach molecule. Exemplary absorption images of the $^{23}\text{Na}^{40}\text{K}$ mixture at different interaction strengths are shown in the inset panels a, b, and c, corresponding to $(k_n a)^{-1} = -1.5, -0.4, +2.5$, respectively.

The solid blue line in Fig. 3-9 represents the loss rate coefficient β_p as a function of scattering length a in the negative scattering regime. The data is fit to the relationship $\beta_p = n_B L_3 \propto n_B a^2$, where n_B is the boson density and L_3 is the three-body loss coefficient. The loss rate β_p does not diverge at unitarity $(k_n a)^{-1} = 0$, where scattering length converges to the inter-boson distance $a \rightarrow k_n^{-1}$. Feshbach molecules, which only exist at positive scattering length, are weakly-bound dimers having molecular size approximately to the scattering length a . The Feshbach molecule binding energy E_b is inverse proportional to a^2 : $E_b = \hbar/(2m_r a^2)$ where $m_r = \frac{m_B m_F}{m_B + m_F}$ is the reduced $^{23}\text{Na}^{40}\text{K}$ mass. Smaller Feshbach molecules, that are further away from the resonance, have better vibrational wavefunction overlap with deep bound molecular states, which results more rapid atom-dimer loss. The gray solid line in Fig. 3-9 represents the resulting Feshbach molecule loss rate β_m inverse proportional to the molecular size a as $\beta_m \propto a^{-1}$ [26, 27]. It is worth noting that the Feshbach molecule with a binding energy of 80 kHz (black dot in Fig. 3-9) has a loss rate more than two orders of magnitude higher than that of the polaron near unitarity. Despite the favorable photoassociation coupling strength, Feshbach molecules undergo rapid population loss in a dense boson environment, which acts as an obstacle to creating ground state molecules inside a BEC starting from Feshbach molecules. On the other hand, Bose polarons are stable initial state and have strong coupling to the excited state, which are two crucial ingredients for creating ground state molecules. On the other hand, Bose polarons possess two crucial ingredients for creating ground state molecules: a stable initial state and strong coupling to the excited state, making them the ideal starting point for creating ground state molecules within a BEC. In Chapter 5, we demonstrate the experiment realization of ground state molecules directly from strongly interacting Bose polaron.

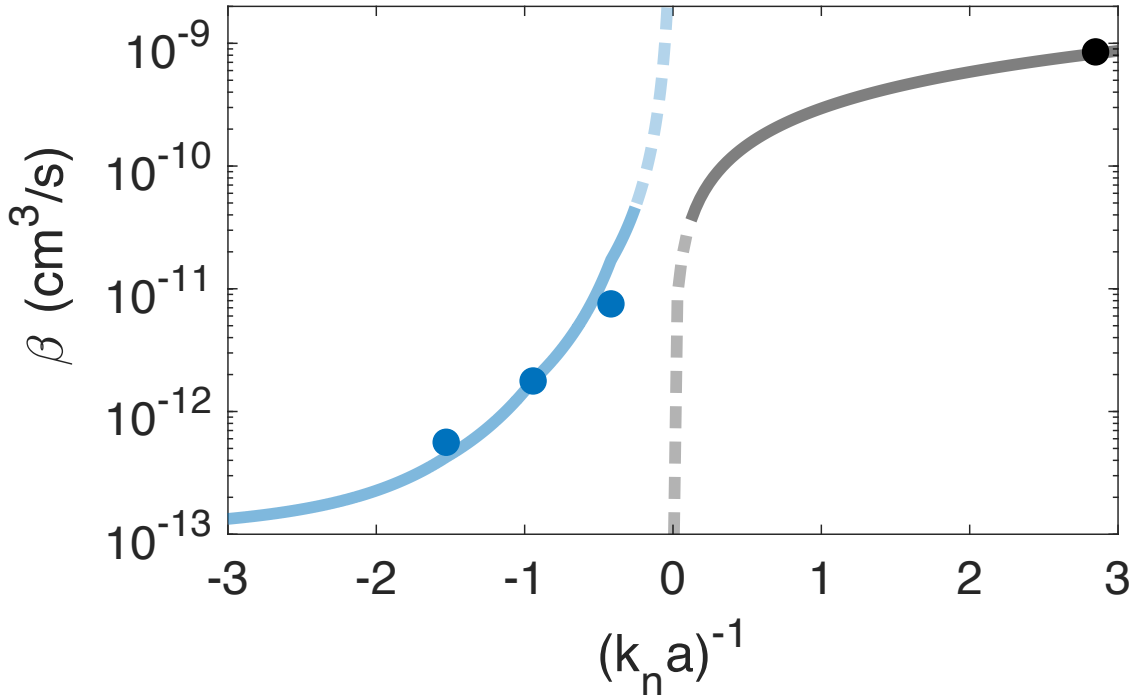


Figure 3-9: The Loss rate β of attractively interacting polarons and weakly-bound Feshbach molecules. The blue and gray lines represent two different loss mechanisms for attractively interacting polarons and Feshbach molecules respectively. At negative scattering lengths, the loss of polarons is attributed to the three-body recombination process. This process involves a three-body complex of 2 bosons and 1 fermion forming a deeply bound molecule, which subsequently releases binding energy that is carried away as kinetic energy share between the molecule and the third boson. The polaron loss rate described in Eqn. 3.5 is extrapolated by a^2 and is represented by the solid blue line. The loss of Feshbach molecules occurs due to vibrational relaxation between the molecule and a second bosonic atom. This atom-dimer loss is represented by the gray line in the figure with $\beta_m \propto a^{-1}$, which is based on the findings of [26]. The loss rate of Feshbach molecules is approximately three orders of magnitude higher than that of polarons, which makes it extremely difficult to create ground state molecules inside a BEC with Feshbach molecules.

Chapter 4

Creating ground state dipolar molecules from Feshbach molecules

In this chapter, we present a road map of creating ground state $^{23}\text{Na}^{40}\text{K}$ dipolar molecules starting from weakly-bound Feshbach molecules. Feshbach molecules exhibit strong coupling to the electronically excited state, enabling efficient transfer to the ground state through coherent two-photon Raman transfer. To mitigate the rapid loss between Feshbach molecules and background bosons, we create Feshbach molecules in a dilute boson environment. We conduct the following $^{23}\text{Na}^{40}\text{K}$ ground state molecule spectroscopy through the balanced excited state that has a mixed character of 64% $c^3\Sigma^+$ 36% $B^1\Pi$. In Section 4.1, we begin by measuring a coarse two-photon resonance of ground state molecules with an accuracy at the level of 10s MHz using Autler-Townes spectroscopy. In Section 4.2, we employ dark resonance spectroscopy to precisely determine the transition frequency from Feshbach molecules to ground state molecules with a precision of kHz level. In Section 4.3, we demonstrate the creation of ground state molecules by observing the coherent time evolution from Feshbach molecules to ground state molecules via Stimulated Raman Adiabatic Passage (STIRAP) process. In Section 4.4, we experimentally determine the lifetime of ground state molecules in the presence of a dilute bosonic background. In Section 4.5, we characterize the atom removal technique using laser beams that are resonant with atoms but invisible to ground state molecules in order to prolong the lifetime

of $^{23}\text{Na}^{40}\text{K}$ ground state molecules and enable future dipolar interactions among ground state molecules. Finally in Section 4.6, we systematically study ways to improve the efficiency of ground state molecule creation, taking into account limitations arising from laser coherence and laser power.

4.1 Autler-Townes spectroscopy

In Chapter 3.3 we have determined the single photon resonances between the initial Feshbach molecule state and the electronically state and produced photoassociation spectrum, which is a depletion signal on Feshbach molecules. The photoassociation resonances exhibit features ≈ 10 MHz that are determined by the excited state natural linewidth. The next scientific step in creating ground state molecules involves the search for the down-leg resonance that couples the excited state to the ground state. We generate the down-leg light using a Coherent 899 ring dye laser that is optically pumped by a high-power 532 nm SproutG laser. The dye laser is frequency locked to its built-in reference cavity to achieve laser frequency stability. The length of the reference cavity is controlled by an external signal which effectively set the down-leg laser frequency. We obtain the frequency of the dye laser from a high-precision wavemeter that is periodically calibrated to the ^{23}Na spectroscopy cell. In our coarse search for the down-leg resonance, we simultaneously illuminate the Feshbach molecules with 57 mW of down-leg and 1 W of up-leg laser light field for a duration of 100 μs . We lock the up-leg laser, which is resonant to the balanced excited state transition as highlighted in Fig. 3-2, to the ULE cavity for ultimate up-leg laser stability. The presence of the down-leg laser field dresses the excited state with the ground state, creating an Autler-Townes splitting with a protection window width of approximately $\frac{\Omega_2^2}{\gamma_e}$, where Ω_2 is the down-leg laser Rabi rate and γ_e is the natural linewidth of the excited state. Fig. 4-1 demonstrates the resulting Autler-Townes spectrum, which features a 32 MHz FWHM wide protection window. Our search of the down-leg resonance is guided by previous Fermi 1 work as reported in [56], which shows excellent agreement with our results. In the next section, we employ dark resonance

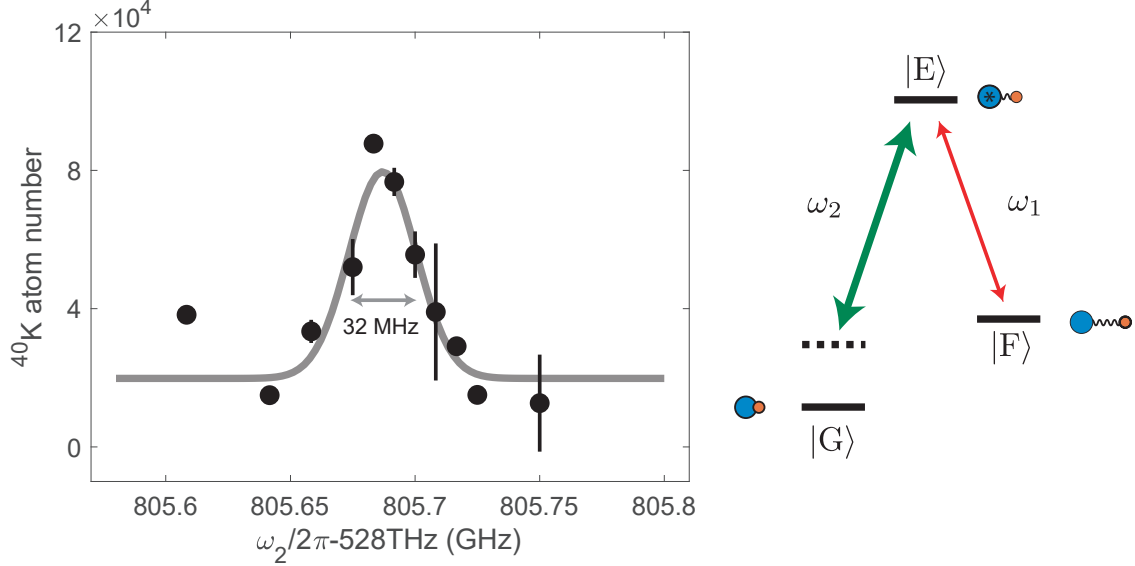


Figure 4-1: Ground state molecule spectroscopy via Autler-Townes splitting. We prepare a sample of 10×10^3 ultracold Feshbach molecules with 80 kHz binding energy at 100 nK temperature. The Feshbach molecules are irradiated with the up-leg laser (ω_1) at 1 W optical power in horizontal polarization, and the down-leg laser (ω_2) at 57 mW optical power in vertical polarization for a duration of 100 μ s. We maintain the up-leg laser resonant with the excited state and scan the frequency of the down-leg laser. During the 100 μ s Autler-Townes spectroscopy time, the down-leg laser creates a 32 MHz FWHM protection window as a result of the splitting of the excited state due to the mixing with the ground state.

spectroscopy to accurately determine the down-leg transition to kHz precision.

4.2 Dark resonance spectroscopy

When the down-leg Rabi rate Ω_2 is reduced to $\Omega_2 < \gamma_e/2$, we enter into the "over-damped" regime, where the protection of the initial Feshbach molecules relies on electromagnetically induced transparency (EIT) [11, 33]. Under the two-photon resonance condition, the dark state $|D\rangle$ is a superposition of the initial Feshbach molecule state $|F\rangle$, and the ground molecule state $|G\rangle$:

$$|D\rangle = \frac{1}{\sqrt{\Omega_1^2 + \Omega_2^2}} (\Omega_2 |F\rangle + \Omega_1 |G\rangle) \quad (4.1)$$

In the regime $\gamma_e/2 > \Omega_2 \gg \Omega_1$, Feshbach molecule state dominates the dark state,

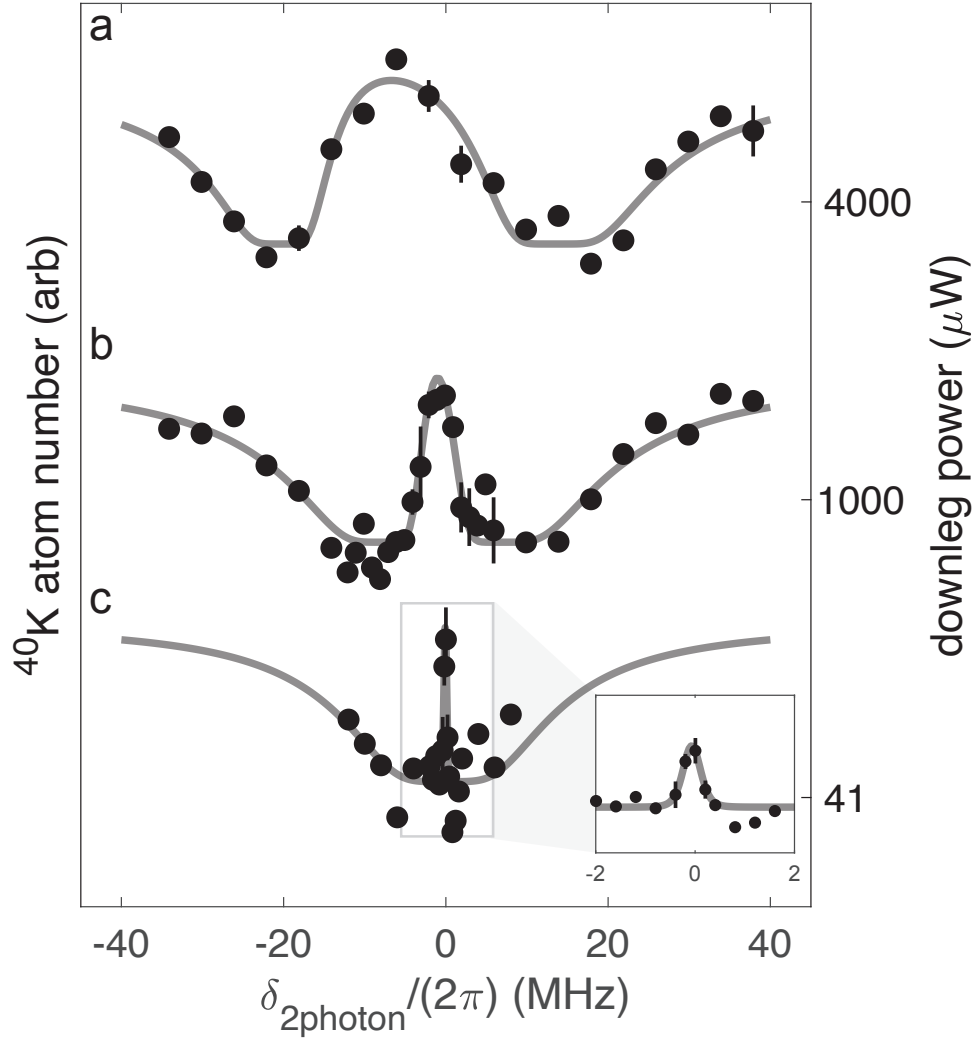


Figure 4-2: Observation of ground state molecules using dark resonance spectroscopy. The Feshbach molecules with an 80 kHz binding energy are illuminated simultaneously by the up-leg and down-leg lasers for 100 μs . The up-leg light field, in horizontal polarization, is resonant with the balanced excited state transition as highlighted in Fig. 3-2. The AOM in the up-leg PDH lock path, which is used to bridge the ULE lock mode transition resonance, is utilized to precisely shift the two-photon resonance frequency δ_{2photon} . The dark resonance spectra are obtained using an up-leg laser power of 50 mW, while varying the down-leg laser power in three different cases: 4 mW, 1 mW, and 41 μW for cases a, b, and c respectively. We image the surviving Feshbach molecules and analyze the observed EIT lineshape using a numerical solution of a three-level system based on the Bergmann STIRAP formalism [7].

which have zero coupling to the dissipative excited state. During the $100 \mu\text{s}$ dark resonance spectroscopy time, the EIT protection window arises from the coherent interference of the up-leg and down-leg lasers. To ensure the highest relative phase coherence between the up-leg and down-leg lasers, we lock both Raman lasers to the same ULE cavity using the Pound-Drever-Hall (PDH) lock technique. To bridge the frequency difference between the single-photon and two-photon resonance, we utilize AOMs to shift the laser frequencies before they enter the PDH lock path. Fig. 4-2 illustrates a series of dark resonance spectra obtained with three different down-leg laser powers, where the two-photon resonance frequency $\delta_{2\text{photon}}$ is varied by tuning the up-leg laser frequency while keeping the down-leg laser frequency fixed. By employing the down-leg laser in vertical polarization to drive the π transition, and the up-leg laser in horizontal polarization to drive the σ^\pm transitions, we identify that the observed EIT protection window corresponds to the absolute ground state $|G1\rangle$, as reported in our previous work in [57]. In Fig. 4-2c, we showcase the narrowest EIT protection windows with a width of approximately 100 kHz.

It is worth noting that the finite coherence time leads to a finite dark state population lifetime. Decoherence sources such as laser phase fluctuations, optical fiber scrambling on phases may contribute to perturb the destructive interference, and subsequently leads to dark state population leaking into dissipative bright states. As shown in Fig. 4-3, we perform coherence time measurements using dark state population time dynamics. We create a dark state that has equal superpositions of Feshbach molecule $|F\rangle$ and ground state molecule $|G\rangle$: $|D\rangle = \frac{1}{\sqrt{2}}(|F\rangle + |G\rangle)$, which is most sensitive to environment decoherence. The experimental data are fitted to a simple exponential decay model, $N_D = N_0 e^{-t/\tau_D}$. The fitting result yields a coherence time of $\tau_D = 63 \mu\text{s}$, which sets a time scale for the completion of coherent population transfer in our experiment. After precisely determining the transition frequency of the ground state molecules using dark resonance spectroscopy and estimating the coherence time of the system, we proceed with creating ground state molecules using coherent two-photon Raman transfer.

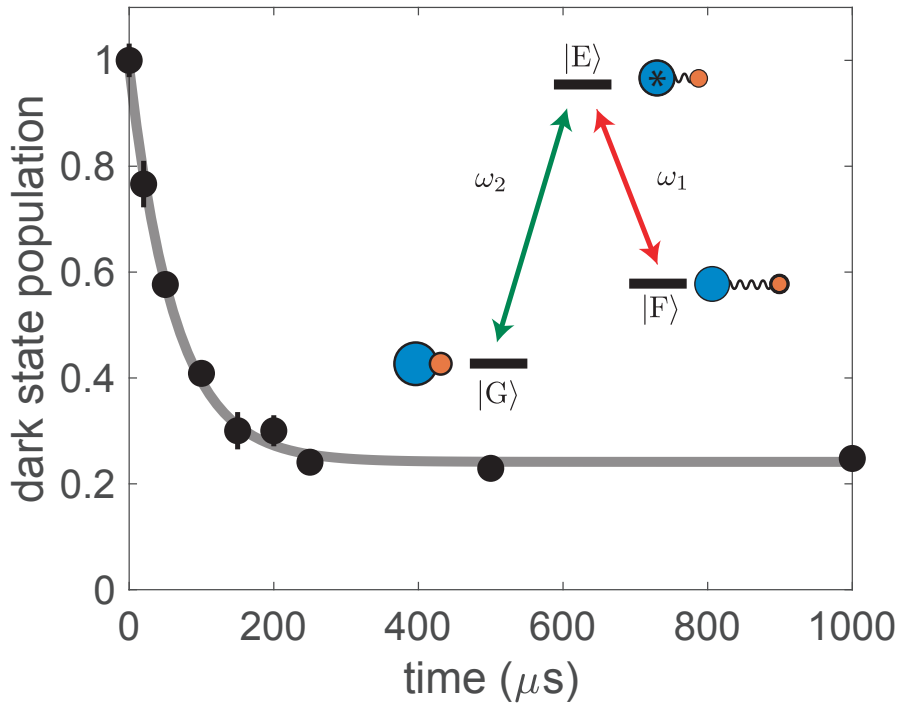


Figure 4-3: Time evolution of dark state population. We create a dark state with equal superposition of ground state molecule and Feshbach molecule $|G\rangle$: $|D\rangle = \frac{1}{\sqrt{2}}(|F\rangle + |G\rangle)$. To create this dark state, we illuminate the initial Feshbach molecules with 417 mW of horizontally polarized up-leg laser light, and 31 μW of vertically polarized down-leg laser light. The dark state population is held inside ODT before the detection where remaining Feshbach molecules are resonantly imaged. The gray line fits the normalized dark state population with a simple exponential time decay, which yields 63 μs exponential constant.

4.3 Coherent two-photon creation of ground state molecules

In dark resonance spectroscopy, the dark state of the system is created as a coherent superposition of bare states that remains "still" or unperturbed, using fixed up-leg and down-leg laser power. In this section, we implement the stimulated Raman adiabatic passage (STIRAP) protocol, that dynamically tilt the dark state to enable population transfer from the initial Feshbach molecule state to the ground state molecules. Due to lack of direct coupling between Feshbach molecules and ground state molecules, the highly dissipative excited state acts as an intermediate bridge for the population transfer. This STIRAP sequence cleverly utilizes the dark state, allowing us to circumvent the dissipative nature of the excited state and achieve efficient conversion of Feshbach molecules to ground state molecules. This is achieved by adiabatically adjusting the partially overlapped up-leg and down-leg lasers. Fig. 4-4a displays the up-leg and down-leg ramps during the STIRAP time sequence, which adiabatically tilt the dark state

$$|D\rangle = \frac{1}{\sqrt{\Omega_1^2 + \Omega_2}}(\Omega_2 |F\rangle + \Omega_1 |G\rangle) \quad (4.2)$$

To achieve the transfer of Feshbach molecules to ground state molecules, we begin with the down-leg laser at full strength, which places the Feshbach molecule state as the dark state of the system, denoted as $|D\rangle = |F\rangle$. As the strength of the down-leg laser ramps down and the up-leg laser ramps up, the first STIRAP pulse completes with the ground state molecule becoming the dark state of the system, denoted as $|D\rangle = |G\rangle$. Ground state molecules cannot be directly imaged due to the lack of cycling transitions. Therefore, the second STIRAP pulse, which reverses the ramping order of the lasers, transfers the ground state molecules back to Feshbach molecules for detection purposes. Fig. 4-4b illustrates the coherent creation of 4×10^4 ground state molecules at a temperature of 80 nK. After the first STIRAP pulse completes at $t = 20 \mu s$, we observe a decrease in the population of Feshbach molecules, with 65% of them being transferred to the ground state molecules that do not react to

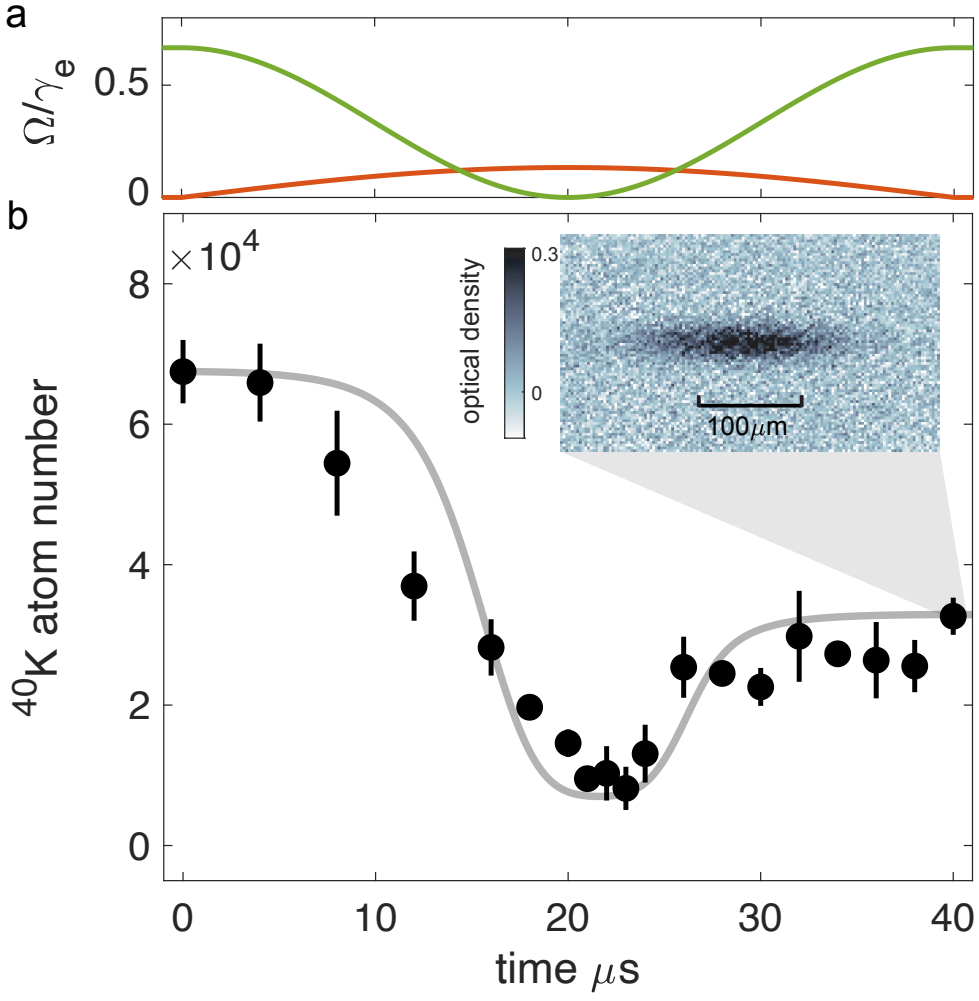


Figure 4-4: Observation of ground state molecule population coherent evolution during the STIRAP ramp. a. Rabi rate of up-leg and down-leg laser during the STIRAP ramp. The up-leg laser, depicted in orange, has a peak Rabi rate of $(2\pi)1.2 \text{ MHz}$, while the down-leg laser, shown in green, has a Rabi rate of $(2\pi)6 \text{ MHz}$. The partially overlapped up-leg and down-leg lasers are utilized to adiabatically tilt the dark state from the initial Feshbach molecules to the ground state within a time duration of $20 \mu\text{s}$. During the second half of the ramp, the ground state molecules are transferred back to Feshbach molecules for imaging. b. Time evolution of Feshbach molecules during the STIRAP sequence. We start our experiment with a population of 7×10^4 Feshbach molecules, which are trapped in the optical dipole trap (ODT) and cooled to a temperature of 80 nK . The population evolution of Feshbach molecules follows the same time axis as the Rabi rates of the Raman lasers, as shown in a. After the first STIRAP pulse at $t = 20 \mu\text{s}$, we successfully create 4×10^4 $^{23}\text{Na}^{40}\text{K}$ ground state molecules with a single trip STIRAP efficiency of 64%. The second STIRAP pulse transfers the ground state molecules back to Feshbach molecules, as illustrated in the inset of the ^{40}K atom absorption image at the end of the STIRAP evolution.

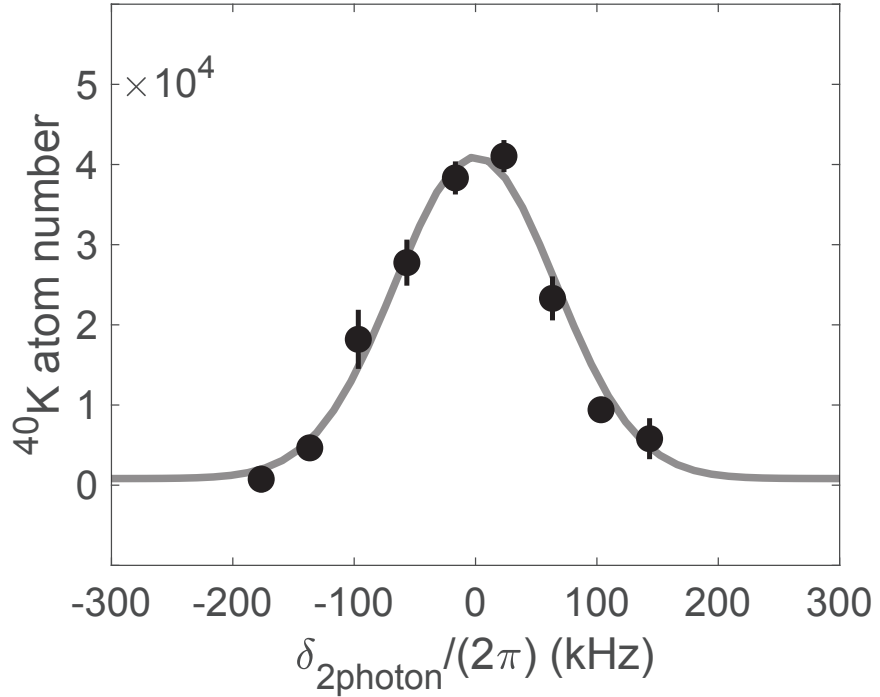


Figure 4-5: Creation of ground state molecules from two-photon spectroscopy of STIRAP. We observe 4×10^4 number of returning Feshbach molecules after STIRAP round trip at the same two-photon resonance condition that we observed in Fig. 4-2. The two-photon resonance is varied by the up-leg laser frequency, while the down-leg laser frequency is maintained at the resonance condition.

absorption imaging light. The ground state molecules later are coherently transferred back into the Feshbach molecules after the second STIRAP trip ends at $t = 40 \mu\text{s}$. An exemplary absorption image of the ${}^{40}\text{K}$ is shown in Fig. 4-4 at the end of the STIRAP round trip.

The successful creation of ground state molecules via STIRAP relies on the system being in the dark state, which is facilitated under the two-photon resonance condition. To demonstrate the importance of the two-photon resonance condition as a critical element for achieving efficient STIRAP transfer, we vary the frequency of the up-leg laser while keeping the frequency of the down-leg laser constant, and image the returning Feshbach molecules after two STIRAP pulses. Fig. 4-5 shows the spectrum of the STIRAP two-photon resonance centered at the same frequency as the EIT

protection window shown in Fig. 4-2. The STIRAP two-photon resonance lineshape has $(2\pi)160$ kHz FWHM width which is related to the effective Rabi rate Ω_* of the Raman lasers, STIRAP pulse duration τ_* , and the excited state dissipation rate γ_e . These parameters together create the STIRAP adiabatic criteria, which determines the figure of merit for resonant STIRAP transfer efficiency: $\eta_{STIRAP} = \exp(-\frac{\pi\gamma_e}{\Omega_*^2\tau_*})$ [89]. Section 4.6 will further systematically characterize the STIRAP efficiency in relation to Ω_* and τ_* . Section 5.7 discusses the STIRAP theory in a greater detail with a dressed state model. In the next section, we study the $^{23}\text{Na}^{40}\text{K}$ ground state molecule stability with the ambient ^{23}Na atoms.

4.4 Ground state molecule lifetime

A stable assembly of dipolar molecules is a crucial prerequisite for realizing the great promise of building many-body system with anisotropic dipolar interactions. Nevertheless, population losses caused by inelastic collisions have long been a challenge in ultracold molecule research. Here, we investigate the stability of $^{23}\text{Na}^{40}\text{K}$ ground state molecules in the presence of background ^{23}Na atoms. We start the experiment with 6×10^4 number of Feshbach molecules, and 8×10^5 number of ^{23}Na atoms. The first $20 \mu\text{s}$ -long STIRAP pulse transfers Feshbach molecules into ground state molecules, which subsequently are held together with background ^{23}Na atoms for fixed amount of time inside ODT. The second STIRAP pulse facilitates the transfer of the remaining ground state molecules back to Feshbach molecules for detection. Fig. 4-6 shows the population loss of ground state molecules, which is fitted by a exponential time decay curve $N = N_0 \exp^{-t/\tau}$, with an exponential time constant of $\tau = 5.8 \text{ ms}$. The inset shows the absorption image of ^{23}Na with a peak boson density of $n_B = 1.2 \times 10^{12} \text{ cm}^{-3}$. As ^{23}Na atoms are in majority limit, we observe no ^{23}Na counts change throughout the experiment. The population loss of ground state molecules is attributed to chemical reactions with surrounding bosons, which can be

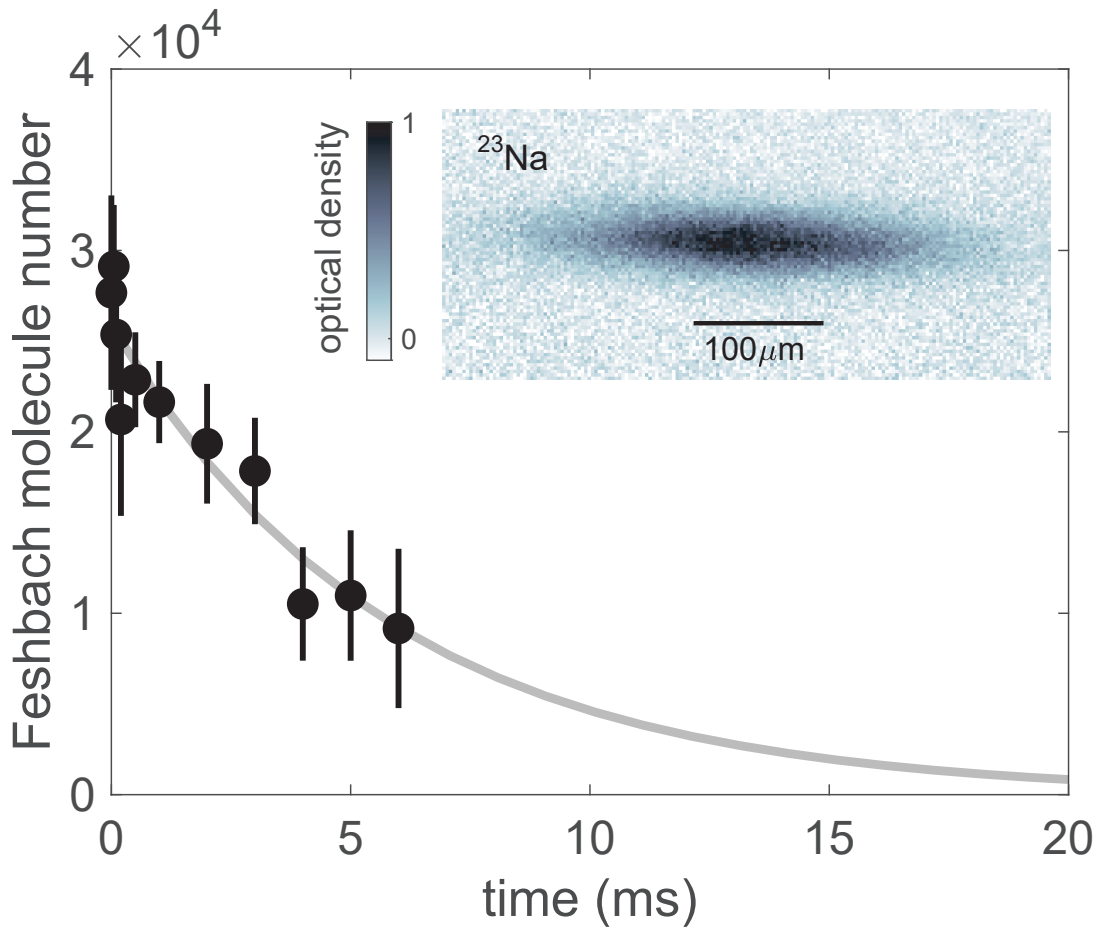


Figure 4-6: Ground state molecule lifetime in a dilute boson bath. After the first STIRAP pulse, we hold the ground state molecule for period of time to study their loss rate with the dilute boson bath at $T = 80 \mu\text{K}$. A second STIRAP pulse convert the remaining molecules back after the holding time so we can image the Feshbach molecules. The calibrate peak boson density $n_B = 1.2 \times 10^{12} \text{ cm}^{-3}$ and an exponential decay time constant of $\tau = 5.8 \text{ ms}$ yields the ground state molecule two body loss rate $\beta = 1.4 \times 10^{-10} \text{ cm}^3/\text{s}$ with the boson bath.

characterized by the rate equation:

$$\frac{dn_m(t)}{dt} = -\beta n_B n_m(t) = -\tau^{-1} n_m(t) \quad (4.3)$$

Based on the constant boson density, we can conclude that the two-body loss coefficient is given by $\beta = (n_B \tau)^{-1} = 1.4 \times 10^{-10} \text{ cm}^3/\text{s}$. We can model the chemical reaction between $^{23}\text{Na}^{40}\text{K}$ and ^{23}Na atoms as following:



As a result of ^{23}Na being a smaller atom than ^{40}K , the $^{23}\text{Na}_2$ molecule, with approximately $h \times 184$ THz binding energy [75, 79], is much tighter-bound than $^{23}\text{Na}^{40}\text{K}$, which has binding energy of $h \times 156$ THz [57]. The deep electronic potential of the $^{23}\text{Na}_2$ molecule provides many exothermic exit channels. Hence, in the reaction complex formed by a $^{23}\text{Na}^{40}\text{K}$ ground state molecule and a ^{23}Na atom, the preferred reaction products are the ^{40}K atom and the $^{23}\text{Na}_2$ molecule. The exothermic chemical reaction releases a significant amount of kinetic energy, which is carried away by the ^{40}K atom and the $^{23}\text{Na}_2$ molecule as they move apart. By the same principle, we can understand that the $^{40}\text{K}^{87}\text{Rb}$ molecule is chemically stable when immersed in a bosonic bath of ^{87}Rb atoms, but becomes chemically reactive when surrounded by a fermionic bath of ^{40}K atoms, as reported in previous studies [55]. The assessment of chemical stability in bi-alkali molecules based solely on atom size is crude, as other factors such as atom-molecule spin structure and quantum statistics can also play crucial roles in determining their stability, which is still under intense theoretical and experimental study. For instance, authors observe more intricate molecule-atom collisions that are influenced by Feshbach resonance among $^{23}\text{Na}^{40}\text{K}$ singlet ground molecules and ^{40}K atoms in [88], and $^{23}\text{Na}^7\text{Li}$ triplet ground state molecule and ^{23}Na in [71, 59]. In the upcoming section, we will introduce an effective technique that utilizes resonant laser fields to remove the residue atoms.

4.5 Atom removal

In this section, we present a method for effectively removing atoms by applying laser beams that are resonant with ^{23}Na and ^{40}K atoms. The removal light share the same source and optical path as light for atoms/Feshbach molecules imaging. We apply $4 \mu\text{W}$ of resonant light, which drives the $^{40}\text{K}|F = 9/2, mF = -9/2\rangle$ to $|F' = 11/2, mF = -11/2\rangle$ transition, to remove ^{40}K atoms with initial density of $n_F = 2 \times 10^{11} \text{ cm}^{-3}$. Fig. 4-7a shows that the removal of $^{40}\text{K}|9/2, -9/2\rangle$ atoms is achieved within $30 \mu\text{s}$. Due to $^{23}\text{Na} |F = 1, mF = 1\rangle$ to $|F' = 2, mF = 2\rangle$ is not a cycling transition, we utilize both $4 \mu\text{W}$ of ‘pump’ light and $16 \mu\text{W}$ of ‘repump’ light to remove $^{23}\text{Na} |1, 1\rangle$ atoms with an initial density of $n_B = 1 \times 10^{12} \text{ cm}^{-3}$. (‘Pump’ light drives the $^{23}\text{Na} |F = 2, mF = 2\rangle$ to $|F' = 3, mF = 3\rangle$ transition, and ‘repump’ light drives the $^{23}\text{Na} |F = 1, mF = 1\rangle$ to $|F' = 2, mF = 2\rangle$ transition.) Fig. 4-7b demonstrates that the removal of $^{23}\text{Na}|1, 1\rangle$ atoms is achieved within $10 \mu\text{s}$. The removal time scale for ^{23}Na atoms increases to 1 ms when a dense BEC of ^{23}Na is formed.

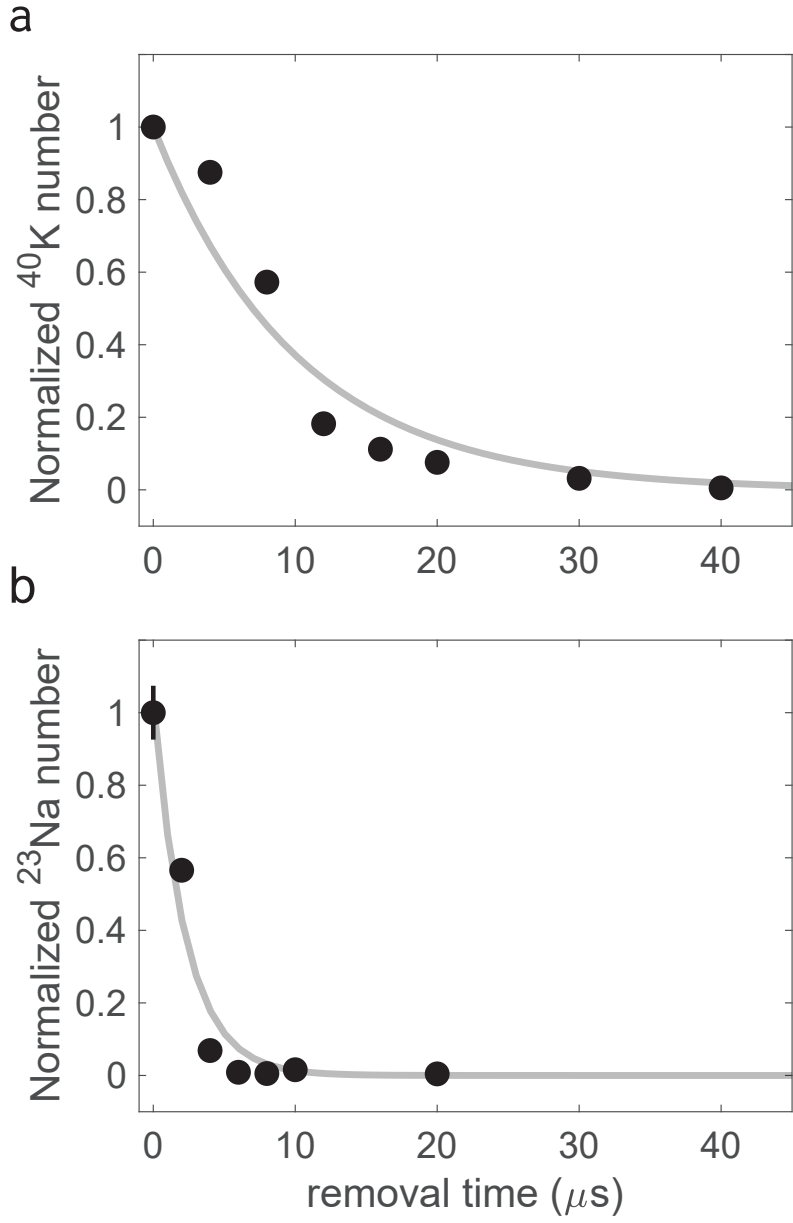


Figure 4-7: Demonstration of efficient ^{23}Na and ^{40}K atoms removal with resonant laser light. a. Population of ^{40}K atoms in relation to laser removal time. ^{40}K atoms are removed within 4 μW of laser light that drives a σ^- transition from $|F = 9/2, mF = -9/2\rangle$ to $|F' = 11/2, mF = -11/2\rangle$. The gray curve fits the exponential population decay with exponential time constant of $\tau_K = 10 \mu\text{s}$. b. Population of ^{23}Na atoms in relation to laser removal time. The ^{23}Na atoms are removed by pump and repump laser light, which resonantly drives $|F = 2, mF = 2\rangle$ to $|F' = 3, mF = 3\rangle$ and $|F = 1, mF = 1\rangle$ to $|F' = 2, mF = 2\rangle$ respectively. The gray line fits the Na removal with exponential time constant $\tau_{Na} = 2.3 \mu\text{s}$. Both removal lights are derived from absorption imaging light along the lab z (gravity) axis.

4.6 STIRAP efficiency

In this section, we experimentally characterize the STIRAP efficiency, which will provide valuable insights for future improvements in the creation of $^{23}\text{Na}^{40}\text{K}$ ground state molecules. A successful STIRAP transfer requires the state vector to adiabatically follow the dark state. The laser coupling rate and transfer time set the adiabatic criteria for STIRAP. The transfer time scale is constrained by the coherence time of the experiment, which is typically determined by the relative phase noises of the STIRAP lasers used. In our application, for transferring population from Feshbach molecules to the absolute ground state molecules, the dark state is dynamically controlled by two STIRAP lasers, as shown in Eqn. 4.2. Bright states contain admixture of intermediate excited state that is highly dissipative due to spontaneous emission. Therefore any population leakage to bright states due to non-adiabaticity can be detrimental for the transfer efficiency. On one hand, STIRAP is a robust protocol that is insensitive to many experimental parameters, such as laser pulse shape and timing. On the other hand, due to the robust nature of STIRAP, there is no simple formulation that can exactly model the STIRAP transfer process, taking into account all the experimental parameters [7]. We employ a model based on Bergmann [89] to approximate the efficiency of STIRAP in relation to the effective Rabi rate Ω and environment decoherence D .

$$\eta = \exp\left(-\frac{\pi^2 \gamma_e}{\Omega^2 \tau}\right) \exp(-D\tau). \quad (4.5)$$

The first part of this analytic formula, $\exp\left(-\frac{\pi^2 \gamma_e}{\Omega^2 \tau}\right)$, represents the adiabaticity criteria, which is determined by the effective Rabi rate Ω and the transfer process time τ , where γ_e denotes the excited state dissipation rate. The second part of the model, $\exp(-D\tau)$, accounts for the coherence effect on STIRAP transfer efficiency. Here, D represents total the environment decoherence, which can arise from various sources such as laser source phase fluctuations, phase scrambling from optical fibers, AOM rf driver noises, and ambient electromagnetic noises. The simple STIRAP model presented in Eqn. 4.5 exhibits excellent agreement with our experimental characterization. In

our experimental procedure, we initiate the transfer process of Feshbach molecules to ground state molecules using the first STIRAP pulse. The Feshbach molecules that are not successfully transferred to the ground state are subsequently removed using resonant light in $40 \mu\text{s}$. This atom removal ensures that only the ground state molecules are retained. The second STIRAP pulse subsequently transfers the ground state molecules back to Feshbach molecules for detection. Fig. 4-8 illustrates the STIRAP efficiency as a function of the STIRAP pulse duration τ . The optimal STIRAP pulse time is determined to be $20 \mu\text{s}$ in our experimental characterization. This time duration represents a ‘Goldilocks’ point that balances the requirements of adiabaticity and coherence time. A shorter STIRAP pulse duration would result in reduced adiabaticity, while a longer pulse duration would introduce more decoherence effects. Thus, the optimal pulse duration of $20 \mu\text{s}$ strikes a favorable balance between these competing factors, resulting in the highest transfer efficiency in our experimental setup. As shown in Fig. 4-8, the gray curve represents the fit result of Eqn. 4.5, which is obtained by multiplying the decoherence contribution (the orange dashed line) with the adiabatic criteria contribution (the blue dashed line). The fit results of the STIRAP model reveal a decoherence width of $D = (2\pi)3 \text{ kHz}$, which corresponds to a coherence time of $64 \mu\text{s}$. Our experimental findings reveal that the coherence time obtained from laser PDH lock noises is typically a generous estimate. This is because the estimation of coherence time based solely on laser lock noises does not take into account decoherence mechanisms that may occur outside of the laser lock servo. It is also worth noting that the dark state population time dynamics measurements shows a similar coherence time measurement which is demonstrated in Fig. 4-3. Shown in Fig. 4-8 as blue dashed line, adiabatic criteria part of the fit yields $\frac{\Omega^2}{\pi^2\gamma_e} = (2\pi) 170 \text{ kHz}$, which is in an excellent agreement with the STIRAP two-photon resonance spectrum width demonstrated in Fig. 4-5. The adiabatic criterion can also be interpreted as the energy gap between the avoided crossings during the adiabatic transfer process, which will be discussed in detail in Chapter 5.7.

In addition to investigating the effects of STIRAP pulse duration on efficiency, we also conducted a characterization of the impact of STIRAP laser power. Fig.

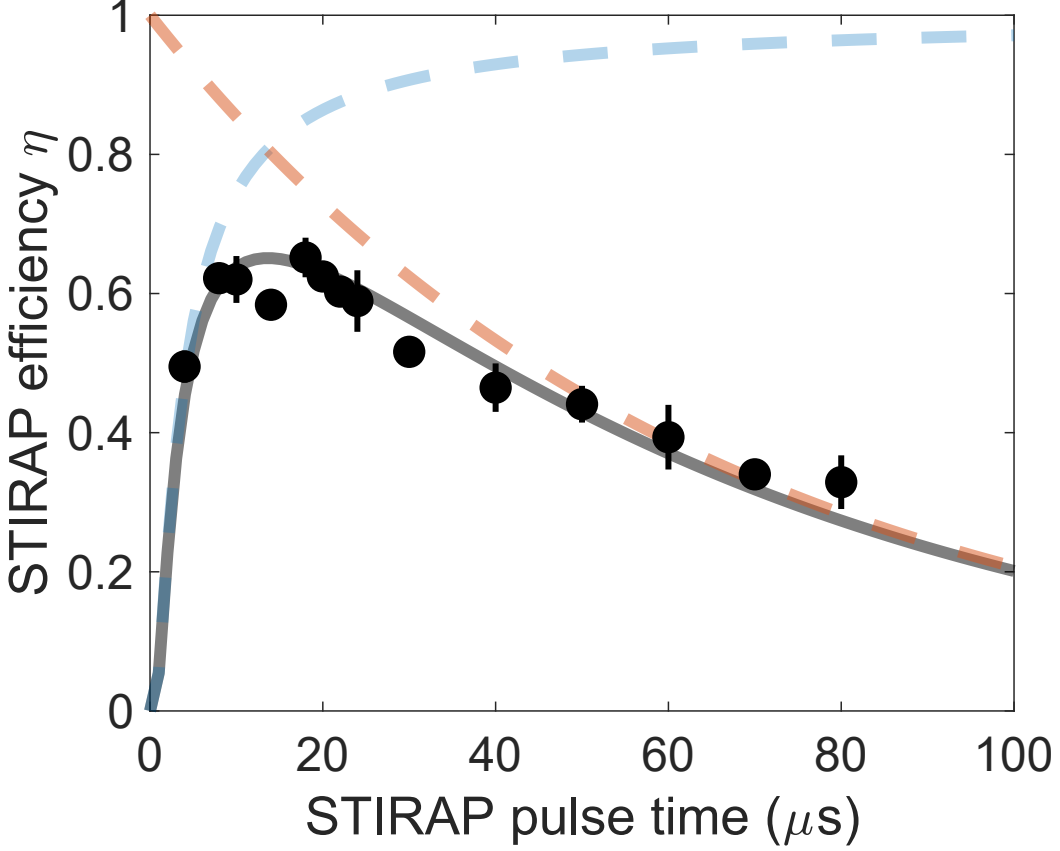


Figure 4-8: Observation of STIRAP efficiency as a function of pulse duration. We perform a round-trip STIRAP on the initial Feshbach molecules. The first STIRAP pulse transfers the Feshbach molecules into ground state molecules. Subsequently, we remove any residual atoms and Feshbach molecules, which ensures a background-free signal. The second STIRAP pulse transfers the ground state molecules back to Feshbach molecules for counting. The efficiency of single-trip STIRAP is calculated as $\sqrt{\frac{N_f}{N_i}}$, where N_i is the initial Feshbach molecule population, and N_f is the returning Feshbach population. The black dots represent the single-trip STIRAP efficiency in response to pulse time. The gray solid line shows the fit to the data based on Eqn. 4.5, which incorporates both adiabatic criteria and decoherence effects. The red dashed line represents $e^{-D\tau}$, which denotes the contribution of decoherence to the STIRAP transfer. The blue dashed line shows $e^{-\frac{\pi^2\gamma_e}{\Omega^2\tau}}$, which represents the contribution of the adiabatic criteria. The fitted value for laser coherence is $D = (2\pi)3 \text{ kHz}$, or equivalently a coherence time of $D^{-1} = 64 \mu\text{s}$, which is in an excellent agreement from dark state population decay shown in Fig. 4-3. The fitted value for effective Rabi rate $\Omega^2/(\pi^2\gamma_e) = (2\pi)170 \text{ kHz}$.

4-9 illustrates the STIRAP efficiency in relation to up-leg and down-leg laser powers, where the STIRAP is chosen to be $20 \mu\text{s}$. We keep the STIRAP pulse time fixed at $20 \mu\text{s}$. As shown in Fig. 4-9a, we vary the up-leg power while keeping the down-leg power at $75 \mu\text{W}$. Similarly, in Fig. 4-9b, we scan the down-leg power while maintaining the up-leg power at 1.2 W . Following the first STIRAP pulse, any remaining residue atoms are removed to ensure that only ground state molecules are transferred back to Feshbach molecules during the second STIRAP pulse. The STIRAP efficiency can be easily saturated by less than $50 \mu\text{W}$ of down-leg laser power, as the result of strong Frank-Condon overlap between excited and ground state [56]. In contrast, the up-leg transition requires $> 1\text{W}$ of optical power to saturate. The coupling of the up-leg transition can be enhanced by using deeper-bound Feshbach molecules as the initial state, as recently demonstrated in a recent study [5]. In their work, they created close channel dominated Feshbach molecules with a binding energy of approximately 1 MHz , which resulted in more efficient coupling to the excited state and higher transfer efficiency in the STIRAP process. However, a Rabi rate that is too large can lead to complications in STIRAP transfer due to the participation of other hyperfine states in the ground state manifold. For instance, authors in [50] observed interference effects among ground state hyperfine states. Therefore, there exists an upper limit on the Rabi rate, which is set by spacing between nearby discrete state energy.

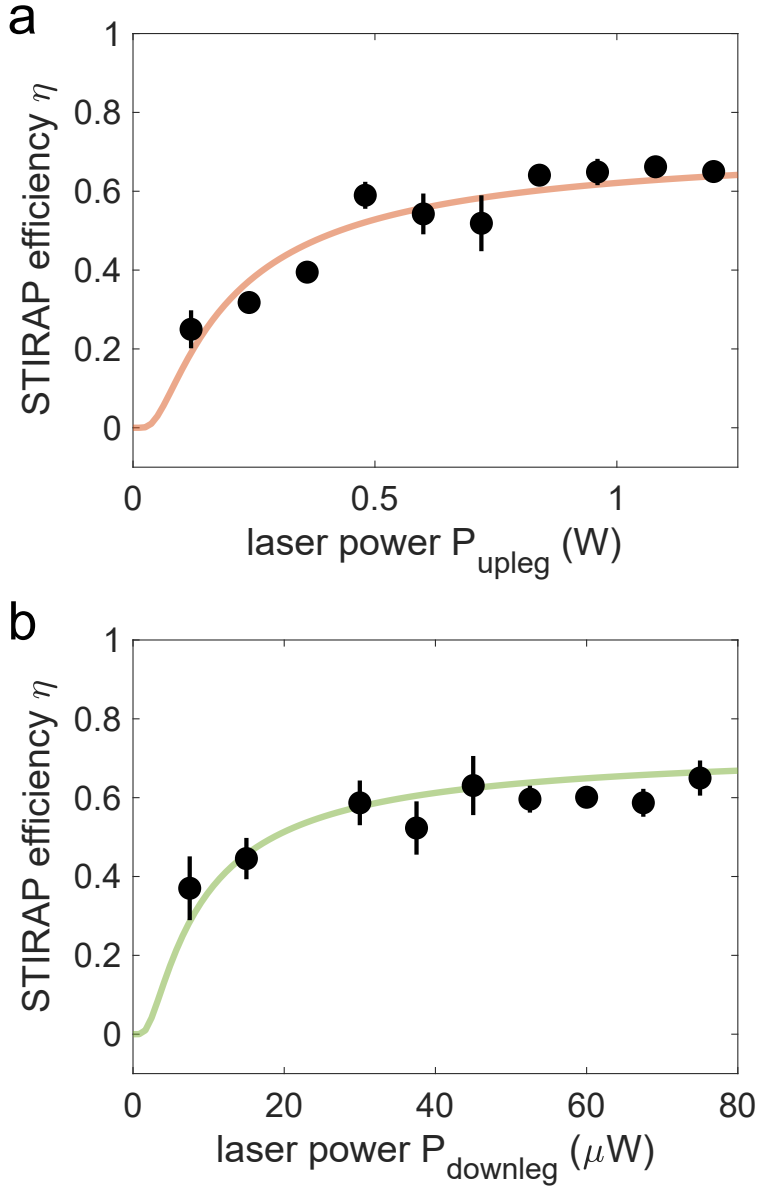


Figure 4-9: Observation of STIRAP transfer efficiency as a function of laser powers. We conduct the round-trip STIRAP on initial Feshbach molecules. To produce background-free signal, residue atoms and Feshbach molecules are removed after the first STIRAP pulses. a. STIRAP single-trip efficiency vs up-leg laser power. As we vary the up-leg laser power, the down-leg laser power is fixed at $75 \mu\text{W}$. b. STIRAP single-trip efficiency vs down-leg laser power. While we scan the down-leg laser power, the up-leg laser power is maintained at 1.2 W .

Chapter 5

A new pathway to the dipolar molecule ground state from Bose polarons

Quantum gases of ultracold dipolar molecules are prime candidates for realizing novel many-body systems. Dipolar molecules possess large electric dipole moments and rich internal structures like vibrational, rotational, and nuclear spin degrees of freedom. The long-range nature of electric dipole moments between molecules can create new types of order that are beyond simple contact interactions between atoms. When a dipolar molecule is immersed inside of a Bose-Einstein condensate (BEC), molecule's rotational degree of freedom can couple to the bosonic bath and forms a new quasi-particle called an ‘angulon’ [68, 69, 47]. Realizing the angulon in ultracold temperature regime ($T < 1\text{mK}$) is still in its experimental infancy. Prior to this thesis work, experiments on realizing angulon were conducted at ‘cold’ temperature regime (1 mK to 1 K), where molecules are trapped inside helium droplets. Even at the cold temperature regime, the molecule rotational spectra are drastically modified due to the helium droplet dressing [48]. Rich internal structures of molecules impose challenges on direct laser cooling, which can be circumvented by choosing right categories of molecules with complicated laser manipulation. But direct laser cooling on molecule is much more challenging than laser cooling on alkali atoms, which have strong op-

tical cycling transitions. Endeavors in atom/molecule/optics research have advanced dipolar molecules in high phase space density to ultracold regime with temperature <1 mK in the last decade [15, 10]. The very strategy that brings molecules to ultracold temperature regime is leveraging powerful atomic cooling technique as much as possible, and only at the very end atom pairs are coherently transferred into ground molecular state. Weakly-bound molecules associated via Feshbach resonances are considered a prerequisite step in creation of ground state molecules, because Feshbach molecules provide strong coupling to the excited state. Chapter 4 follows the footsteps of creating ground state dipolar molecules from Feshbach molecules. However, the Feshbach molecule association process yields a finite efficiency and Feshbach molecules are short-lived in a dense bosonic bath due to rapid three-body recombinations, which from the very beginning poses an obstacle for creating ground state molecules inside a BEC. Work in this chapter experimentally realizes a new pathway to the dipolar molecule ground state, which never involves a weakly-bound molecular state as a starting point. The new pathway begins with an attractively interacting Bose-Fermi mixture, directly followed by a two-photon rapid adiabatic passage (STI-RAP) that coherently transfers the mixture into the absolute rovibrational ground state.

5.1 Contact is all you need

With fermions at the impurity limit, the Bose-Fermi mixture can be described by a framework of Bose polarons. Bose polarons are quasi-particles formed by impurities dressed by a bosonic bath. Within variational descriptions, the Bose polaron wavefunction has a localized component that has the same characteristics as a Feshbach molecule whose molecule size is set by the polaron energy [64, 49, 87]. Polaron energy is related to contact, a many-body quantity that characterizes short-range correlations and captures the change of polaron energy with interaction strength. An intuitive interpretation of the contact is the probability that a fermion finds a boson at a certain proximity [76], which is the very essence for binding two atoms into a molecule.

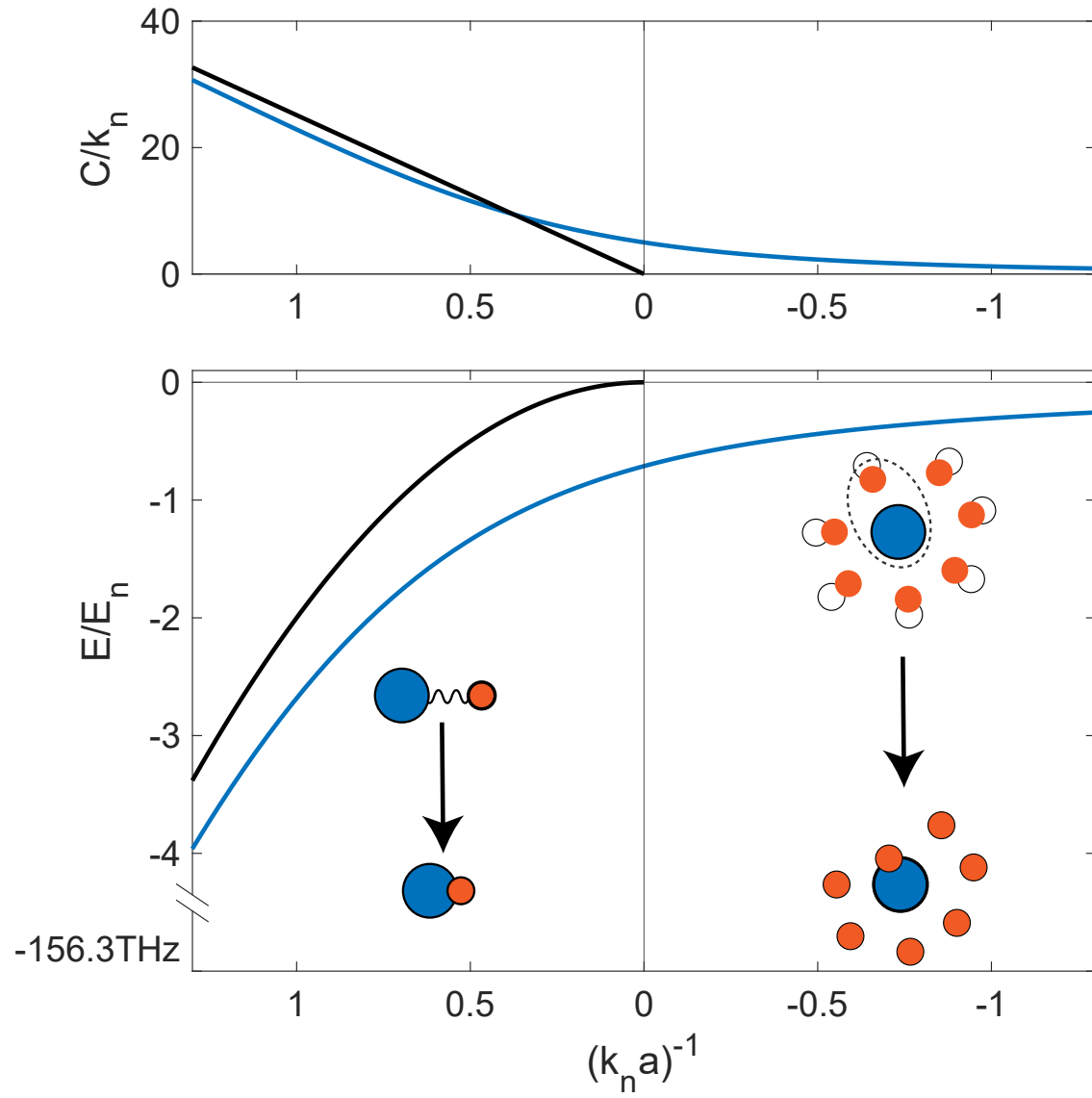


Figure 5-1: Pathways to the absolute rovibrational ground state molecules. Polaron contact and energy based on variational descriptions are illustrated in blue line together with Feshbach molecule in black line. The Feshbach molecule branch starts near the Feshbach resonance and extends to the repulsive side. A polaron can be pictured as a Feshbach molecule dressed by a condensate, whose energy smoothly evolves from negative to positive interaction strength and eventually connects to the molecule branch. A polaron, with near unitarity-limited interaction, has a sizable contact that enables couplings to the excited state and a 50 times longer lifetime in a boson bath than a Feshbach molecule. A typical pathway to the ground state molecule from a Feshbach molecule is illustrated on the left. On the right, a new pathway is demonstrated starting from a fermion (blue circle) dressed by bosons (orange circles) to a 156.3 THz deeply bond ground state molecule.

Fig. 5-1 shows the polaron (blue) energy and contact smoothly evolving from attractive to repulsive interactions, where polarons merge with Feshbach molecules (black). Feshbach molecules exist only at the repulsive side of the resonance, where they are short-lived in the presence of a dense boson bath. In contrast, polarons with attractive interactions have a finite contact and almost two orders of magnitude slower loss rate with bosons, even near unitarity. These two properties of the polaron open up a unique gateway to make ground state molecules in the presence of a BEC.

Similar to our previous work described in [87], we start with fermionic ^{40}K and bosonic ^{23}Na at their ground hyperfine states: $^{40}\text{K}|F, m_F\rangle = |\frac{9}{2}, -\frac{9}{2}\rangle$ $^{23}\text{Na}|F, m_F\rangle = |1, 1\rangle$. After the evaporative cooling in a crossed optical dipole trap, ^{23}Na atoms form a BEC with peak density $n_B = 7 \times 10^{13} \text{ cm}^{-3}$, temperature $T=100 \text{ nK}$ and trapping frequencies $(\omega_x, \omega_y, \omega_z)/2\pi = (120, 116, 10) \text{ Hz}$. A magnetic field gradient is applied to levitate both species, which cancels the gravitational sag due to ^{23}Na ^{40}K mass difference. Fermions are fully immersed in the BEC at 81 G where three-body losses between ^{23}Na ^{40}K are minimal. Fermions are at the impurity limit with peak density $n_F = 2 \times 10^{11} \text{ cm}^{-3}$. The magnetic field is then ramped to its final value at 78.54 G, where the inter-species scattering length $a = -4000 a_{\text{Bohr}}$. Impurities are strongly attracted to the BEC with interaction strength $(k_n a)^{-1} = -0.3$, where $k_n = (6\pi^2 n_B)^{1/3}$ is the inter-boson distance. Following a 2 ms thermalization time, impurities are strongly dressed by the BEC and form Bose polaron quasi-particles with an estimated energy $E_p/E_n = -0.5$. E_p is the quasi-particle self-energy and $E_n = \frac{\hbar^2 k_n^2}{4m_r}$ is the boson degeneracy energy ($m_r = \frac{m_B m_F}{m_B + m_F}$ is the reduced mass). Fig. 5-1 demonstrates that Bose polarons with attractive interactions have a finite contact. We observe that the contact enhances the impurity coupling to the excited state with photoassociation spectroscopy.

5.2 Single photon dynamics

An up-leg laser (ω_1) in horizontal polarization is applied to perform the photoassociation (PA) spectroscopy shown in Fig. 5-2. When ω_1 resonates with the initial polaron

state $|P\rangle$ and the excited state $|E\rangle$, the quasi-particle wavefunction collapses as each dressed impurity finds a nearby boson and photoassociates to an electronically excited molecule. We observe free-particle continuum influence which is perceived a photoassociation resonance frequency red-shift that is linear to the up-leg laser intensity. Due to the polaron's small energy separation from the free-particle continuum, the continuum dresses the excited state and shifts its energy. Similar AC-Stark-like effects were studied in [9, 63, 60, 43, 82]. The continuum- and light-induced spectral shift is measured to be $-(2\pi)2.9 \text{ kHz}/(\text{W cm}^{-2})$. The maximum polaron to excited state coupling is achieved with up-leg laser intensity at $7 \times 10^3 \text{ W/cm}^2$ and at frequency $-(2\pi)19 \text{ MHz}$ from the unperturbed resonance. As shown in Fig. 5-3, strongly dressed impurities within the BEC Thomas-Fermi radius (black dots) are averaged to have a $\Omega_1 = (2\pi)0.6 \text{ MHz}$ Rabi rate with a $5 \mu\text{s}$ exponential decay constant. The impurities at the trap center are estimated to have a higher than average Rabi rate since they are dressed by denser bosons. In contrast, weakly dressed impurities outside of the Thomas-Fermi radius (gray dots) are unperturbed by the up-leg laser. These two distinctive photoassociation rates manifest the paramount importance of the contact in binding two atoms into a molecule.

5.3 Dark resonance spectroscopy of polaron

We perform dark resonance spectroscopy to characterize the initial polaron state coupling to the ground state via the electronically excited state. A down-leg laser (ω_2) in vertical polarization with $30 \mu\text{W}$ power is introduced as a pumping light with a fixed frequency that resonates with the ground state $|G\rangle$ and the excited state $|E\rangle$. Scanning the frequency of the up-leg laser (ω_1) changes the two-photon resonance condition ($\delta_{2\text{photon}}$). When two-photon resonance conditions are dissatisfied, shadows of the BEC are imprinted onto the impurities shown in Fig. 5-2 $\delta_{2\text{photon}}/2\pi = -2.7$ and 0.9 MHz . These ‘negative’ BEC prints on the impurities are results of the strongly dressed impurities photo-associating into excited molecules. In the narrow window where two-photon resonance conditions are satisfied ($|\delta_{2\text{photon}}/2\pi| < 200 \text{ kHz}$), the initial polaron

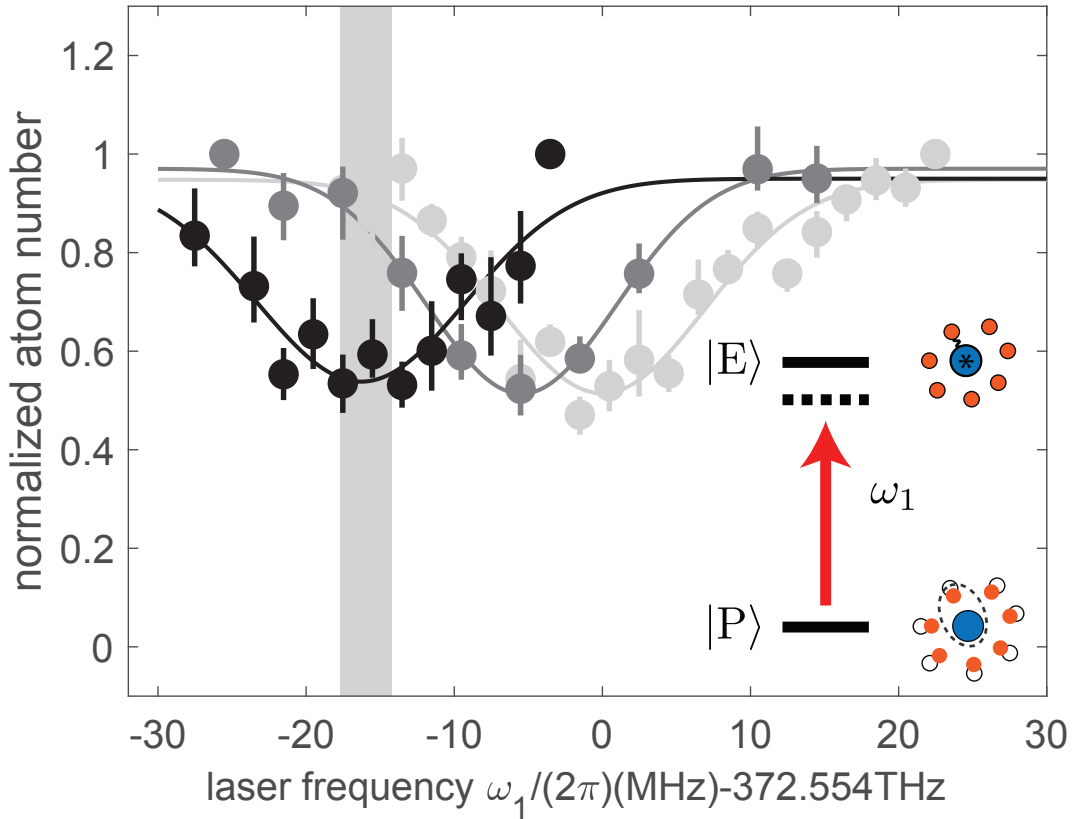


Figure 5-2: Polaron photoassociation spectral red-shift. The up-leg laser is frequency locked to the ULE cavity for improved frequency stability. A offset AOM shifts the laser frequency before the ULE cavity, which controls the up-laser frequency. Photoassociation spectrum with 3 up-leg power, 0.2, 0.6 and 1 W, is shown in lighter gray, gray and black. The photoassociation time is chosen to resolve the red-shift by promoting roughly half of the fermionic impurities that are within the BEC Thomas-Fermi radius. The photoassociation resonance frequency is measured to have a red-shift linear to up-leg laser intensity due to the nearby free-particle continuum, which is discussed in detail in Chapter ???. The gray shade marks up-leg frequency where the maximum polaron to excited state coupling is achieved. The up-leg resonates with the transition 3 (highlighted in Fig. 3-5) which is within the ‘balanced’ manifold with admixture of 64% $c^3\Sigma^+$ 36% $B^1\Pi$ electronically excited state potentials. The up-leg laser has horizontal polarization that selectively drives $\Delta m_F \pm 1$ transitions.

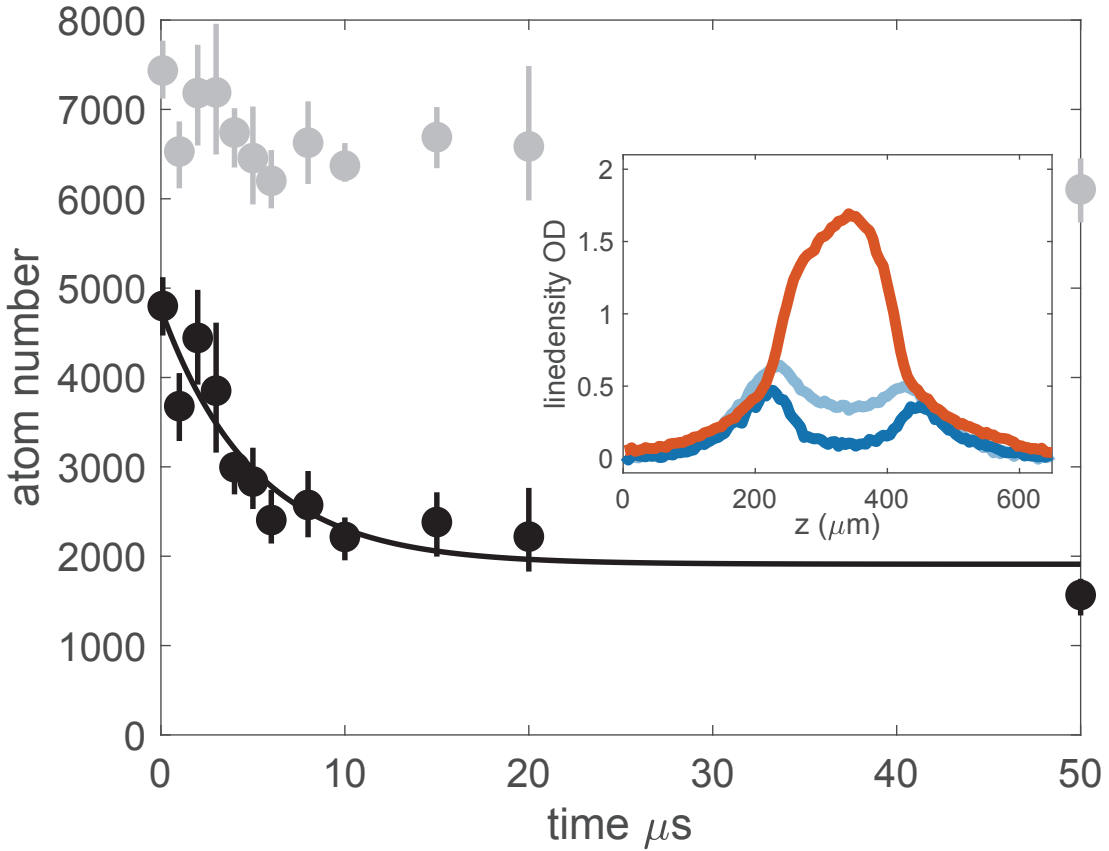


Figure 5-3: Polaron photoassociation time dynamics. Locally resolved impurities are measured with 1W up-leg laser power at with $-(2\pi)19\text{MHz}$ detuned frequency to achieve maximum photoassociative formation rate. As a result of strong dressing, impurities inside of the BEC Thomas-Fermi radius (black dots) are driven into the excited state with $5\ \mu\text{s}$ exponential time constant. Impurities outside of the BEC Thomas-Fermi radius (gray dots) show little coupling. Inset shows the integrated linedensity of the bosonic majority (orange) and fermionic impurities (light blue at $0\ \mu\text{s}$ and dark blue at $50\ \mu\text{s}$). The boson linedensity displays a BEC bimodal distribution and stays unperturbed during PA.

state, the dark state of the system, are transparent to the up-leg and down-leg lasers. The dark resonance spectrum in Fig. 5-4b precisely determines the ground state molecule binding energy by the up-leg and the down-leg laser frequency differences. The up-leg and the down-leg Rabi rates are fitted to be $\Omega_1, \Omega_2/(2\pi) = 0.4, 3.2$ MHz based on an open three-level model. These results from the dark resonance spectrum pave a clear path to the dipolar molecule ground state.

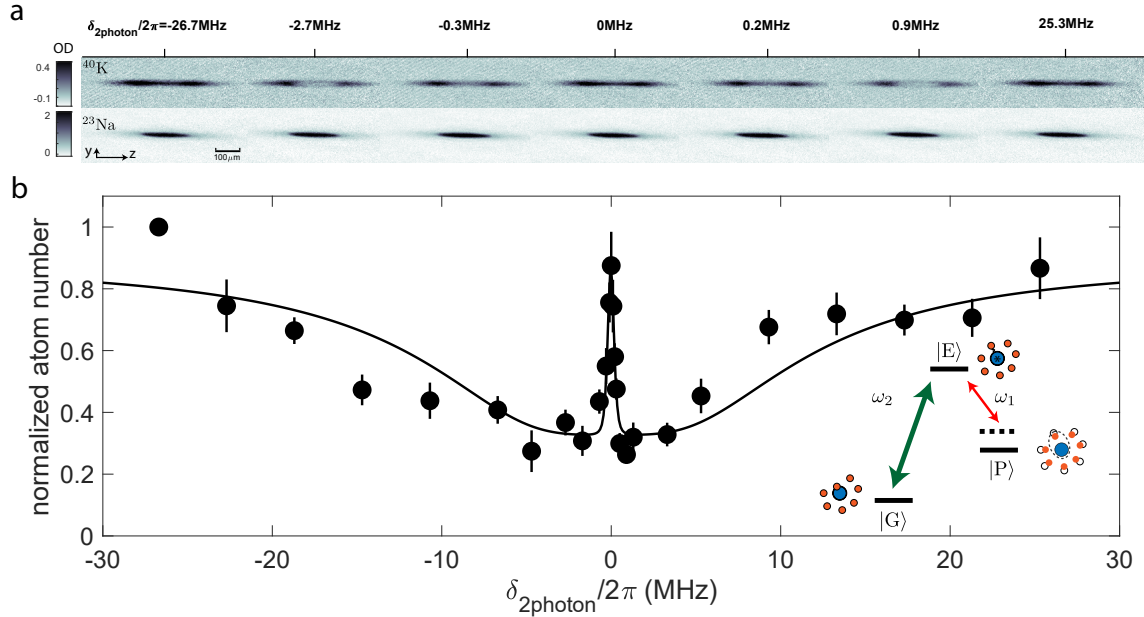


Figure 5-4: Observation of polaron coupling to the absolute ground state via dark resonance spectroscopy. a. Exemplary absorption images of the fermionic ^{40}K and the bosonic ^{23}Na . At $\delta_{2\text{photon}}/2\pi = -2.7, 0.9$ MHz, the BEC casts two shadows onto the fermions, manifesting fermions strongly dressed by the BEC are favored to couple to the excited state. b. Dark resonance spectrum with normalized counts of impurities within the BEC Thomas-Fermi radius. The inset illustrates the initial polaron state $|P\rangle$, the excited state $|E\rangle$ and the absolute molecular ground state $|G\rangle$ connected through the up-leg ω_1 in horizontal polarization with 200 mW power and down-leg laser ω_2 in vertical polarization with 30 μW . Up-leg (Ω_1) and down-leg (Ω_2) Rabi rates are fitted to be $\Omega_1, \Omega_2/2\pi = 0.4, 3.2$ MHz.

5.3.1 Dark resonance spectrum of three transitions

We perform two additional dark resonance spectrum via the triplet rich (92% $c^3\Sigma^+$ 8% $B^1\Pi$) and singlet rich (8% $c^3\Sigma^+$ 92% $B^1\Pi$) excited states in Fig. 5-5 and Fig. 5-6

respectively. Dark resonance spectroscopy is a powerful spectroscopic tool to measure the dipolar molecule ground state energy to sub-kHz precision from the narrow electromagnetic induced transparency (EIT) window. Stronger down-leg dressing power (higher down-leg Rabi coupling Ω_2) widens the EIT protection window. A fit model based on a numerical solver of three level system time propagator interprets the data and extract the down-leg Rabi rate Ω_2 . We use the same mixture condition described in the Section 5.3 to perform the dark resonance spectroscopy.

Fig. 5-7 summarizes the down-leg coupling strength in relation to down-leg optical power. Three excited state characters have down-leg Rabi rate. The absolute molecule ground state $|G\rangle$ is in pure singlet potential, therefore the singlet rich excited has the highest Franck-Condon overlap. Fig. 5-8 demonstrates the relative up-leg (Ω_1) and down-leg (Ω_2) coupling rates among three excited states. Ground state molecule creation from the initial polaron state via STIRAP. Ground state molecule creation from triplet rich initial state $|P\rangle$ relies on the electronically excited state $|E\rangle$ singlet-triplet mixing. The singlet-triplet potential mixing in the electronically excited state is the bridge that enables coherent creation of absolute ground state molecules from the initial polaron state. More prominent triplet character in the excited state provides strong up-leg coupling but weakens down-leg coupling.

5.4 Coherent creation of ground state dipolar molecules inside a BEC

We achieve dipolar molecule creation directly starting from polarons via a two-photon STIRAP. In the STIRAP sequence, the down-leg (Ω_2) and the up-leg (Ω_1) laser intensities (Ω_1^2, Ω_2^2) are ramped sinusoidally, and the dark state ($\approx \Omega_2 |P\rangle + \Omega_1 |G\rangle$) is adiabatically tilted from the polaron state $|P\rangle$ to the ground state $|G\rangle$. Fig. 5-10b demonstrates that the strongly dressed impurities (black dots) are coherently transferred into the absolute rovibrational ground state via a $30\ \mu\text{s}$ STIRAP, and consequently back to polarons after a reverse STIRAP. Such a coherent impurity

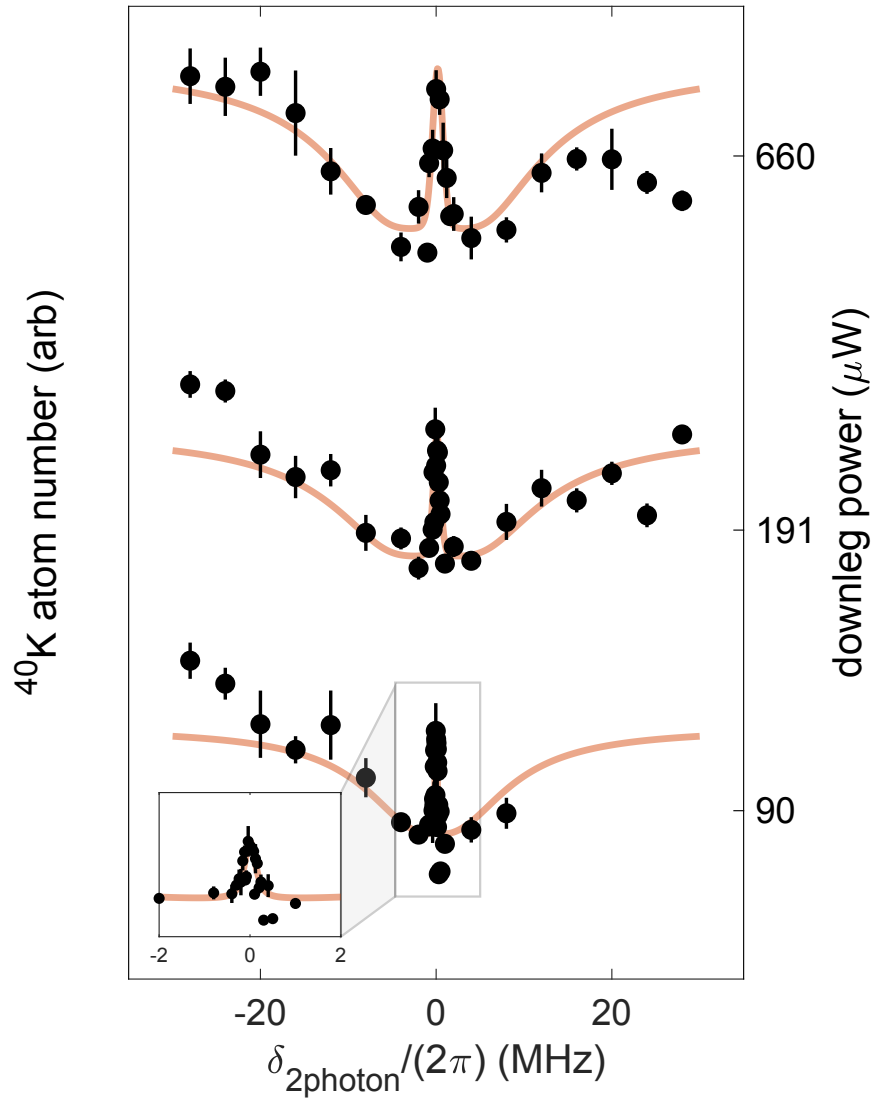


Figure 5-5: Dark resonance spectroscopy of the triplet rich manifold. Normalized ^{40}K counts revives inside of the EIT window due to interference between down-leg and up-leg laser. Normalized polaron counts are plotted on the left Y-axis at 3 down-leg dressing power. Normalized polaron counts are fitted with a three-level system solver by numerically expanding the Hamiltonian time propagator. The EIT window narrows down at low down-leg dressing power. Inset at the bottom zooms into the polaron counts within 4 kHz EIT window.

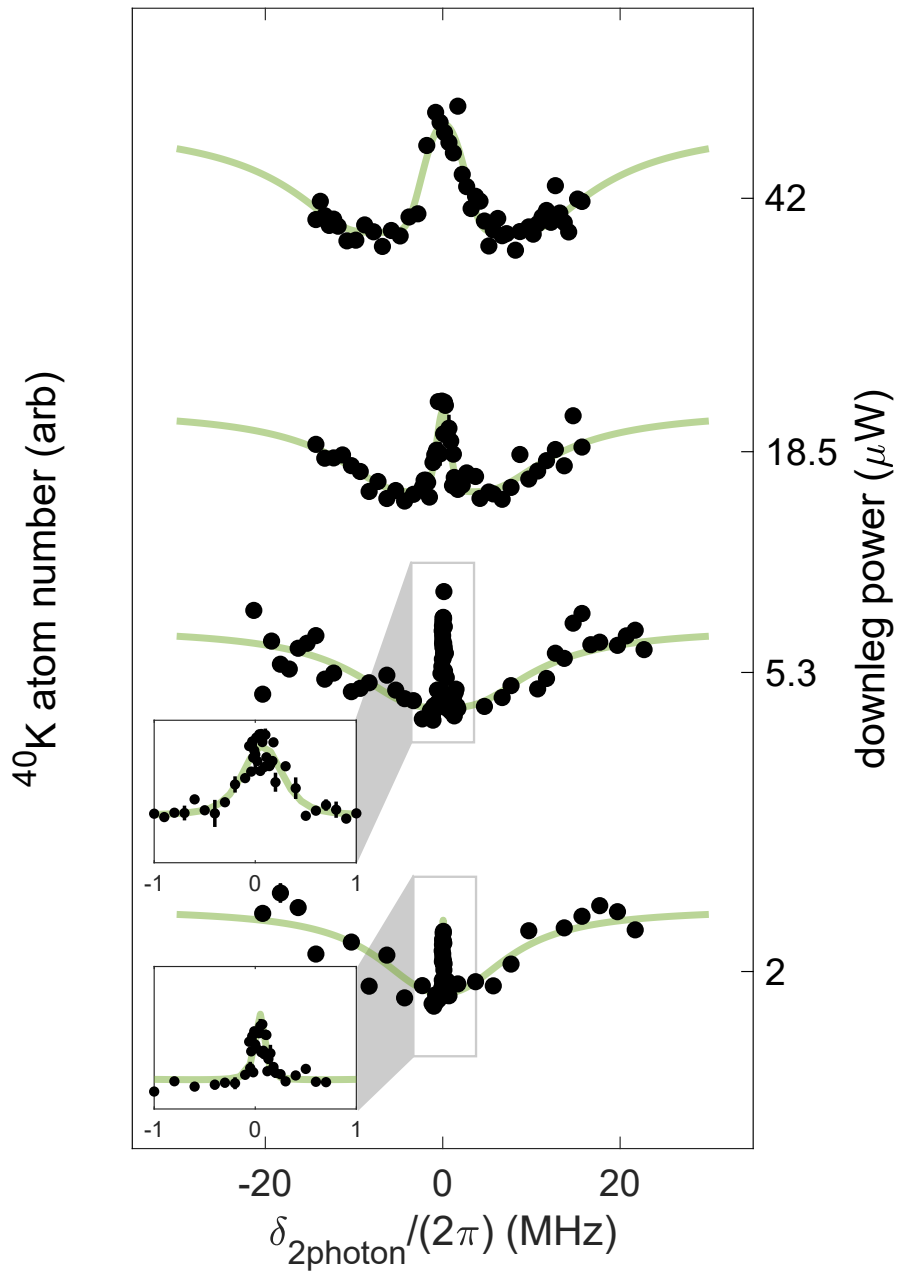


Figure 5-6: Dark resonance spectroscopy of the singlet rich manifold. Same plotting style as Fig. 5-5. EIT windows are much wider via the singlet rich excited state than that of triplet rich excited state, as a result of the large Franch-Condon overlap of pure singlet ground state. Two insets demonstrate narrow features within the EIT window with $5.3 \mu\text{W}$, minuscule down-leg dressing power.

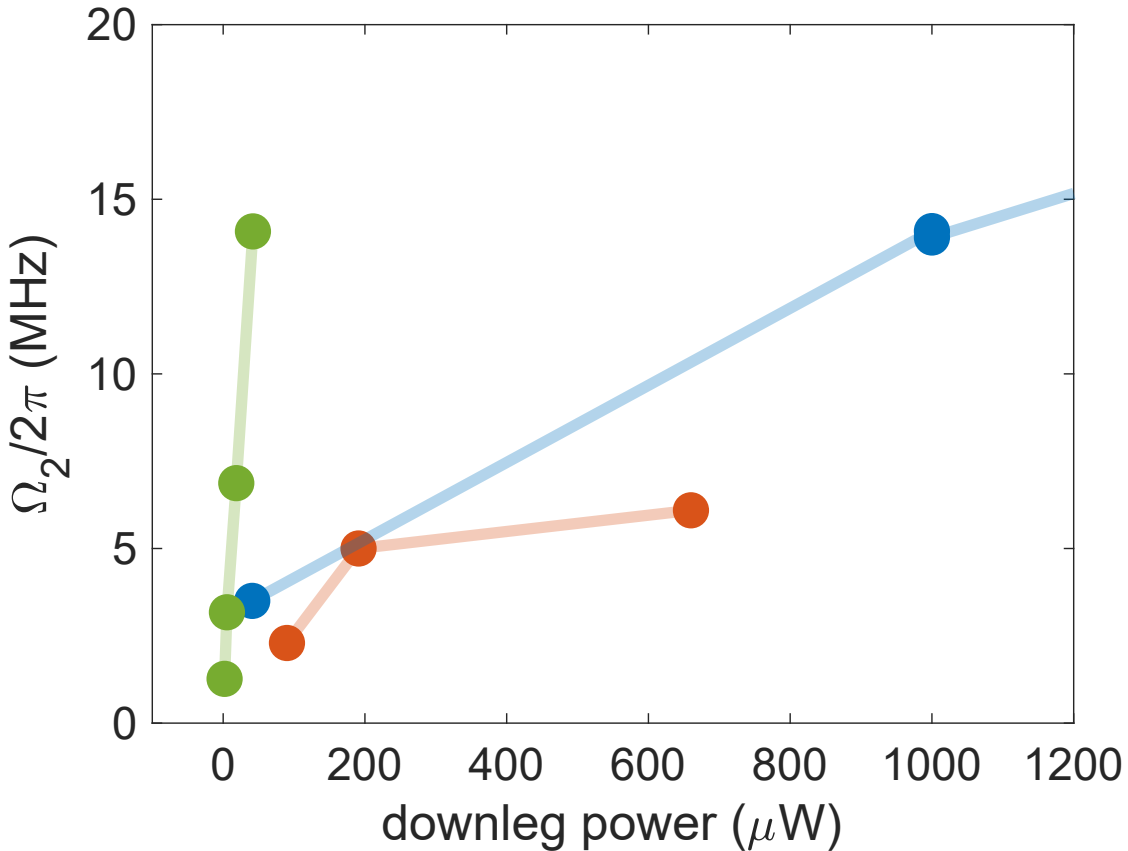


Figure 5-7: Down-leg coupling strength relation to optical power. Dark resonance spectroscopy fit results are shown in red (via triplet rich in Fig. 5-5), blue (via balanced excited state in Fig. 4-2), and green (via singlet rich excited state in Fig. 5-6). Down-leg Rabi Ω_2 of singlet rich excited state has the steepest slope to down-leg optical power.

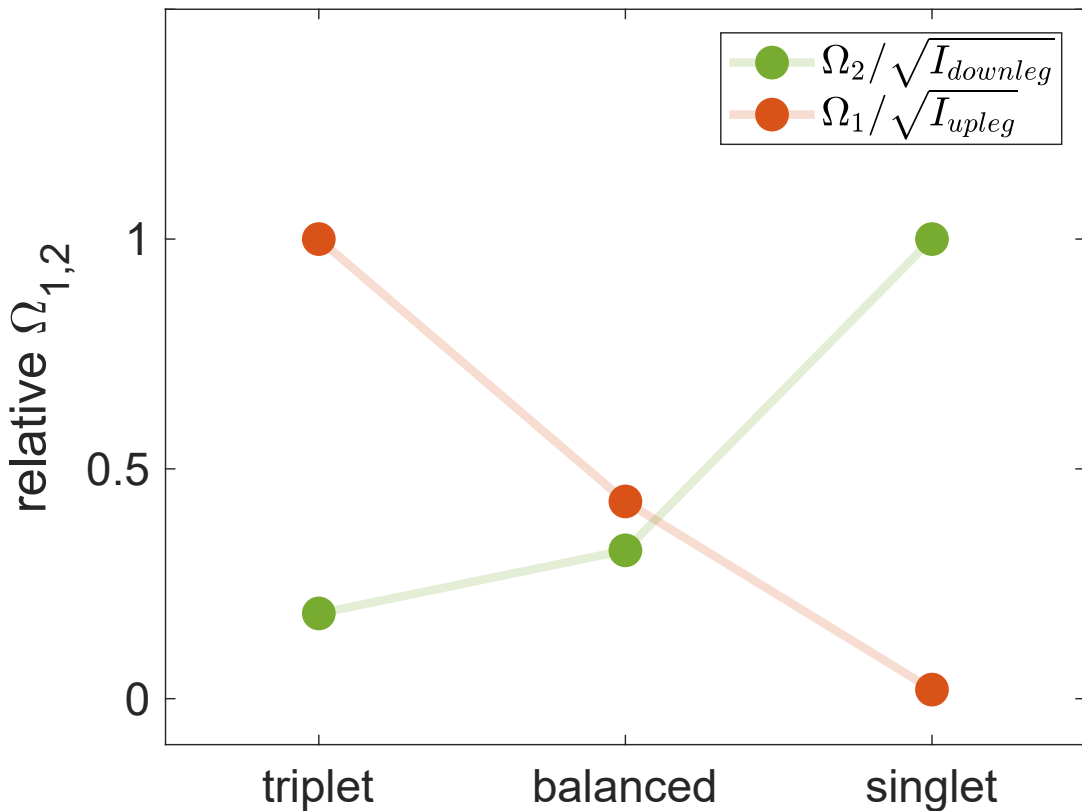


Figure 5-8: Relative up-leg and down-leg coupling strength via 3 excited states. Red: up-leg coupling strength; green: down-leg coupling strength. The up-leg coupling strength is normalized to the triplet rich excited transition which is extracted from Fig. 3-6; the down-leg coupling strength is normalized to the singlet rich excited state transition, which is extracted from Fig. 5-7.

signal revival is locally resolved and seen only with the impurities within the BEC Thomas-Fermi radius. In contrast, the impurities outside of the BEC Thomas-Fermi radius (gray dots in Fig. 5-10) do not participate in the STIRAP due to the lack of up-leg coupling. The STIRAP signal difference between strongly and weakly dressed impurities again reveals that the contact is the critical parameter for making dipolar molecules. We report on average 30% single STIRAP molecule conversion efficiency for the impurities strongly dressed by the BEC. The impurities that locate at the peak boson density are estimated to have a higher than average STIRAP efficiency. We realize 600 fermionic $^{23}\text{Na}^{40}\text{K}$ ground state molecules inside of the BEC, which is an inheritance from the initial polaron state. Since bosons are in the majority limit, the BEC is little perturbed by the STIRAP association, which remains at its initial temperature $T/T_c=0.1$ and peak density $n_B = 7 \times 10^{13} \text{ cm}^{-3}$.

5.5 Dipolar ground state molecule lifetime inside of a BEC

We measure the ground state $^{23}\text{Na}^{40}\text{K}$ molecule inside a BEC bath, using the same technique that measures the ground state molecule lifetime with a thermal boson bath in Chapter ???. After the first STIRAP pulse, the dressed impurities that find their boson partners are converted into the ground state molecules. We hold the ground state molecule in a fix period time before the second STIRAP pulse that transfer ground state molecules back to atoms for imaging. Fig. 5-11 shows the time dynamics of the ground state molecules that are immersed inside of the BEC. We measure two types of time dynamics shown in the Fig. 5-11 inset: the fast time dynamics is the ground state molecule inelastic collision with the BEC bath, and the slow time dynamics is the background polaron lifetime inside of the BEC.

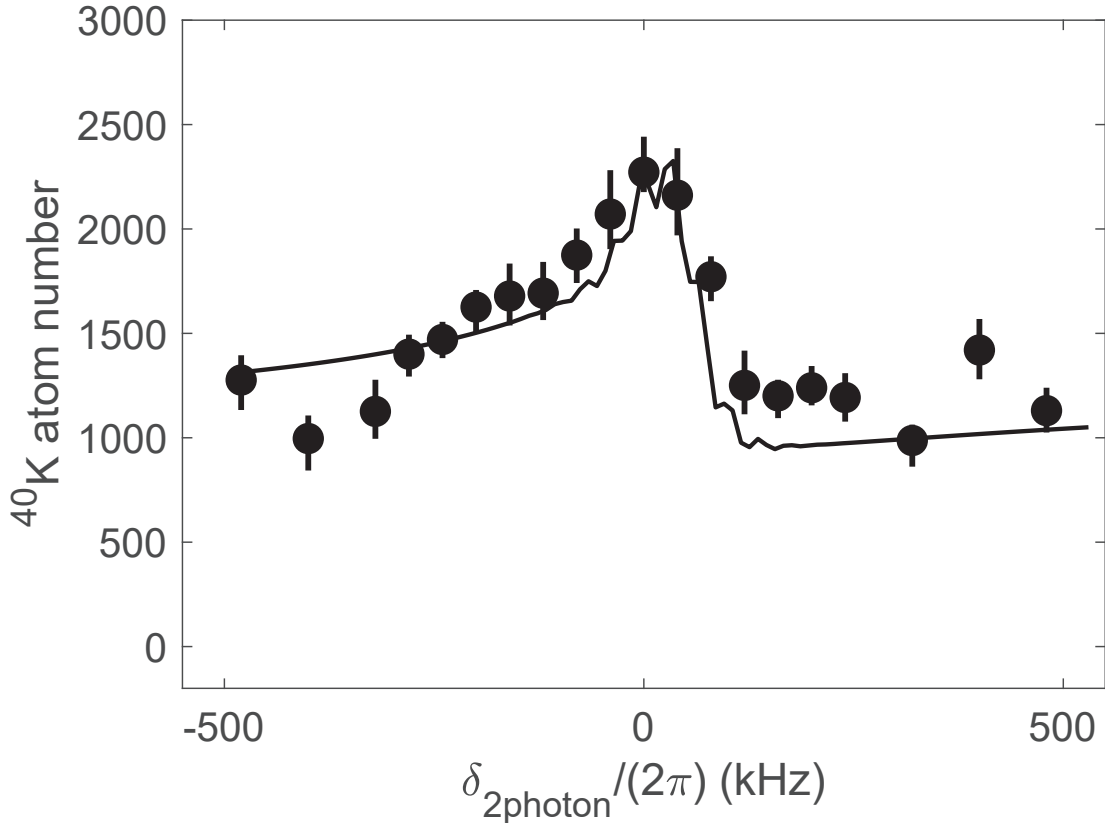


Figure 5-9: STIRAP two-photon resonance spectrum. Strongly dressed impurities that go through two consecutive STIRAP pulses are measured. The asymmetric STIRAP resonance lineshape is due to the nearby free-particle continuum, which is discussed in detail in Chapter ???. The spectrum peak center around the same two-photon resonance frequency as the dark resonance spectrum shown in Fig. 5-4. The maximum ^{40}K atoms are retrieved when two-photo resonance condition is satisfied, as the system remains in the dark state. Unable to satisfy the two-photon resonance condition exposes the system to bright states which are highly dissipative because bright states have electronically excited state component that rapidly decays to lower molecular states.

5.6 Outlook

In conclusion, our method utilizes the contact of a many-body initial state to create ground state molecules immersed in a BEC bath. Feshbach molecules have a finite association efficiency, which is worth mentioning when compared with the polaron pathway. Our locally resolved 30% polaron-to-ground state molecule transfer is not inferior to the Feshbach molecule approach, when both weakly-bound molecule as-

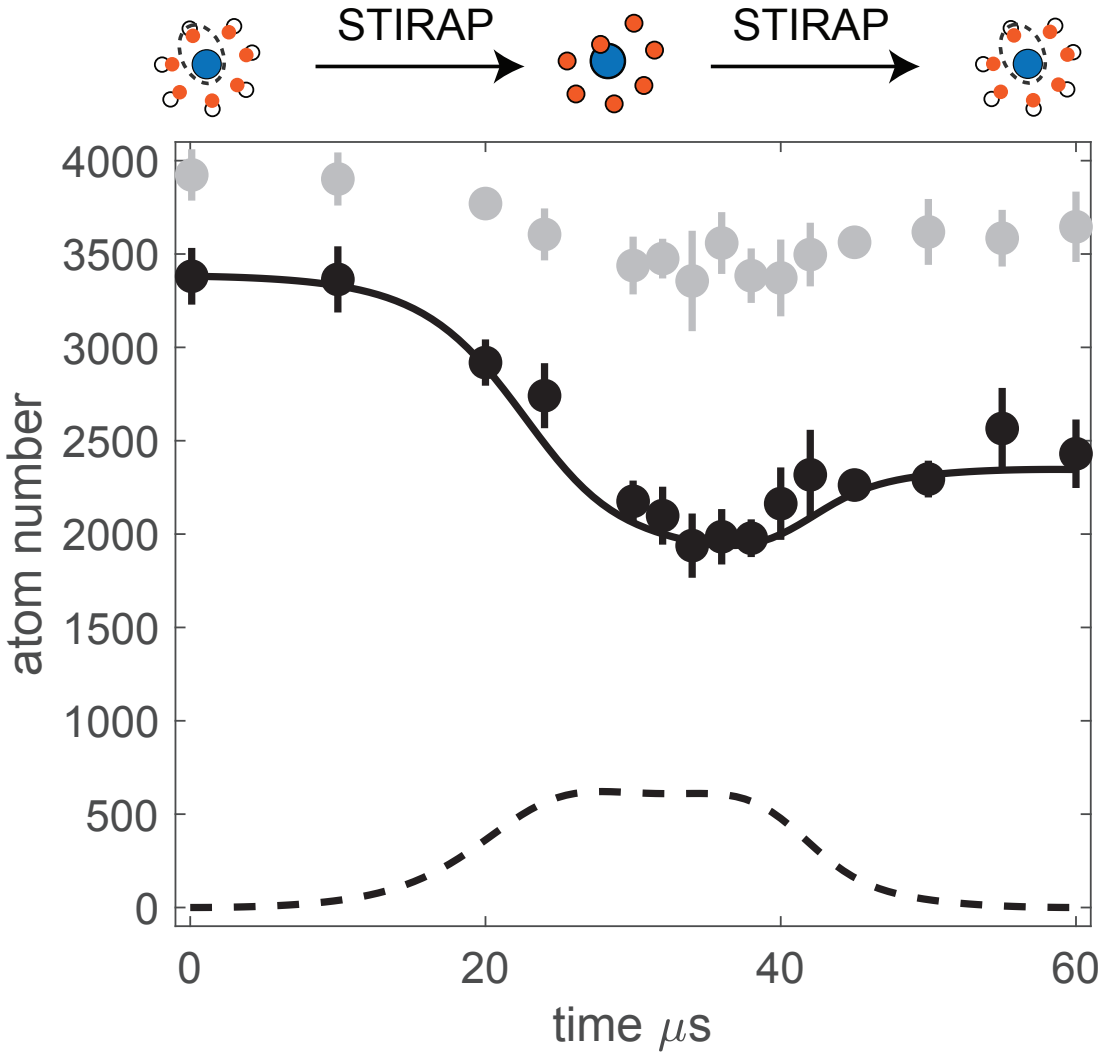


Figure 5-10: Coherent population transfer from strongly interacting Bose polarons to the absolute ground state molecules via two-photon STIRAP. Impurities immersed inside of the BEC Thomas-Fermi radius (black dots) show a coherent revival, in contrast to unperturbed impurities outside of the BEC (gray dots). Black dashed (solid) line is the ground state molecule (impurity) number based on a STIRAP model with an extra spectator continuum state. Thirty percent STIRAP single trip efficiency is observed and six-hundred dipolar molecules are created inside of the BEC.

sociation and STIRAP efficiency are accounted for. Our prior work reported a 11% free fermion-to-ground state molecule efficiency with Feshbach molecules as an intermediate step [83, 56] (15% Feshbach molecule radio-frequency association and 75% single STIRAP efficiency). Recent experiments have achieved 6–20% free fermion-to-

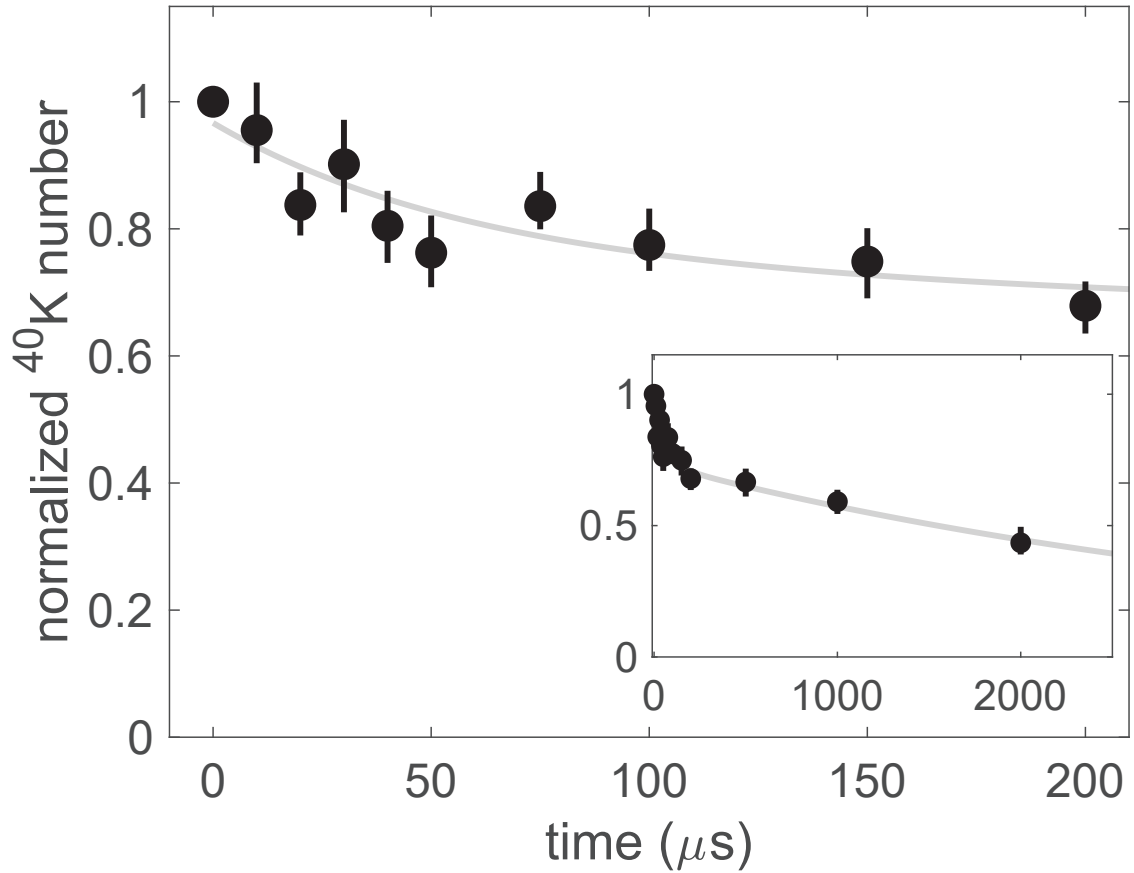


Figure 5-11: Dipolar ground state molecule lifetime inside of a BEC. A concatenated exponential time decay fits the ground state molecule data $N_F = N_0 e^{-\tau_m t} e^{-\tau_p t}$, where τ_m is the ground state molecule exponential constant, and τ_p is lifetime constant for the background polaron. The fit yields background polaron lifetime $\tau_p = 3 \text{ ms}$, which is in agreement with the independent measurement of the polaron lifetime time without STIRAP process. We measure the ground state molecule lifetime $\tau_m = 60 \mu\text{s}$ inside of the BEC with peak boson density $n_B = 7 \times 10^{13} \text{ cm}^{-3}$. We estimate the ground state molecule have $\beta = 2.4 \times 10^{-10} \text{ cm}^3/\text{s}$.

ground state molecule transfer via magnetic association that converts a large portion of the BEC into Feshbach molecules [1, 6, 29, 13]. Feshbach molecules have the disadvantage of a short lifetime due to rapid three-body recombinations with the surrounding bosons. We measure the NaK Feshbach molecules with Na to have a loss rate of $\beta = 10^{-10} \text{ cm}^3/\text{s}$. Polarons even at near unitarity-limited interactions have 50 times slower loss rate, $\beta = 5 \times 10^{-12} \text{ cm}^3/\text{s}$, which makes the polaron a much more stable initial state. Direct transfer from polarons creates a unique opportunity for ground state molecules to interact with the BEC. Unfortunately, the NaK ground state molecules are chemically reactive to Na, which results in a two-body loss rate of $\beta = 3 \times 10^{-10} \text{ cm}^3/\text{s}$. However, the novel BEC-ground state molecule interactions may be achieved with molecule species that are chemically stable [54] or that have Feshbach resonances with their constituent bosons [72]. Polarons created in this work are held in a harmonic trap, which creates a spatially dependent dressing. We propose a box trap as an ideal configuration for creating NaK ground state molecules via the polaron pathway. Bosons held in a box trap have a flattop density distribution and condense without changing their spatial distributions [35]. Fermions can be uniformly dressed by the bosons. We have an opportunity to create an equal Bose-Fermi mixture, where the entire box of atoms can be associated into the ground state molecules.

5.6.1 Comparison with Feshbach molecule approach

Bose polaron up-leg coupling is in the unitarity limited regime, which limits the STIRAP transfer efficiency within the practical up-leg laser power and coherence time provided by the BEC bath. However, the overall molecule creation efficiency deserves a subtle discussion. The overall molecule creation starts from the atomic sample, before Feshbach molecules are associated via rf or magnetic field sweep. The Feshbach molecule association process carries finite efficiency, which is typically the limiting factor in the overall molecule creation. The overall molecule creation efficiency $\eta_{overall}$ is a convolution of Feshbach molecule and STIRAP transfer efficiency $\eta_{overall} = \eta_{Feshbachmolecule} \times \eta_{STIRAP}$. Fig. 5-12 demonstrates the STIRAP time evo-

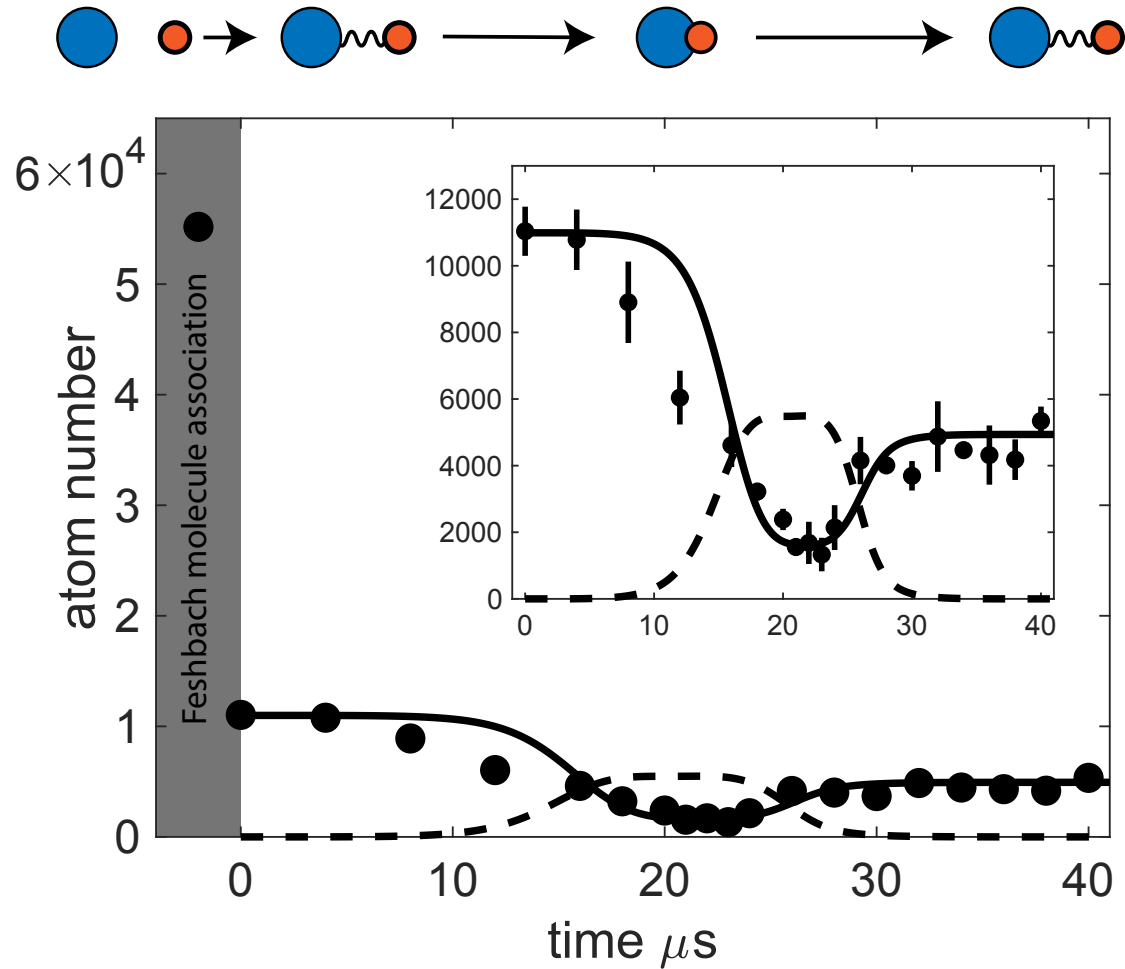


Figure 5-12: Typical Feshbach molecule STIRAP with rf association efficiency included. Free atom pairs to Feshbach molecule typically have 20% rf association efficiency. Inset shows STIRAP time evolution details.

lution that starts prior to Feshbach molecule association. Table 5.1 summarizes the overall molecule creation efficiency in recent published work. The direct STIRAP transfer from Bose polaron holds the highest fermion to ground state molecule efficiency. The notable advantage of the Bose polaron to ground state molecule is that majority boson bath remains intact, which is the starting point for realizing angulon.

Experiments	T/T _c	$\eta_{\text{Feshbach molecule}}^*$	η_{STIRAP}	η_{overall}
²³ Na ⁴⁰ K [29]	0.74	27.8%	80%	22%
²³ Na ⁴⁰ K [14]	0.58	11%	70%	7.8%
⁴⁰ K ⁸⁷ Rb [1]	0.5	7%	90%	6.3%
²³ Na ⁴⁰ K [this work]	0.1	unnecessary	30%	30%

Table 5.1: List of recent experiments on converting Bose-Fermi mixtures to ground state molecules. $\eta_{\text{Feshbach molecule}}$ is the Feshbach molecule association efficiency for fermions. This thesis work directly transfers strongly interacting Bose polarons to dipolar molecules, therefore the Feshbach molecule association stage is not needed. The last column η_{overall} states the overall Bose-Fermi mixture to ground state molecule efficiency $\eta_{\text{overall}} = \eta_{\text{Feshbach molecule}} * \eta_{\text{STIRAP}}$.

5.7 Simple STIRAP model

STIRAP is a popular technique that is practiced in almost all the bi-alkali experiments to create quantum degenerate ground state molecules. While no fundamental difference to other two-photon Raman protocols, STIRAP gains its popularity for its robustness against timing, laser intensity inhomogeneity, and laser power fluctuations. As an adiabatic transfer protocol, STIRAP does not have an analytic formula. Therefore we develop a STIRAP toy model based on dressed state approach to gain intuitions on achieving optimal transfer efficiency. First we start with a three-level system shown in Fig. 5-13b. The system can be described by a 3-by-3 Hamiltonian,

$$H(t) = \frac{1}{2} \begin{pmatrix} 2\delta_i & \Omega_1(t) & 0 \\ \Omega_1(t) & i\gamma_e & \Omega_2(t) \\ 0 & \Omega_2(t) & 2\delta_g \end{pmatrix} \quad (5.1)$$

The time evolution of probability amplitudes c_i, c_e, c_g are governed by a time-dependent Hamiltonian $H(t)$ via Schrodinger equation,

$$\frac{d}{dt} \begin{pmatrix} c_i \\ c_e \\ c_g \end{pmatrix} = \frac{1}{2} \begin{pmatrix} 2\delta_i & \Omega_1(t) & 0 \\ \Omega_1(t) & i\gamma_e & \Omega_2(t) \\ 0 & \Omega_2(t) & 2\delta_g \end{pmatrix} \begin{pmatrix} c_i \\ c_e \\ c_g \end{pmatrix} \quad (5.2)$$

The matrix element $\langle i | H(t) | g \rangle \equiv 0$ manifests the lack of direct coupling between the initial state $|i\rangle$ and the target ground molecule state $|g\rangle$. The STIRAP protocol circumvents this lack of direct coupling with help of a third intermediate state $|e\rangle$ that couples to both the initial and ground states with Ω_1 and Ω_2 Rabi rates. For bi-alkali mixtures, the STIRAP intermediate state is typically electronically excited molecular states, which have rapid dissipation rate γ_e due to the excited molecule spontaneously decaying to lower-lying states, which is implemented by the imaginary term $i\gamma_e$ in the Hamiltonian. The STIRAP pulse is engineered to minimally populate the dissipative excited state by stay in the dark state. Fig. 5-13a demonstrates the ‘counter-intuitive’ STIRAP ramping sequence where the dark state smoothly evolves from the initial state to the ground state and back. For the on resonant scenario ($\delta_g = \delta_i = 0$), three eigenstates of the Hamiltonian $H(t)$ are superpositions of bare states $|i\rangle, |e\rangle, |g\rangle$. Three eigenstates can be separated into ‘dark’ and ‘bright’ based on their eigenenergies: a dark dressed state $|D\rangle$ has constant zero energy $E_D = 0$, and two bright dressed states $|B_{\pm}\rangle$ with complex eigenenergies

$$E_{B_{\pm}} = \frac{1}{4}(i\gamma_e \pm \sqrt{4(\Omega_1(t)^2 + \Omega_2(t)^2) - \gamma_e^2}). \quad (5.3)$$

The STIRAP efficiency depends on the energy gap Δ_B that separates the dark state from its nearest bright state. Shown in Fig. 5-13c, the most critical moment for the STIRAP transfer is when the Δ_B is the narrowest, which is also the moment when system total population loss occurs at $t = 1.5\tau_{STIRAP}$ and $2.5\tau_{STIRAP}$ shown as gray line in Fig. 5-13b.

5.7.1 STIRAP in over-damped regime

Over-damping happens when the excited state dissipation dominates over STIRAP Rabi rate: $\Omega = \sqrt{\Omega_1(t)^2 + \Omega_2(t)^2} < 2\gamma_e$. Fig. 5-14 shows the bright eigenenergy are purely imaginary in the over-damped regime. Notably, most STIRAP in bi-alkali experiments are in the ‘over-damped’ regime. The $^{23}\text{Na}^{40}\text{K}$ electronically excited molecules have spontaneous decay rate $\gamma_e = (2\pi)10$ MHz. In practice, the decay rate

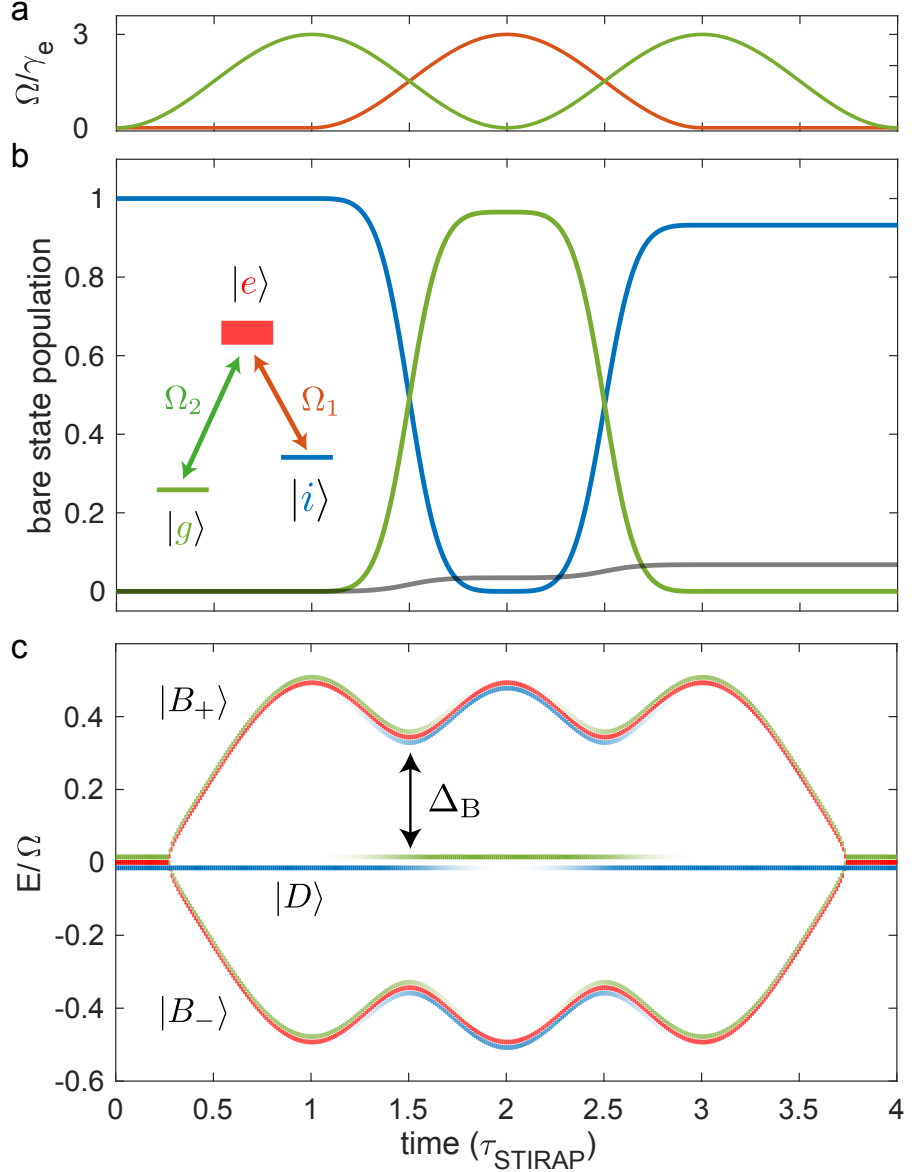


Figure 5-13: Time evolution of the three level system during STIRAP. a. Up-leg (orange) and down-leg (green) Rabi rates during STIRAP. The STIRAP ramps on in a counter-intuitive fashion in order to adiabatically tilt the dark state from initial state to the ground molecule state. b. Bare state population time evolution. Starting from $t = 0$, the free-atom like initial state (blue) evolves into the ground state molecules (green). The gray line shows the population loss via the excited state due to non-perfect adiabatic condition. c. Dressed state energy. Diagonalizing the system Hamiltonian leads to three eigenstates that are superpositions of initial, excited, and ground state. The STIRAP transfer efficiency is most sensitive at cross point of two up/down-leg Rabi rates, the energy gap Δ between the dark state at energy $E = 0$ and the bright state becomes narrowest which sets the transfer adiabatic condition. Satisfying the adiabatic condition guarantees the dark state evolves from initial state (blue) to the ground state (green) with minimum loss.

is much larger than STIRAP Rabi rates due to laser power budget. Furthermore, ground state molecule hyperfine states impose another constraint on STIRAP Rabi rate upper limit. For ground state $^{23}\text{Na}^{40}\text{K}$ molecules, hyperfine states are ≈ 100 kHz apart [57], which requires $>10 \mu\text{s}$ and < 100 kHz effective Rabi rate to resolve. Authors in [50] observe that effective STIRAP Rabi rate larger than 100 kHz leads to superposition and interference of hyperfine states, adding complications to ground state molecule creation.

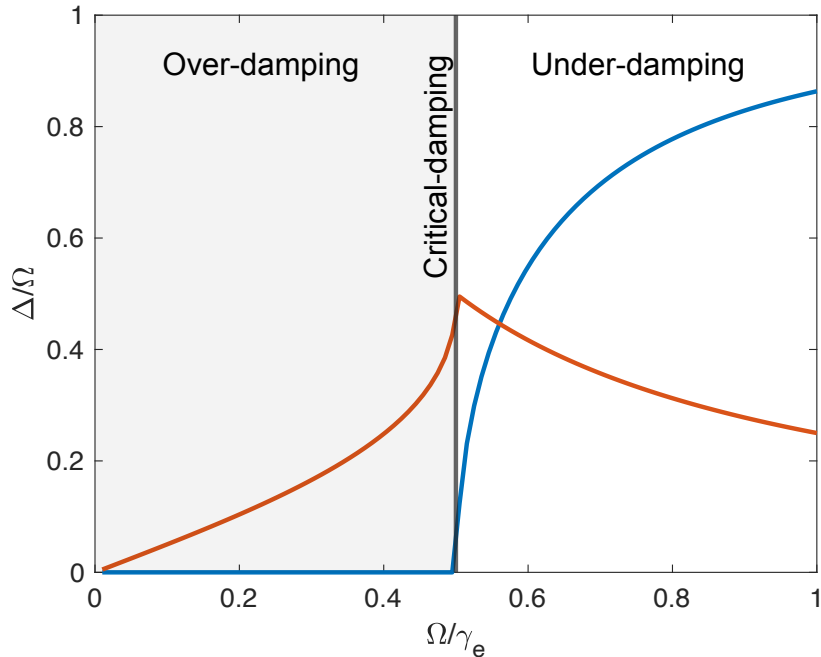


Figure 5-14: Damping effects on energy gap at the STIRAP critical moment. The energy separation from the dark state and the nearest bright state are plotted in orange for imaginary part and blue for the real part. The center line at $\Omega/\gamma_e = 0.5$ separates the system into under-damping and over-damping regimes. The real part of the energy separation collapses to 0 in the over-damp regime. Adiabatic transfer purely relies the imaginary energy gap opening in the over-damped system.

In this over-damped regime, high STIRAP efficiency purely relies on the opening of imaginary bright state energy gap, and the speed the process sweep across the gap. In Chapter 4, the STIRAP efficiency is modeled by a simple Eqn. 4.5. Fig. 5-15d shows that the STIRAP efficiency from the simple model agrees very well with the result from numerically solving the three-level system. In summary for this subsection, we

demonstrated that the dressed state picture provides a valid intuition on STIRAP efficiency even in the over-damped regime. In the next section, we introduce another subtlety of STIRAP from the free-particle continuum.

5.7.2 Free-particle continuum influence

We observe the spectral red-shift effect on Bose polaron photoassociation caused by the nearby free-particle continuum in Chapter 3. The continuum also plays a significant role in the direct STIRAP on Bose polarons. We propose to use a single level to approximate the continuum effect on STIRAP with a 4-by-4 Hamiltonian H_c

$$H_c(t) = \frac{1}{2} \begin{pmatrix} 2\delta_i & 0 & \Omega_1(t) & 0 \\ 0 & 2\delta_c & \Omega_c(t) & 0 \\ \Omega_1(t) & \Omega_c(t) & i\gamma_e & \Omega_2(t) \\ 0 & 0 & \Omega_2(t) & 2\delta_g \end{pmatrix} \quad (5.4)$$

Fig. 5-16a shows that the initial state is below the continuum by its self-energy E_i . The up-leg laser, that couples the initial state, also near-resonantly couples the continuum state $|c\rangle$ to the excited state with a Rabi rate $\Omega_c(t)$, which results the self-consistent detuning condition $\delta_i - \delta_c \equiv E_i$. The presence of the continuum leads to a second ‘quasi-dark’ dressed state that we have to avoid crossing during STIRAP. Shown in Fig. 5-16c, as the down-leg ramps down and up-leg ramps up, the quasi-dark state evolves from initially bare continuum to a dressed state that is Δ_D away from the true dark state at 0. The small Δ_D separation leads poor STIRAP efficiency, as the system population diabatically transfers to the quasi-dark state, instead of evolving to the ground molecules. Bose polaron has $- \approx 16$ kHz self-energy at near unitarity limited interaction. Given the absorption imaging technique having 10 MHz resolution, the continuum cannot be resolved from the polaron, therefore crossing to the quasi-dark state leads to low STIRAP contrast, while crossing to the bright state results to system population loss. The continuum effect on STIRAP can be mitigated by red-detuning lasers from single-photon resonance. Fig. 5-17 illustrates

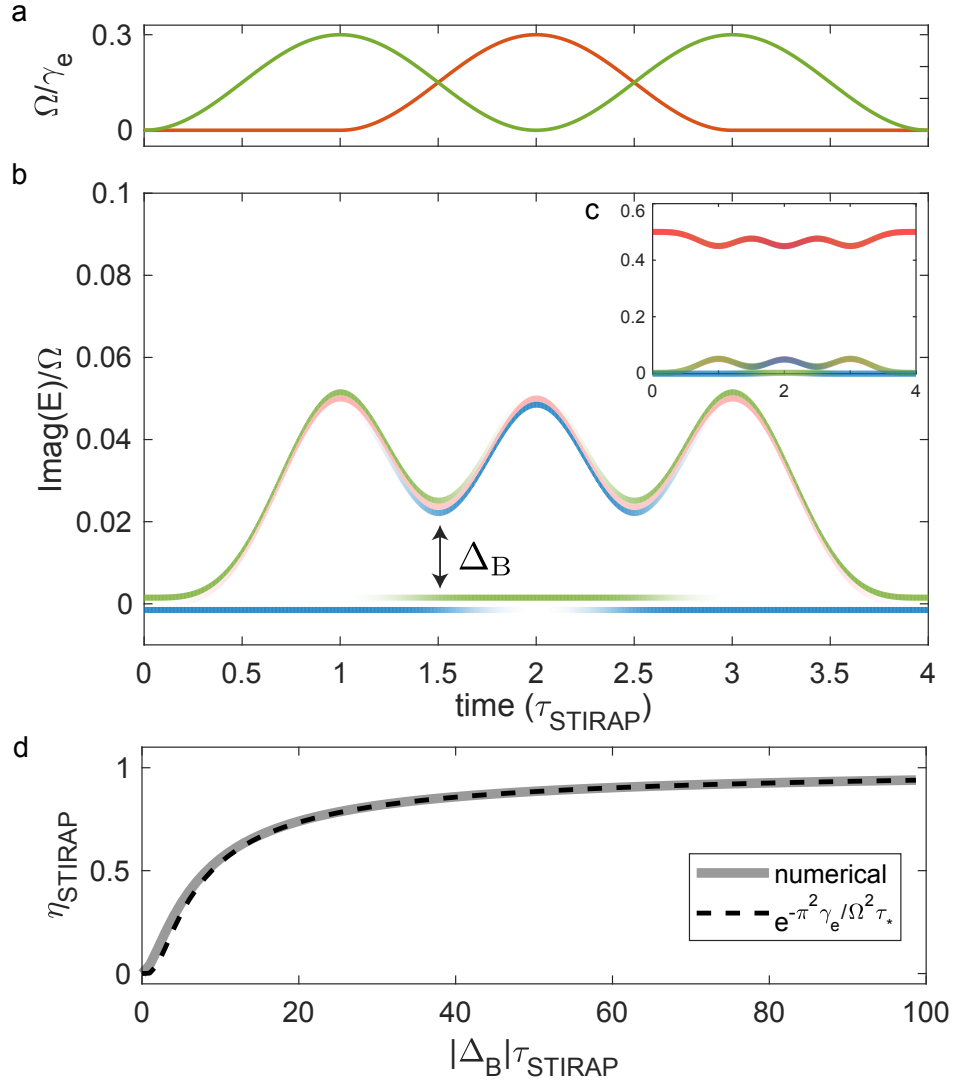


Figure 5-15: Dressed state energy evolution during STIRAP ramp in the over-damped regime. a. Up-leg (orange) and down-leg (green) Rabi rate ramp. Both legs have an equal peak rate $\Omega = \gamma_e/3$, placing the system in the over-damp regime. b. The bright state imaginary energy evolution during the STIRAP ramp. The color indicates bare state superpositions in each dress state: initial state in blue, excited state in red, and ground molecule state in green, and the intensity indicates bare state amplitudes. Δ_B marks the most critical moment during STIRAP where the bright state is closest to the dark state. c. Inset shows energies of all 3 dressed states. d. Comparison of STIRAP efficiency from numerical solution and phenomenological equation. The gray solid line indicates the STIRAP efficiency via numerically solving the system dynamic Eqn. 5.2; the black dashed line shows phenomenological expression $\eta_{\text{STIRAP}} = \exp(-\frac{\pi^2 \gamma}{\Omega^2 \tau_*})$ with $\tau_* = 0.8\tau_{\text{STIRAP}}$.

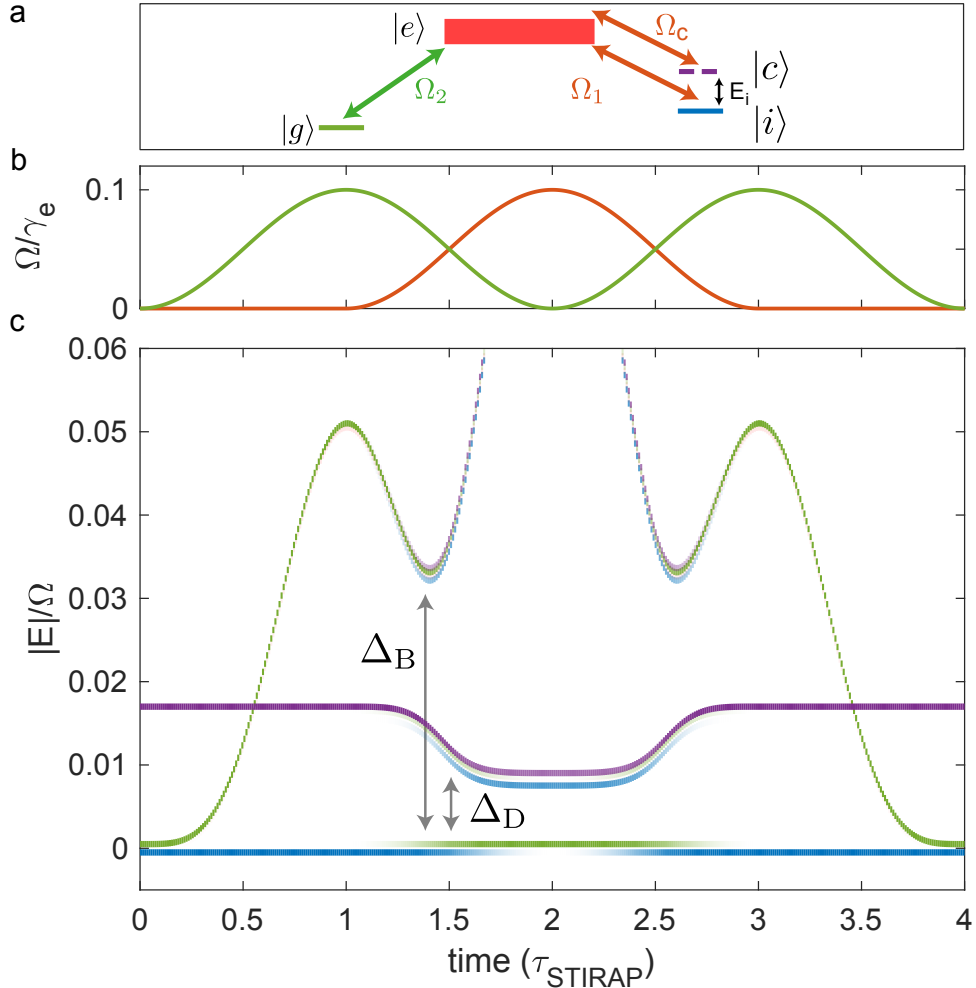


Figure 5-16: Free-particle continuum participation during STIRAP. a. Four level systems diagram. We use a single level $|c\rangle$ shown in purple dashed line to approximate the free-particle continuum effect. The initial state $|i\rangle$ with self-energy E_i is below the free-particle continuum. The up-leg laser connects both $|i\rangle$ and $|c\rangle$ to the excited state $|e\rangle$ with Rabi rates Ω_1 and Ω_c . The excited state has spontaneous decay rate γ_e . The down-leg laser connects $|e\rangle$ to the ground state $|g\rangle$ with Rabi rate Ω_2 . b. Sinusoidal ramp of up-leg and down-leg Rabi rates with equal peak amplitude $\Omega = 0.1\gamma_e$, placing the system in over-damped regime. c. Dressed state energy time evolution during the STIRAP process. The true dark state remains constantly at $E = 0$. At $t = 1.5\tau_{\text{STIRAP}}$, the most critical moment for STIRAP, the bright state is separated from the true dark state by an energy gap Δ_B . Due to the continuum participation, a second quasi-dark state has energy Δ_D separation from the true dark state. The crossing to the second dark state reduces the ground state transfer efficiency and STIRAP contrast by populating the continuum state, which is typically indistinguishable from the initial state. Parameters used in the calculations are $\gamma_e/2\pi = 10$ MHz, peak $\Omega_{1,2}/2\pi = 1$ MHz, $E_i/2\pi = -16$ kHz, single STIRAP pulse time $\tau_{\text{STIRAP}} = 30$ μ s, and $\delta_{1\text{photon}} = \delta_{2\text{photon}} = 0$.

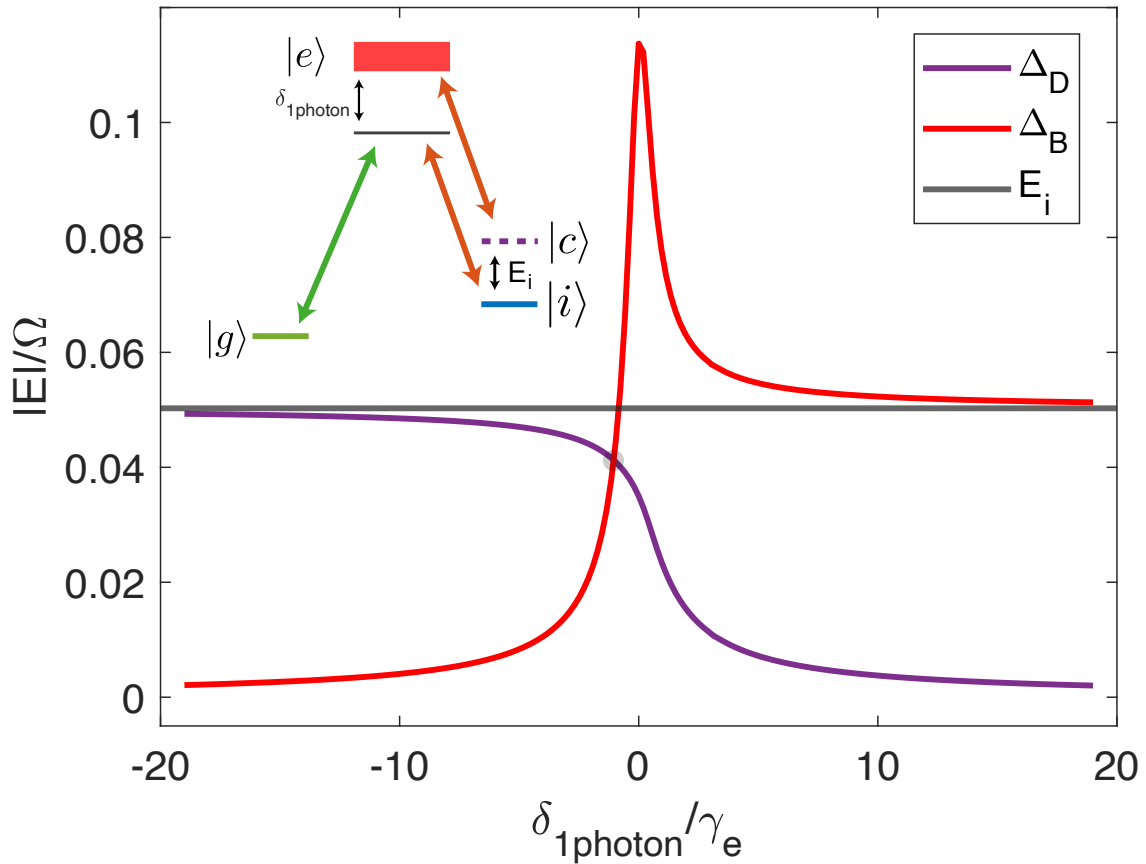


Figure 5-17: Dressed state energy gaps in relation with single photon detuning. Negatively shifting single photon detuning $\delta_{1\text{photon}}$ opens up the quasi-dark state energy gap Δ_D , while the bright state energy gap Δ_B closes down. The optimal STIRAP efficiency is achieved at the compromised $\delta_{1\text{photon}}$ region where Δ_B and Δ_D cross. At far red detuned $\delta_{1\text{photon}}$ the quasi-dark state energy gap approaches the bare initial state energy. Similarly, at far blue detuned $\delta_{1\text{photon}}$, the bright state energy gap approaches the bare initial state energy.

the quasi-dark state gap Δ_D opens up at negative $\delta_{1\text{photon}}$, while at the same time the bright state gap Δ_B closes down. The optimal STIRAP efficiency is achieved at a compromised one-photon detuning where both bright and dark state energy gaps are equally resolvable, which agrees with our experimental discovery. In the next section, we present a STIRAP transfer data via the triplet-rich excited state, which has better coupling to the initial and continuum state than the balanced excited state.

5.7.3 Polaron to ground state molecule via the triplet-rich excited state

In addition to creating ground state molecules via the balanced excited state, we also perform STIRAP via the triplet-rich excited state. Compared with the balanced excited state, the triplet-rich excited state has stronger coupling to both the Bose-Fermi mixture initial state. However, the triplet-rich excited state also has enhanced coupling to the free-particle continuum. Given the experimental constraints of laser power, coherence time, and ground state molecule lifetime, we achieve the optimal STIRAP signal with singlet-photon detuning $\delta_{1photon}/2\pi = -13.75$ MHz and single STIRAP ramp time $\tau_{STIRAP} = 30 \mu s$. Fig. 5-18 shows the STIRAP time evolution of Bose polaron via the triplet-rich excited state, which has reduced contrast due to the strong continuum influence. We expect the triplet-rich excited state strong coupling can be realized with Feshbach molecules, which are further away from the continuum from their larger binding energy than Bose polarons.

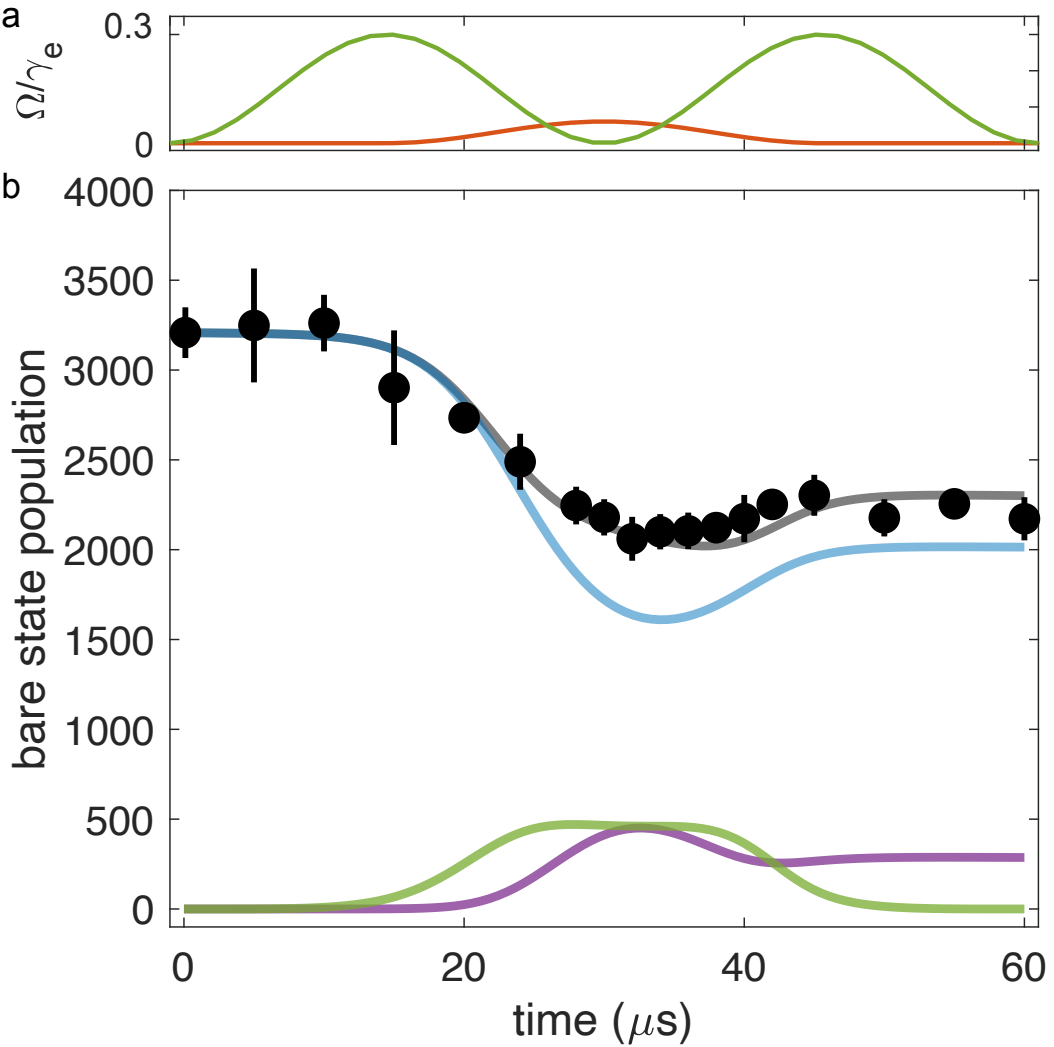


Figure 5-18: STIRAP time evolution from strongly interacting Bose polarons to ground state molecules via the triplet-rich excited state. a. Up-leg (orange) and down-leg (green) Rabi rate ramps. b. Bare states population during the STIRAP ramp. The initial Bose-Fermi mixture is prepared in the same condition as experiments performed in Fig. 5-10. Black dots are measured ${}^{40}\text{K}$ atoms that are within the BEC Thomas-Fermi radius. The gray line is the theory calculation of ${}^{40}\text{K}$ population, which is the summation of the initial polaron (blue line) and the continuum population (purple line). The continuum state is indistinguishable from the initial polaron state by the absorption image. The green line indicates the ground state molecule population. The STIRAP contrast and ground state molecule creation efficiency is impaired by the continuum participation.

Chapter 6

Outlook

6.1 Box trap

6.2 Microwave dressing

Microwave cavity.

6.3 Down-leg dressing

6.4 Molecule microscope

Appendix A

STIRAP Laser System

Lasers used to drive the STIRAP process are frequency stabilized in several stages.

The up-leg light field is derived from a highly tunable Titanium-Sapphire (TiSa) laser manufactured by M-squared.

The down-leg laser field is provided by a dye laser with a intra-cavity electro-optic modulator (EOM).

Both down-leg and up-leg are frequency locked to a ultra low expansion (ULE) cavity that has ≈ 45 kHz linewidth.

The down-leg laser is first locked to its built-in reference cavity via mechanical modulators such as galvo and tweeter mirrors that has bandwidth of 40 kHz.

This reference cavity slow lock gives the down-leg laser ≈ 1 MHz frequency stability.

The PDH lock signal from the ULE cavity further stabilizes the down-leg laser via the intra-cavity EOM in two paths: mid-range (0-100 kHz) and fast-range lock (100-300 kHz).

A high-voltage op-amp ($V_{pp} \approx 400$ V) gets the PDH error signal and the amplified control voltage feeds into one of the EOM electrode.

The mid-range lock bandwidth is limited by the op-amp speed. The fast-range lock control feeds into the second EOM electrode whose bandwidth is limited by an EOM resonance at 300 kHz.

The up-leg laser is a simple two-component lock: a slow piezo and a fast piezo

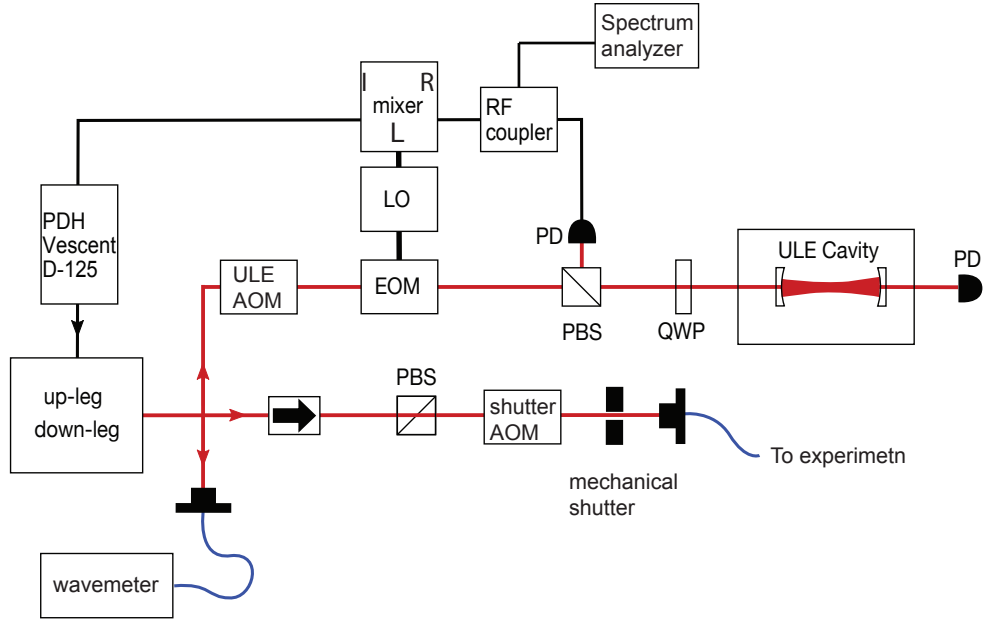


Figure A-1: PDH lock optical and electronics schematics.

stacked together inside the TiSa inner cavity.

The slow piezo lock has 10 kHz bandwidth and the fast piezo has 50 kHz bandwidth. Both components are limited by piezo resonance.

We achieve <1 kHz laser linewidth back out from PDH lock error signal and ULE cavity linewidth.

A simple ‘beta-line’ model based on [25] estimates the laser linewidth to a reasonable approximation, which is discussed in the Appendix A Fig. A-1 and Fig. A-2. The beta-line method converts the PDH error signal to frequency noise based on the ULE cavity linewidth. However, beta-line model usually sets a coherence time upper bound, because components after the laser lock servo typically introduces more noises.

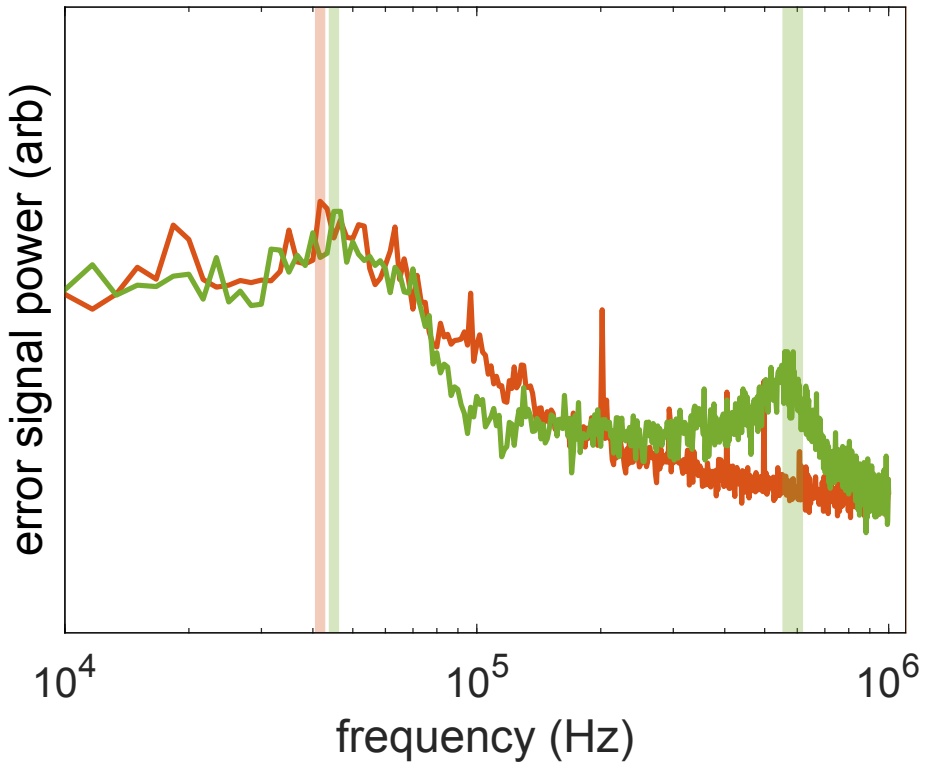


Figure A-2: STIRAP laser error signal power spectrum. Green/orange: down-leg/up-leg error signal power spectrum. Orange shade marks the up-leg laser servo bump at 42 kHz due to the first TiSa piezo resonance. Two green shades marks the down-leg laser servo bumps: first servo bump at 45 kHz that is due to the mechanical galvo/tweeter inside the dye laser, and the second servo bump at 590 kHz is due to intra-cavity EOM resonance.

A.1 Pound-Drever-Hall lock

A.2 Intra-cavity EOM Interference Filter Lasers

Appendix B

Theoretical description of Bose polaron

The calculated effective mass enhancement is shown in Fig.?. At the strongest coupling, $g_{bf}^{-1} = 0$, the Bose polaron effective mass increases by $0.2m_b$ as the result of the strong dressing. The effective mass asymptotically approaches to $m_f + m_b$ due to the nature of the scattering potential, where a boson and a fermion form a bound molecule.

Appendix C

Atom calibrations

We use the boson phase transition from thermal to BEC to calibrate the camera counts to atom number. Fermion atom number is benchmarked to the boson number with ground state molecules: first a single STIRAP pulse associate Feshbach molecules into ground state molecules; second resonant lights remove remaining atoms; third a second STIRAP pulse converts ground state molecules into atoms where fermions and bosons have one-to-one ratio. We first demonstrate how to use bosons near a BEC transition to calibrate boson atom number.

C.1 Boson atom number calibration

Thermal bosons trapped in a harmonic trap have Gaussian-like distribution; in contrast, Bose-Einstein condensed bosons ‘mirror’ the harmonic trap shape due to inter-boson interaction. Linedensity distribution of condensed and thermal bosons are visually different and here we developed a robust 3 stage fitting procedure to characterize boson condensation fraction near its BEC phase transition temperature T_c . With optical dipole trap frequencies measured independently, and temperature from thermal wings, we will use the Bose statistics at onset of BEC to calibrate the camera N count to absolute atom number. We experimentally vary the initial MOT loading time to change total boson number in the end of optical dipole trap cooling and the bosonic ^{23}Na in $|F, mF\rangle = |1, 1\rangle$ state.

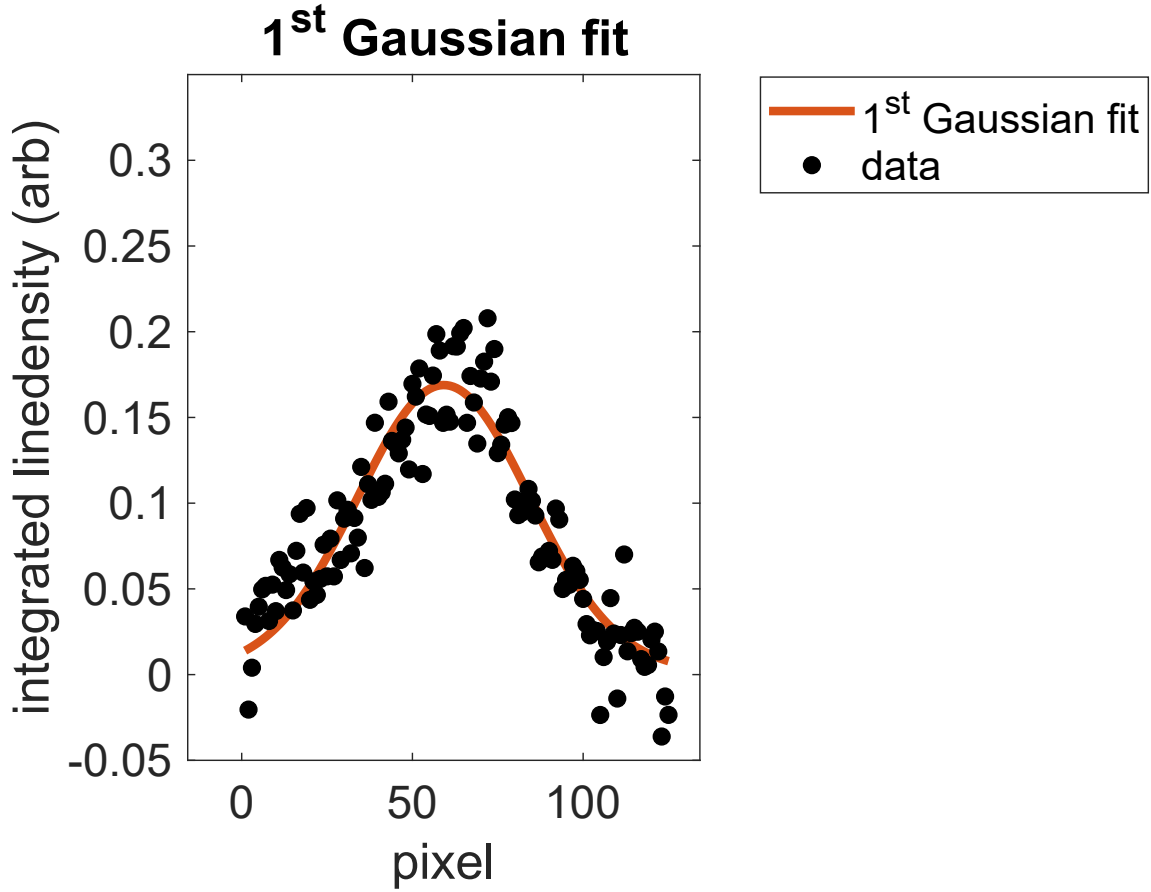


Figure C-1: First Gaussian fit does reasonably robust job to find where the boson assemble center is. However, we can clearly observe the Gaussian profile does not fit the center part of linedensity very well.

C.1.1 Gaussian and bimodal fits

We do a three-stage fitting to make the model reliable on both BEC and thermal data. First a Gaussian distribution (f_1) fits the boson linedensity, where the boson thermal wing and rough center are found,

$$f_1(x) = A \cdot e^{-\frac{(x-x_0)^2}{\sigma^2}} \quad (\text{C.1})$$

A second Gaussian fit (f_2) ‘masks’ out the center part of the linedensity thus only takes the thermal wing into account.

At this stage, we have a good sense on the boson thermal wing property. We do

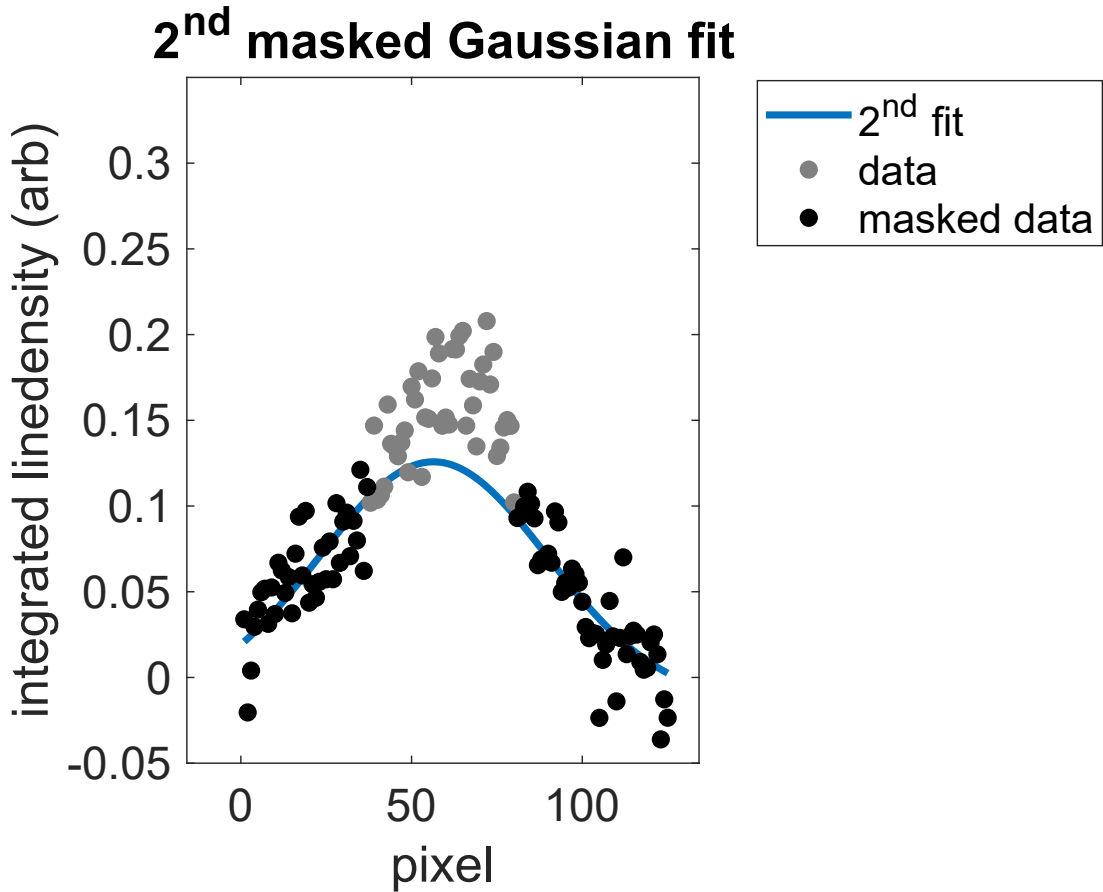


Figure C-2: Second Gaussian fit with center linedensity excluded. Black dots: data used for the second Gaussian fitting. Gray dots: excluded data in the center. The second fit result, shown in blue line, indicates the BEC bimodal distribution where the condensed boson linedensity in the center is much higher.

a final fit (f_3) with a ‘BEC’ amplitude B ,

$$f_3(x) = Ae^{-\frac{(x-x_0)^2}{\sigma^2}} + B(1 - (\frac{x-x_0}{r_{TF}})^2)\Theta(1 - (\frac{x-x_0}{r_{TF}})^2) \quad (C.2)$$

When $T > T_c$, $B = 0$ reflects a pure thermal boson ensemble; when $T < T_c$, $B > 0$ will reveal the condensate fraction.

C.1.2 Temperature calibration

The trapped boson temperature can be estimated from its second Gaussian fit. In a harmonic trap with trapping frequency $(\omega_x, \omega_y, \omega_z)/2\pi = (9, 112, 108.3)$ Hz, the boson

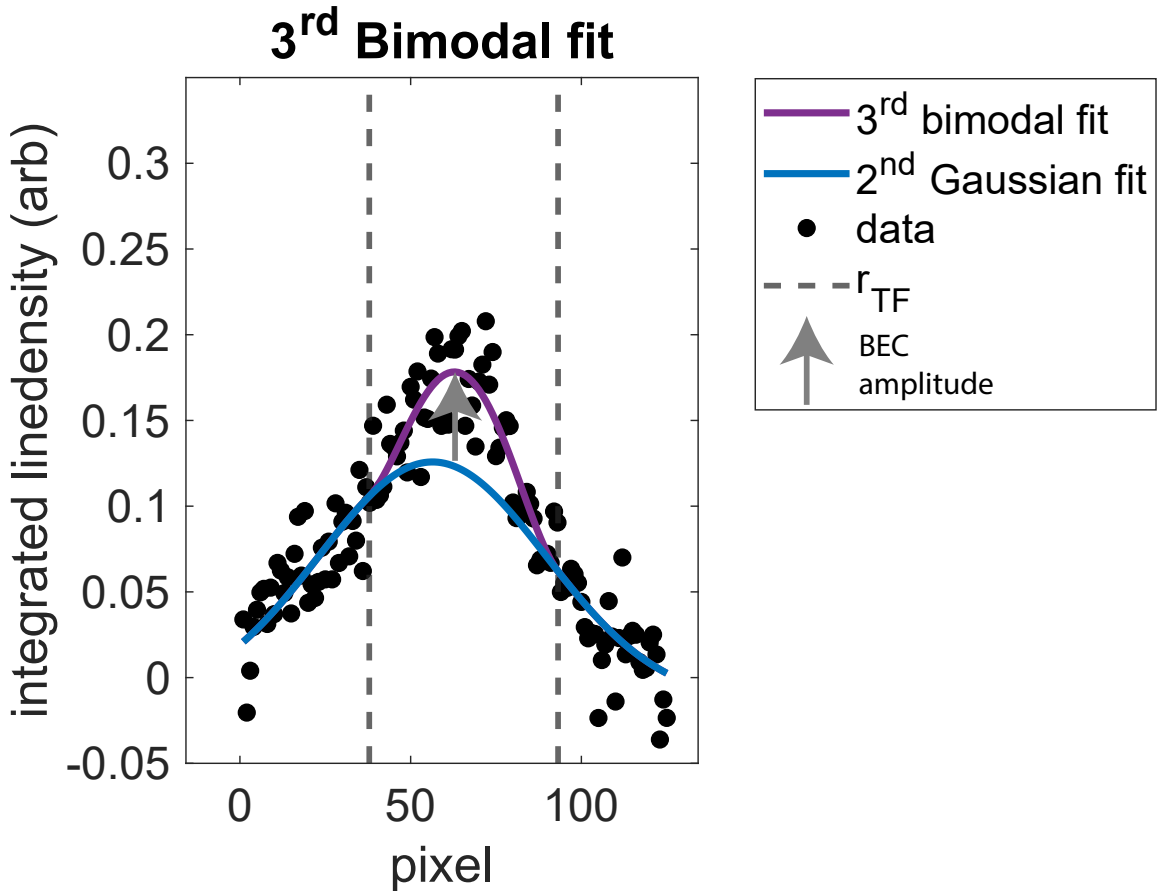


Figure C-3: Third bimodal fit. Purple line: bimodal fit result based on Eqn. C.2. Blue line: second Gaussian fit on the thermal wing. The Gaussian wing the third bimodal fit here is fixed. Dashed gray line: Thomas-Fermi radius r_{TF} . Gray arrow: BEC amplitude B from Eqn. C.2.

temperature T is related to the Gaussian wing width as,

$$k_B T = \frac{1}{2} m_B \omega_x^2 \sigma_x^2 \quad (\text{C.3})$$

Fig. C-4 shows temperature vs BEC amplitude that has little correlation. We have average temperature of 100 nK.

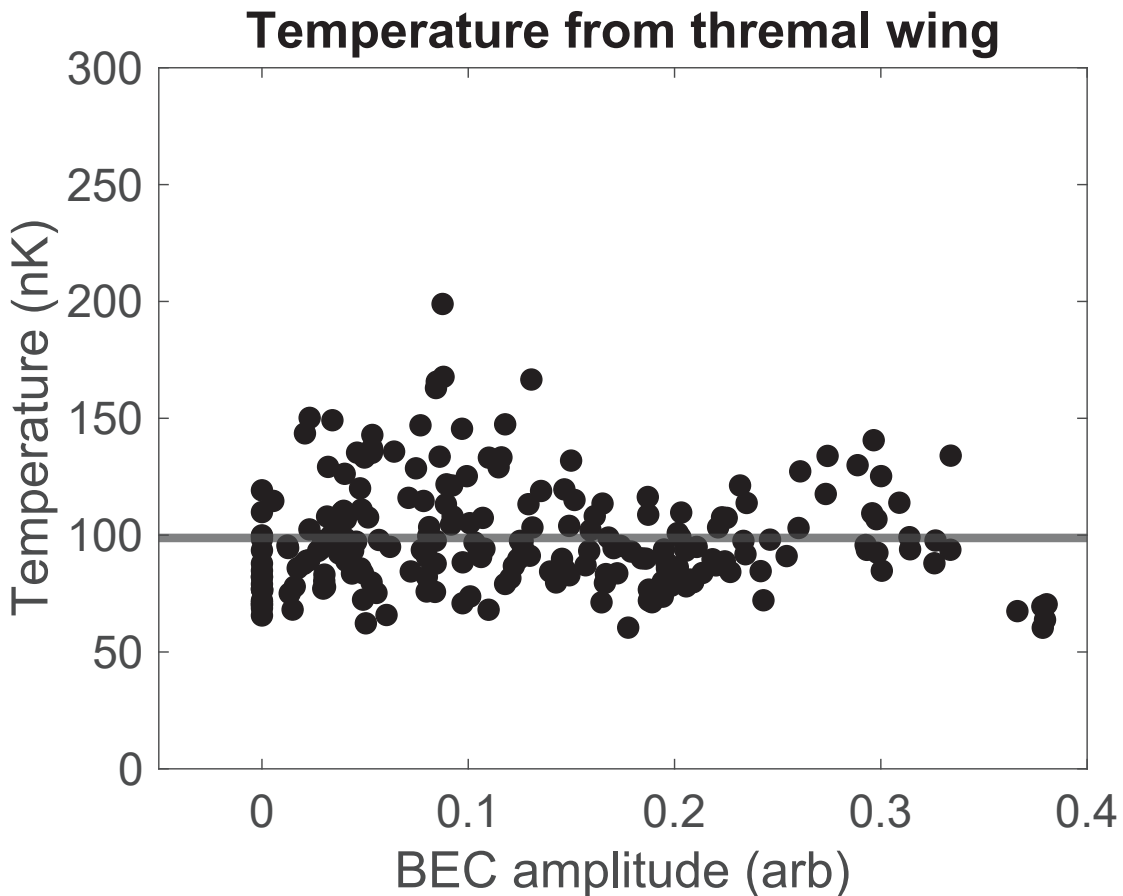


Figure C-4: Temperature extracted from the thermal wing fitted by second Gaussian f_2 . We observe no clear correlation between boson temperature and BEC size, since the temperature is set by the optical dipole trap evaporation end point, which is kept as constant during the measurement. We average to have boson at temperature $T = 100$ nK.

C.1.3 Atom number and BEC critical temperature

As a result of Bose statistics [22], number of condensed boson N_0 is related to temperature as

$$N - N_0 = \zeta(3) \left(\frac{k_B T}{\hbar \omega_{ho}} \right)^3 \quad (\text{C.4})$$

The condensate critical temperature is related to the absolute atom number in a harmonic trap as

$$k_B T_c = \hbar \omega_{ho} \left(\frac{N}{\zeta(3)} \right)^{1/3} \quad (\text{C.5})$$

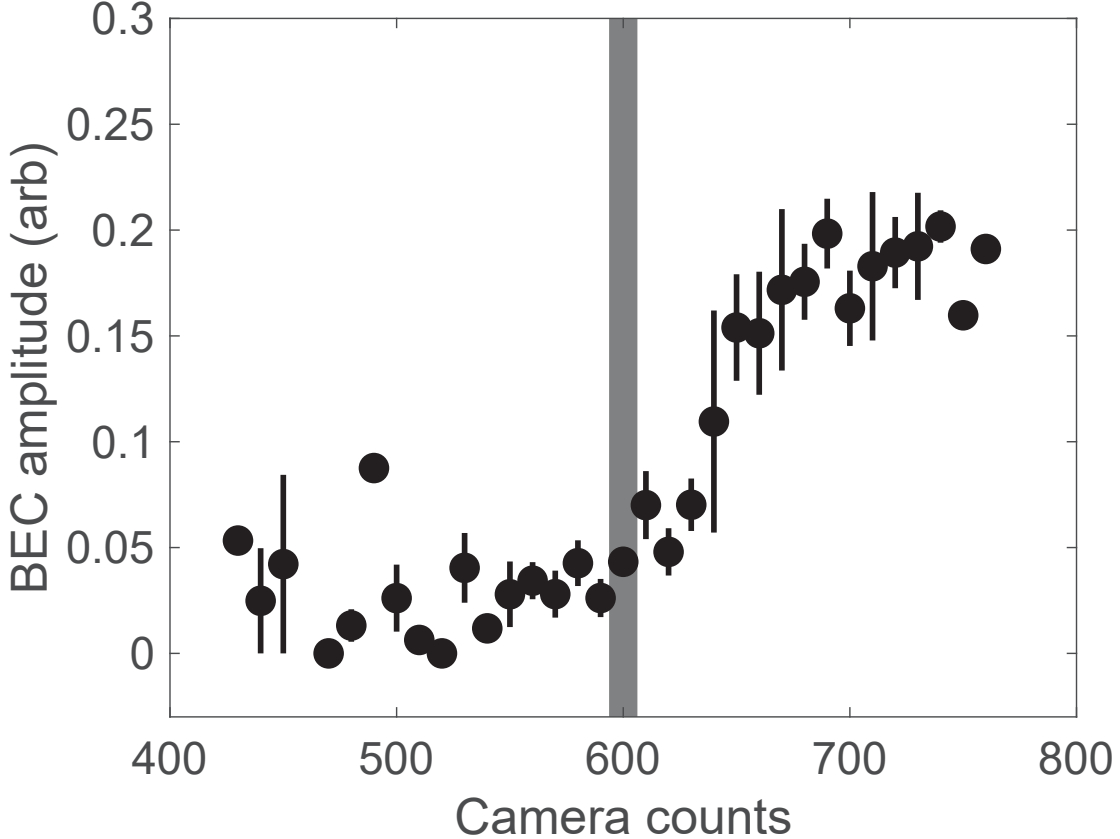


Figure C-5: Onset of the BEC amplitudes near condensate transition temperature. Gray shade indicates the camera counts at the critical temperature T_c .

where T_c is the BEC critical temperature, ω_{ho} is the harmonic trapping frequency, $\zeta(3)$ is the Riemann-Zeta function, and N is the boson atom number. Fig. C-5 shows that at the critical temperature T_c we observe fitted BEC amplitudes rise above zero. We utilize the camera counts at the boson phase transition $N_{camera} = 600$ to calibrate the absolute atom number N in Eqn. C.5. Based on our knowledge of our trap frequencies $\omega_{ho}/2\pi = 48$ Hz, and temperature $T = 100$ nK from thermal wing, we have $N \approx 96000$ atoms at the BEC transition temperature $T = T_c$. Therefore we conclude camera count: **160 atoms per camera N count.**

Fig. C-6 shows a textbook like BEC phase transition, where BEC amplitude rises above zero at $T/T_c \leq 1$. What is different from a text ‘cooling’ to phase transition is that we keep the boson assemble temperature constant, but we vary the boson loading time to change the total boson density in the end, therefore we vary critical

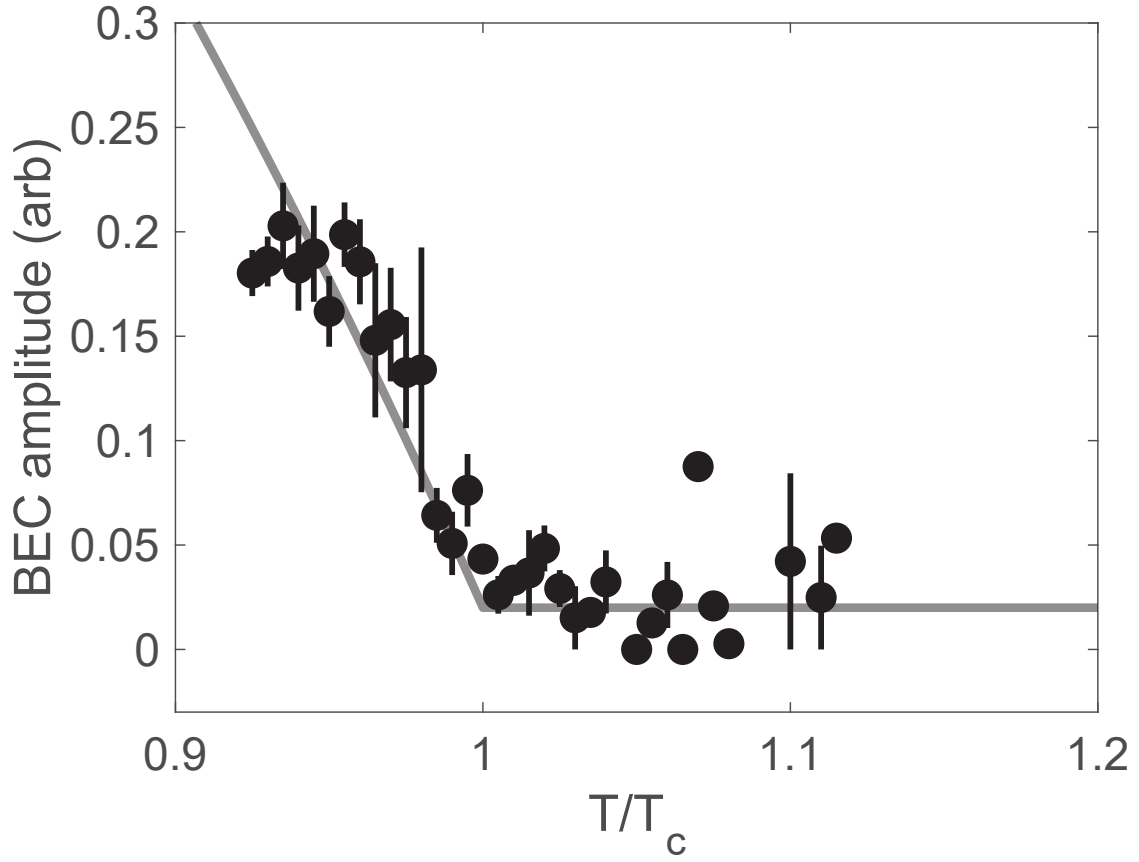


Figure C-6: On set of the BEC amplitudes near condensate transition temperature. The gray curve is a simple theory curve to capture $N_0 = N - CT/T_c$ when temperature is below critical T_c . One Camera count corresponds to 160 atoms.

temperature T_c experimentally instead.

C.2 Fermion atom number

Fermionic ^{40}K number is calibrate to ^{23}Na using a ground state molecules.

Na $|F, mF\rangle = |2, 2\rangle$ has three times more camera counts than Na $|1, 1\rangle$. Therefore each K $|F, mF\rangle = |\frac{9}{2}, -\frac{9}{2}\rangle$ camera count corresponds to $160 \times 3 = 480$ atoms.

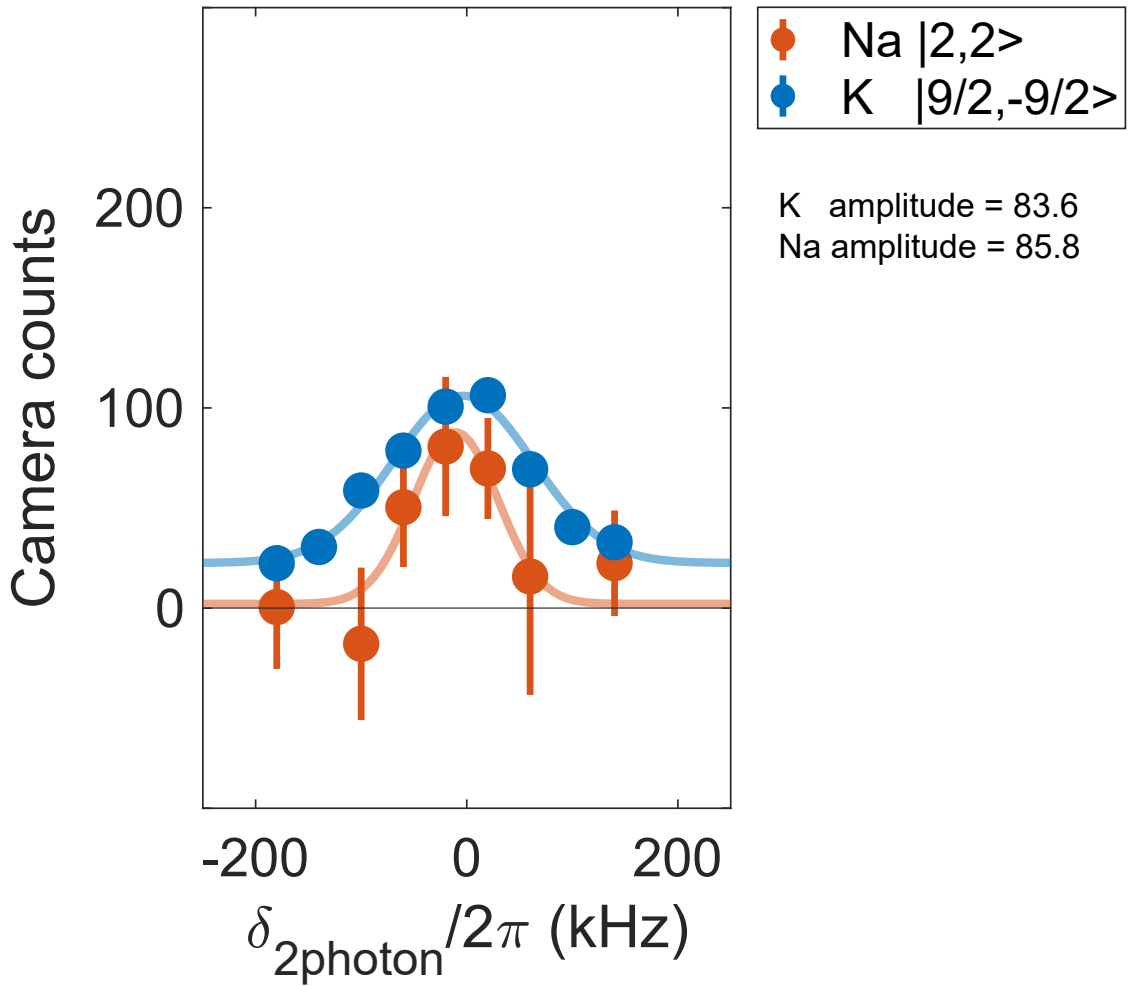


Figure C-7: Calibration fermion and bosons atom number. Blue/orange: fermion/boson camera counts. After Feshbach molecules are associated to ground state molecule, residue atoms are removed by resonant light pulses. Na K atom with 1-to-1 ratio are imaged after ground state molecules are transferred back into atoms. Na are optically pumped to $|F, mF\rangle = |2, 2\rangle$ from $|1, 1\rangle$ for improving imaging signal-to-noise.

C.3 Two component boson density

Two components (thermal n_T and condensed n_C) of BEC density distribution in a harmonic is discussed in detail by Naraschewski and Stamper-Kurn [52]. The con-

densified boson component has a Thomas-Fermi distribution,

$$n_c(z) = B\left(\mu - \frac{1}{2}m\omega_z^2 z^2\right)\Theta\left(\mu - \frac{1}{2}m\omega_z^2 z^2\right) \quad (\text{C.6})$$

Chemical potential μ plays a critical role in determining the BEC distribution. Z is the ‘slow’ trapping axis $\omega_z/2\pi = 9$ Hz. The thermal component distribution is influenced by the condensed boson due to repulsive interaction between Na atoms. Outside of the condensate $z > z_{TF} = \sqrt{\frac{2\mu}{m\omega_z^2}}$, thermal component has a Gaussian-like distribution; inside of the condensate $z < z_{TF}$, the thermal component density is suppressed by the condensate component. In the self-consistent two component boson solution, the thermal boson has density distribution

$$n_T(z) = \frac{1}{\lambda_T} g_{3/2}(e^{-|\frac{1}{2}m\omega_z^2 z^2 - \mu|/k_B T}) \quad (\text{C.7})$$

$g_{3/2}$ is the polylog function (Bose function), λ_T is the de Broglie wavelength. n_T has the highest density at Thomas-Fermi radius $z = z_{TF}$. Fig. C-8 shows a exemplary two component boson density distribution.

C.4 Local density analysis

We use local density analysis to extract density dependent contact and lifetime. Local density analysis (LDA) enables us slice the BEC density at different locations. LDA is valid as long as the thermalization time scale $t_{thermal}$ is much shorter than the trap time dynamics $\propto 1/\omega_{ho}$. Most experiments conducted in this thesis analyze integrated linedensity where we look at the slow trapping axis z spatial property in detail. Given typical z trapping frequency $\omega_z = (2\pi)9$ Hz, experiment time $t \ll 2\pi/\omega_z = 10$ ms makes LDA valid. Inter-boson distance sets the second time scale criteria for LDA, which governs how fast the mixture thermalizes between bosons and fermions. This thermalization time is inverse proportional to degenerate boson energy $t_{thermal} \approx 1/E_n$. Therefore, valid LDA requires both $t \ll t_{thermal}$ and $t \ll 2\pi/\omega_z$.

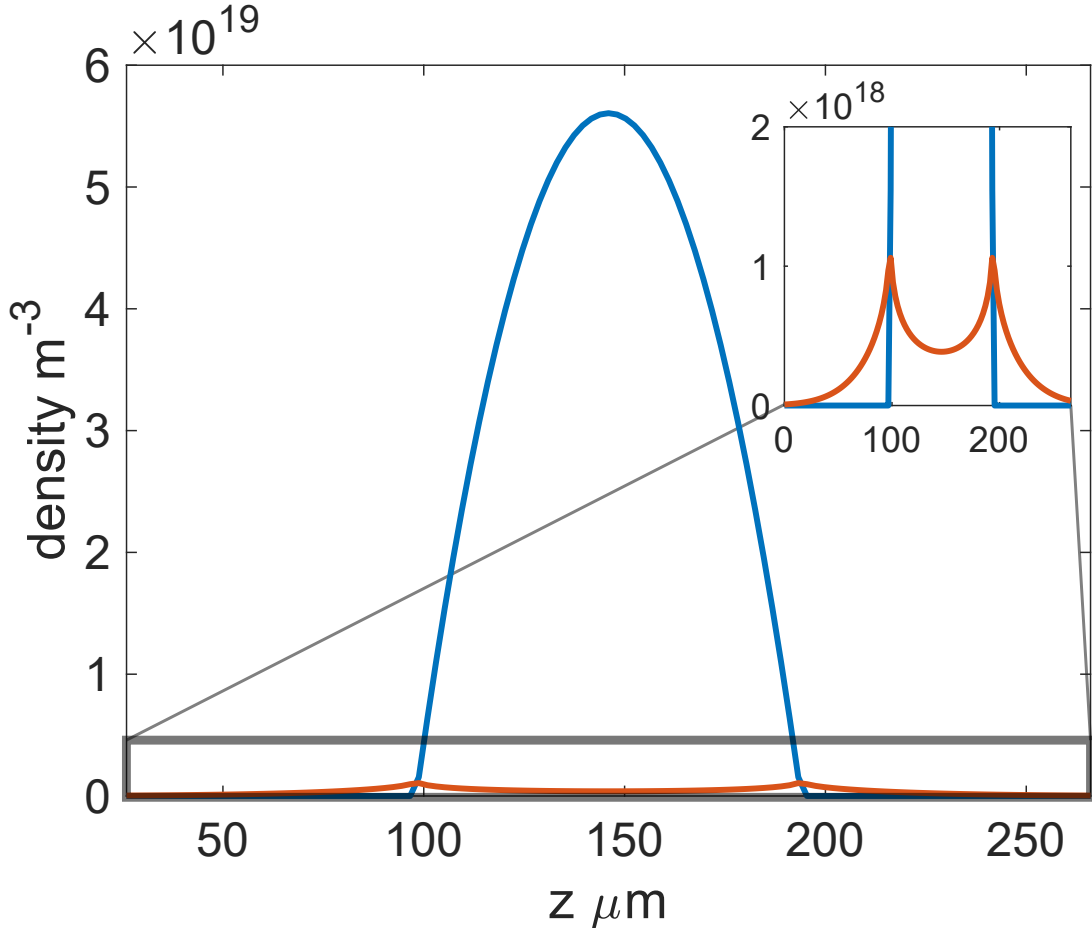


Figure C-8: Two component boson density distributions. Blue: condensed component n_C . Orange: thermal component n_T . The inset shows thermal boson has the highest density at Thomas-Fermi radius where the condensate components starts to emerge.

C.5 Thermal boson line density

We present a fit model for pure thermal boson ($T/T_c > 1$) density distributions. A simple Gaussian fit is compared with a proper Bose function that is derived from Bose statistics. In [52] the proper Bose function n_T to describes a thermal boson density as

$$n_T(z) = \frac{(2\pi)^2}{\lambda_T^5} g_{5/2}(e^{-|\mu - \frac{1}{2}m_B\omega_z^2(z-z_0)^2/(1+\omega_z^2 t_{TOF})|/(k_B T)}) \quad (\text{C.8})$$

We take in-situ images as an example in this chapter, thus $t_{TOF} = 0$.

$$n_T(z) = \frac{(2\pi)^2}{\lambda_T^5} g_{5/2}(e^{-|\mu - \frac{1}{2}m_B\omega_z^2(z-z_0)^2|/(k_B T)}) \quad (\text{C.9})$$

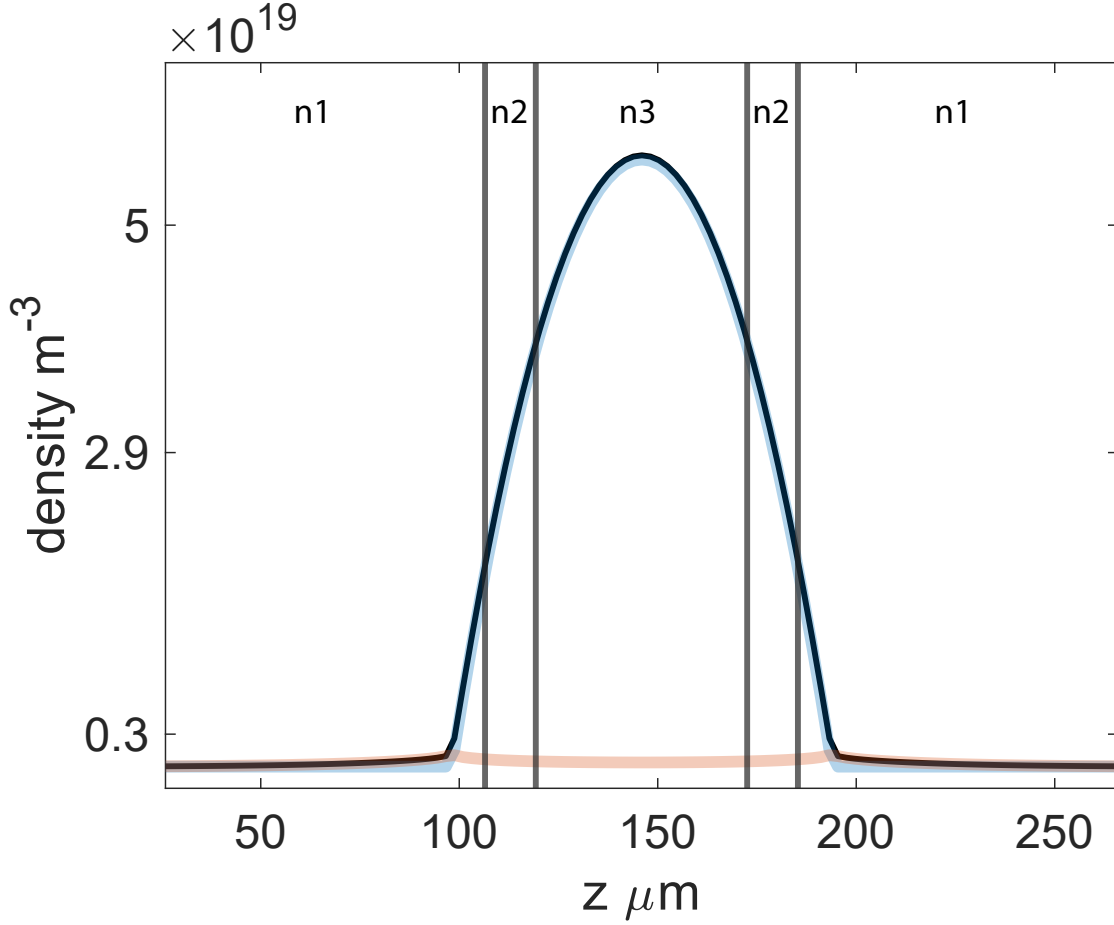


Figure C-9: Three local density slices. Gray vertical lines separates three boson regions density regions $n_1, n_2, n_3 \approx 0.3, 2.9, 5 \times 10^{19} \text{ m}^{-3}$, which are label on the left y-axis. Black solid line marks the sum of thermal (orange) and condensate (blue) density.

Eqn. C.9 is an integrated form of Eqn. C.7. Another integration of $n_T z$ gives us the total number of thermal bosons. Given the calibrated camera counts, we can get the peak thermal boson density,

$$N_{boson} = \int_{z=-\infty}^{\infty} n_T(z) dz = N_{cam} * C_{conversion} \quad (\text{C.10})$$

C.6 Thermal boson column density

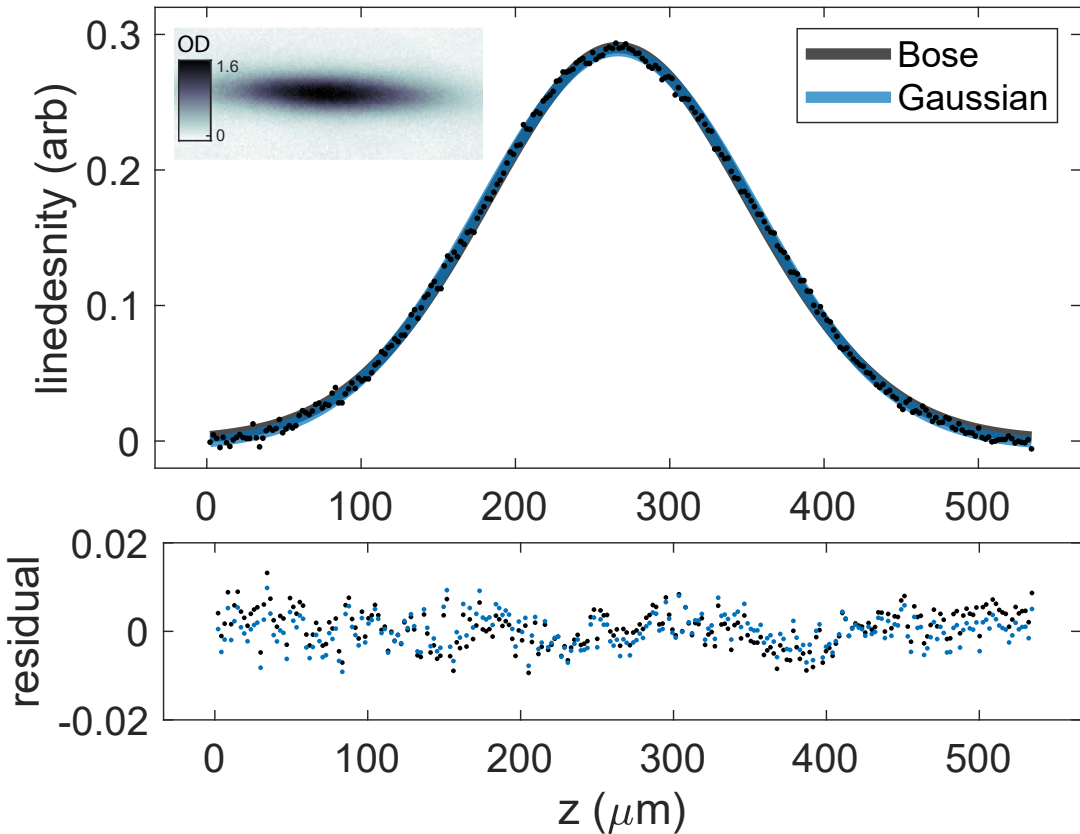


Figure C-10: Thermal boson density distribution. Inset shows the OD image of 50 averages of thermal boson shots. Bose function fit (blue line) shows a good agreement with a simple Gaussian fit (gray line). The fitted chemical potential $\mu/h = -1.1$ kHz, with temperature $T = 71$ nK.

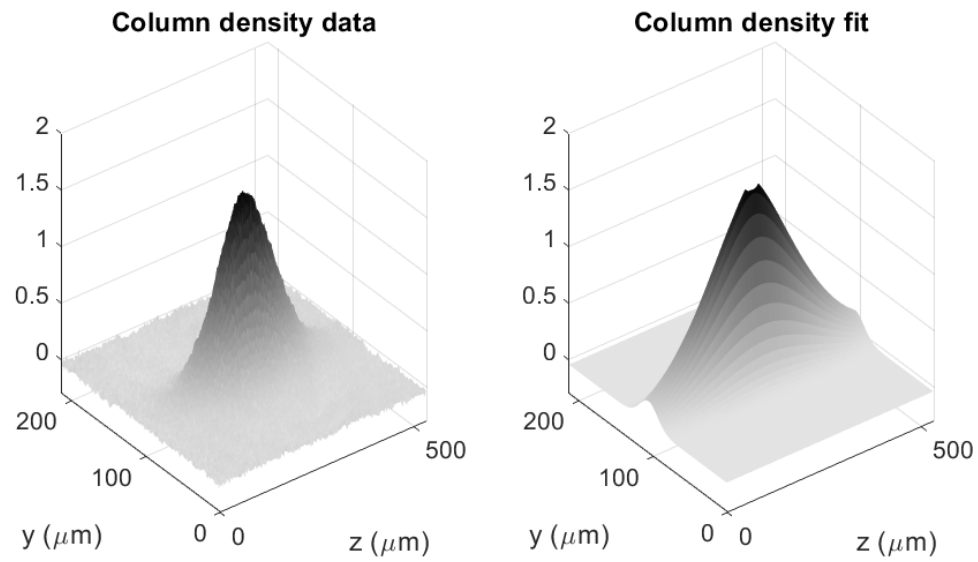


Figure C-11:

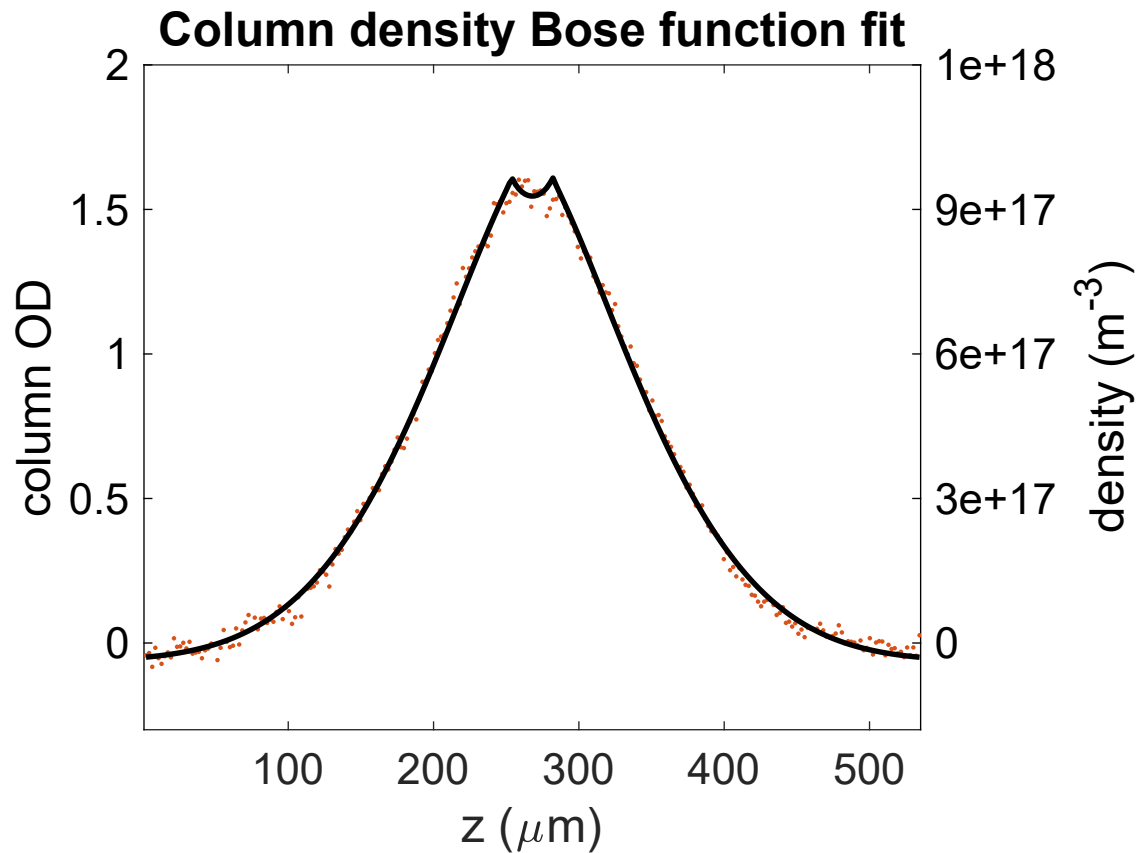


Figure C-12:

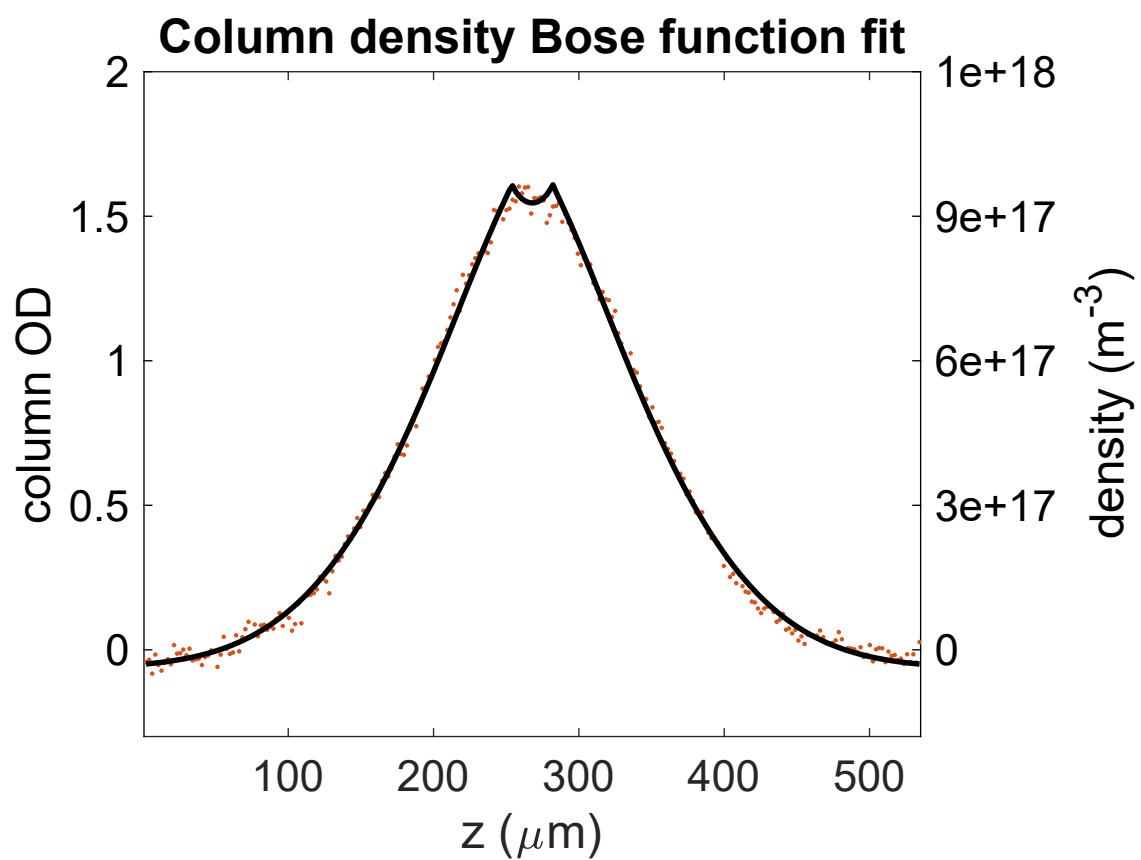


Figure C-13:

Bibliography

- [1] A degenerate Fermi gas of polar molecules. *Science*, 363(6429):853–856, feb 2019.
- [2] Loïc Anderegg, Benjamin L Augenbraun, Yicheng Bao, Sean Burchesky, Lawrence W Cheuk, Wolfgang Ketterle, and John M Doyle. Laser cooling of optically trapped molecules. *Nature Physics*, 14(9):890–893, 2018.
- [3] Loïc Anderegg, Sean Burchesky, Yicheng Bao, Scarlett S Yu, Tijs Karman, Eu-nmi Chae, Kang-Kuen Ni, Wolfgang Ketterle, and John M Doyle. Observation of microwave shielding of ultracold molecules. *Science*, 373(6556):779–782, 2021.
- [4] J. Bardeen, L. N. Cooper, and J. R. Schrieffer. Microscopic theory of superconductivity. *Phys. Rev.*, 106:162–164, Apr 1957.
- [5] Roman Bause, Akira Kamijo, Xing-Yan Chen, Marcel Duda, Andreas Schindewolf, Immanuel Bloch, and Xin-Yu Luo. Efficient conversion of closed-channel-dominated feshbach molecules of ^{23}Na to their absolute ground state. *Physical Review A*, 104(4):043321, 2021.
- [6] Roman Bause, Akira Kamijo, Xing Yan Chen, Marcel Duda, Andreas Schindewolf, Immanuel Bloch, and Xin Yu Luo. Efficient conversion of closed-channel-dominated Feshbach molecules of ^{40}K to their absolute ground state. *Physical Review A*, 104(4):1–9, 2021.
- [7] K Bergmann, H Theuer, and BW Shore. Coherent population transfer among quantum states of atoms and molecules. *Reviews of Modern Physics*, 70(3):1003, 1998.
- [8] Immanuel Bloch, Jean Dalibard, and Wilhelm Zwerger. Many-body physics with ultracold gases. *Reviews of modern physics*, 80(3):885, 2008.
- [9] John L. Bohn and P. S. Julienne. Semianalytic theory of laser-assisted resonant cold collisions. *Physical Review A - Atomic, Molecular, and Optical Physics*, 60(1):414–425, 1999.
- [10] John L Bohn, Ana Maria Rey, and Jun Ye. Cold molecules: Progress in quantum engineering of chemistry and quantum matter. *Science*, 357(6355):1002–1010, 2017.

- [11] K-J Boller, A Imamoğlu, and Stephen E Harris. Observation of electromagnetically induced transparency. *Physical Review Letters*, 66(20):2593, 1991.
- [12] Hans Peter Büchler, Eugene Demler, Mikhail Lukin, Andrea Micheli, N Prokof'Ev, Guido Pupillo, and Peter Zoller. Strongly correlated 2d quantum phases with cold polar molecules: controlling the shape of the interaction potential. *Physical Review Letters*, 98(6):060404, 2007.
- [13] Jin Cao, Huan Yang, Zhen Su, Xin-Yao Wang, Jun Rui, Bo Zhao, and Jian-Wei Pan. Preparation of a quantum degenerate mixture of $^{23}\text{Na}^{40}\text{K}$ molecules and ^{40}K atoms. *Arxiv preprint*, pages 1–6, 2022.
- [14] Jin Cao, Huan Yang, Zhen Su, Xin-Yao Wang, Jun Rui, Bo Zhao, and Jian-Wei Pan. Preparation of a quantum degenerate mixture of $^{23}\text{Na}^{40}\text{K}$ molecules and ^{40}K atoms. *Phys. Rev. A*, 107:013307, Jan 2023.
- [15] Lincoln D Carr, David DeMille, Roman V Krems, and Jun Ye. Cold and ultracold molecules: science, technology and applications. *New Journal of Physics*, 11(5):055049, 2009.
- [16] J. Catani, G. Lamporesi, D. Naik, M. Gring, M. Inguscio, F. Minardi, A. Kantian, and T. Gihamarchi. Quantum dynamics of impurities in a one-dimensional bose gas. *Phys. Rev. A*, 85:023623, Feb 2012.
- [17] Marko Cetina, Michael Jag, Rianne S. Lous, Isabella Fritzsche, Jook T.M. Walraven, Rudolf Grimm, Jesper Levinsen, Meera M. Parish, Richard Schmidt, Michael Knap, and Eugene Demler. Ultrafast many-body interferometry of impurities coupled to a Fermi sea. *Science*, 354(6308):96–99, 2016.
- [18] Xing-Yan Chen, Marcel Duda, Andreas Schindewolf, Roman Bause, Immanuel Bloch, and Xin-Yu Luo. Suppression of unitary three-body loss in a degenerate bose-fermi mixture. *Physical Review Letters*, 128(15):153401, 2022.
- [19] Frédéric Chevy. Universal phase diagram of a strongly interacting fermi gas with unbalanced spin populations. *Physical Review A*, 74(6):063628, 2006.
- [20] Cheng Chin, Rudolf Grimm, Paul Julienne, and Eite Tiesinga. Feshbach resonances in ultracold gases. *Reviews of Modern Physics*, 82(2):1225, 2010.
- [21] Rasmus Søgaard Christensen, Jesper Levinsen, and Georg M. Bruun. Quasiparticle properties of a mobile impurity in a bose-einstein condensate. *Phys. Rev. Lett.*, 115:160401, Oct 2015.
- [22] Franco Dalfovo, Stefano Giorgini, Lev P. Pitaevskii, and Sandro Stringari. Theory of bose-einstein condensation in trapped gases. *Rev. Mod. Phys.*, 71:463–512, Apr 1999.
- [23] David DeMille. Quantum computation with trapped polar molecules. *Physical Review Letters*, 88(6):067901, 2002.

- [24] B. J. DeSalvo, Krutik Patel, Jacob Johansen, and Cheng Chin. Observation of a Degenerate Fermi Gas Trapped by a Bose-Einstein Condensate. *Phys. Rev. Lett.*, 119(23):233401, 2017.
- [25] Gianni Di Domenico, Stéphane Schiltz, and Pierre Thomann. Simple approach to the relation between laser frequency noise and laser line shape. *Applied optics*, 49(25):4801–4807, 2010.
- [26] J. P. D’Incao and B. D. Esry. Scattering length scaling laws for ultracold three-body collisions. *Phys. Rev. Lett.*, 94:213201, Jun 2005.
- [27] J. P. D’Incao and B. D. Esry. Suppression of molecular decay in ultracold gases without fermi statistics. *Phys. Rev. Lett.*, 100:163201, Apr 2008.
- [28] Ronald WP Drever, John L Hall, Frank V Kowalski, James Hough, GM Ford, AJ Munley, and H Ward. Laser phase and frequency stabilization using an optical resonator. *Applied Physics B*, 31:97–105, 1983.
- [29] Marcel Duda, Xing-Yan Chen, Andreas Schindewolf, Roman Bause, Jonas von Milczewski, Richard Schmidt, Immanuel Bloch, and Xin-Yu Luo. Transition from a polaronic condensate to a degenerate Fermi gas of heteronuclear molecules. *Arxiv preprint*, pages 1–12, 2021.
- [30] Vitaly Efimov. Energy levels arising from resonant two-body forces in a three-body system. *Physics Letters B*, 33(8):563–564, 1970.
- [31] PO Fedichev, MW Reynolds, and GV Shlyapnikov. Three-body recombination of ultracold atoms to a weakly bound s level. *Physical review letters*, 77(14):2921, 1996.
- [32] Enrico Fermi et al. Motion of neutrons in hydrogenous substances. *Ricerca Scientifica*, 7(2):13–52, 1936.
- [33] Michael Fleischhauer, Atac Imamoglu, and Jonathan P Marangos. Electromagnetically induced transparency: Optics in coherent media. *Reviews of modern physics*, 77(2):633, 2005.
- [34] James Franck and EG Dymond. Elementary processes of photochemical reactions. *Transactions of the Faraday Society*, 21(February):536–542, 1926.
- [35] Alexander L. Gaunt, Tobias F. Schmidutz, Igor Gotlibovich, Robert P. Smith, and Zoran Hadzibabic. Bose-einstein condensation of atoms in a uniform potential. *Phys. Rev. Lett.*, 110:200406, May 2013.
- [36] Chris H Greene, P Giannakeas, and J Pérez-Ríos. Universal few-body physics and cluster formation. *Reviews of Modern Physics*, 89(3):035006, 2017.
- [37] F. Grusdt, Y. E. Shchadilova, A. N. Rubtsov, and E. Demler. Renormalization group approach to the Fr??hlich polaron model: Application to impurity-BEC problem. *Sci. Rep.*, 5, 2015.

- [38] Fabian Grusdt, Richard Schmidt, Yulia E Shchadilova, and E Demler. Strong-coupling bose polarons in a bose-einstein condensate. *Physical Review A*, 96(1):013607, 2017.
- [39] K Helfrich, H-W Hammer, and DS Petrov. Three-body problem in heteronuclear mixtures with resonant interspecies interaction. *Physical Review A*, 81(4):042715, 2010.
- [40] Ming-Guang Hu, Michael J. Van de Graaff, Dhruv Kedar, John P. Corson, Eric A. Cornell, and Deborah S. Jin. Bose polarons in the strongly interacting regime. *Phys. Rev. Lett.*, 117:055301, Jul 2016.
- [41] Nicholas R Hutzler, Hsin-I Lu, and John M Doyle. The buffer gas beam: An intense, cold, and slow source for atoms and molecules. *Chemical reviews*, 112(9):4803–4827, 2012.
- [42] Kevin M Jones, Eite Tiesinga, Paul D Lett, and Paul S Julienne. Ultracold photoassociation spectroscopy: Long-range molecules and atomic scattering. *Reviews of Modern Physics*, 78(2):483, 2006.
- [43] M. Junker, D. Dries, C. Welford, J. Hitchcock, Y. P. Chen, and R. G. Hulet. Photoassociation of a Bose-Einstein condensate near a feshbach resonance. *Physical Review Letters*, 101(6):1–4, 2008.
- [44] C. Kohstall, M. Zaccanti, M. Jag, A. Trenkwalder, P. Massignan, G. M. Bruun, F. Schreck, and R. Grimm. Metastability and coherence of repulsive polarons in a strongly interacting Fermi mixture. *Nature*, 485(7400):615–618, 2012.
- [45] Marco Koschorreck, Daniel Pertot, Enrico Vogt, Bernd Fröhlich, Michael Feld, and Michael Köhl. Attractive and repulsive Fermi polarons in two dimensions. *Nature*, 485(7400):619–622, 2012.
- [46] L. D. Landau. *Phys. Z. Sowjetunion*, 3:644, 1933.
- [47] Mikhail Lemeshko. Quasiparticle approach to molecules interacting with quantum solvents. *Phys. Rev. Lett.*, 118:095301, Feb 2017.
- [48] Mikhail Lemeshko and Richard Schmidt. Molecular impurities interacting with a many-particle environment: from ultracold gases to helium nanodroplets. In *Cold Chemistry: Molecular Scattering and Reactivity Near Absolute Zero*, volume 11. Royal Society of Chemistry, 2017.
- [49] Weiran Li and S. Das Sarma. Variational study of polarons in bose-einstein condensates. *Phys. Rev. A*, 90:013618, Jul 2014.
- [50] Lan Liu, De-Chao Zhang, Huan Yang, Ya-Xiong Liu, Jue Nan, Jun Rui, Bo Zhao, and Jian-Wei Pan. Observation of interference between resonant and detuned stirraps in the adiabatic creation of $^{23}\text{Na}^{40}\text{K}$ molecules. *Phys. Rev. Lett.*, 122:253201, Jun 2019.

- [51] Andrew D Ludlow, Martin M Boyd, Jun Ye, Ekkehard Peik, and Piet O Schmidt. Optical atomic clocks. *Reviews of Modern Physics*, 87(2):637, 2015.
- [52] M. Naraschewski and D. M. Stamper-Kurn. Analytical description of a trapped semi-ideal bose gas at finite temperature. *Phys. Rev. A*, 58:2423–2426, Sep 1998.
- [53] S. Nascimbène, N. Navon, K. J. Jiang, L. Tarruell, M. Teichmann, J. McKeeever, F. Chevy, and C. Salomon. Collective oscillations of an imbalanced fermi gas: Axial compression modes and polaron effective mass. *Phys. Rev. Lett.*, 103(17):170402, 2009.
- [54] K.-K Ni, S Ospelkaus, M H G De Miranda, A Pe'er, B Neyenhuis, J J Zirbel, S Kotochigova, P S Julienne, D S Jin, and J Ye. A high phase-space-density gas of polar molecules. *Science*, 322(5899):231–235, 2008.
- [55] S Ospelkaus, K-K Ni, D Wang, MHG De Miranda, B Neyenhuis, 1 G Quéméner, PS Julienne, JL Bohn, DS Jin, and J Ye. Quantum-state controlled chemical reactions of ultracold potassium-rubidium molecules. *science*, 327(5967):853–857, 2010.
- [56] Jee Woo Park, Sebastian A Will, and Martin W Zwierlein. Two-photon pathway to ultracold ground state molecules of $^{23}\text{Na}^{40}\text{K}$. *New Journal of Physics*, 17(7):075016, jul 2015.
- [57] Jee Woo Park, Sebastian A Will, and Martin W Zwierlein. Ultracold dipolar gas of fermionic ^{23}Na ^{40}K molecules in their absolute ground state. *Physical review letters*, 114(20):205302, 2015.
- [58] Jee Woo Park, Cheng-Hsun Wu, Ibon Santiago, Tobias G. Tiecke, Sebastian Will, Peyman Ahmadi, and Martin W. Zwierlein. Quantum degenerate bose-fermi mixture of chemically different atomic species with widely tunable interactions. *Phys. Rev. A*, 85:051602, May 2012.
- [59] Juliana J Park, Yu-Kun Lu, Alan O Jamison, Timur V Tscherbul, and Wolfgang Ketterle. A feshbach resonance in collisions between triplet ground-state molecules. *Nature*, 614(7946):54–58, 2023.
- [60] G. B. Partridge, K. E. Strecker, R. I. Kamar, M. W. Jack, and R. G. Hulet. Molecular probe of pairing in the BEC-BCS crossover. *Physical Review Letters*, 95(2):8–11, 2005.
- [61] S. I. Pekar. *Zh. Eksp. Teor. Fiz.*, 16:341, 1946.
- [62] DS Petrov and Felix Werner. Three-body recombination in heteronuclear mixtures at finite temperature. *Physical Review A*, 92(2):022704, 2015.
- [63] Ionut D. Prodan, Marin Pichler, Mark Junker, Randall G. Hulet, and John L. Bohn. Intensity dependence of photoassociation in a quantum degenerate atomic gas. *Phys. Rev. Lett.*, 91:080402, Aug 2003.

- [64] Steffen Patrick Rath and Richard Schmidt. Field-theoretical study of the Bose polaron. *Phys. Rev. A*, 88(5):053632, 2013.
- [65] T. Rentrop, A. Trautmann, F. A. Olivares, F. Jendrzejewski, A. Komnik, and M. K. Oberthaler. Observation of the phononic lamb shift with a synthetic vacuum. *Phys. Rev. X*, 6:041041, Nov 2016.
- [66] F. Scazza, G. Valtolina, P. Massignan, A. Recati, A. Amico, A. Burchianti, C. Fort, M. Inguscio, M. Zaccanti, and G. Roati. Repulsive Fermi Polarons in a Resonant Mixture of Ultracold Li 6 Atoms. *Phys. Rev. Lett.*, 118(8):083602, 2017.
- [67] André Schirotzek, Cheng Hsun Wu, Ariel Sommer, and Martin W. Zwierlein. Observation of fermi polarons in a tunable fermi liquid of ultracold atoms. *Phys. Rev. Lett.*, 102(23):230402, 2009.
- [68] Richard Schmidt and Mikhail Lemeshko. Rotation of quantum impurities in the presence of a many-body environment. *Phys. Rev. Lett.*, 114:203001, May 2015.
- [69] Richard Schmidt and Mikhail Lemeshko. Deformation of a quantum many-particle system by a rotating impurity. *Phys. Rev. X*, 6:011012, Feb 2016.
- [70] Yulia E. Shchadilova, Richard Schmidt, Fabian Grusdt, and Eugene Demler. Quantum dynamics of ultracold Bose polarons. *Phys. Rev. Lett.*, 117(11):113002, apr 2016.
- [71] Hyungmok Son, Juliana J Park, Yu-Kun Lu, Alan O Jamison, Tijs Karman, and Wolfgang Ketterle. Control of reactive collisions by quantum interference. *Science*, 375(6584):1006–1010, 2022.
- [72] Hyungmok Son, Juliana J Park, Yu-kun Lu, Alan O Jamison, Tijs Karman, and Wolfgang Ketterle. Control of reactive collisions by quantum interference. *Science*, 375(6584):1006–1010, mar 2022.
- [73] Benjamin K Stuhl, Matthew T Hummon, Mark Yeo, Goulven Quéméner, John L Bohn, and Jun Ye. Evaporative cooling of the dipolar hydroxyl radical. *Nature*, 492(7429):396–400, 2012.
- [74] Benjamin K Stuhl, Brian C Sawyer, Dajun Wang, and Jun Ye. Magneto-optical trap for polar molecules. *Physical review letters*, 101(24):243002, 2008.
- [75] Levente Szasz and George McGinn. Atomic and molecular calculations with the pseudopotential method. i. the binding energy and equilibrium internuclear distance of the na2 molecule. *The Journal of Chemical Physics*, 45(8):2898–2912, 1966.
- [76] Shina Tan. Energetics of a strongly correlated fermi gas. *Annals of Physics*, 323(12):2952–2970, 2008.

- [77] J. Tempere, W. Casteels, M. K. Oberthaler, S. Knoop, E. Timmermans, and J. T. Devreese. Feynman path-integral treatment of the BEC-impurity polaron. *Phys. Rev. B*, 80(18):184504, 2009.
- [78] J Peter Toennies and Andrey F Vilesov. Superfluid helium droplets: a uniquely cold nanomatrix for molecules and molecular complexes. *Angewandte Chemie International Edition*, 43(20):2622–2648, 2004.
- [79] KK Verma, JT Bahns, AR Rajaei-Rizi, William C Stwalley, and WT Zemke. First observation of bound–continuum transitions in the laser-induced a $1\sigma+$ u–x $1\sigma+$ g fluorescence of na₂. *The Journal of Chemical Physics*, 78(6):3599–3613, 1983.
- [80] Jonas Vlietinck, Wim Casteels, Kris Van Houcke, Jacques Tempere, Jan Ryckebusch, and Jozef T Devreese. Diagrammatic monte carlo study of the acoustic and the bose–einstein condensate polaron. *New Journal of Physics*, 17(3):033023, 2015.
- [81] Vladan Vuletić, Andrew J Kerman, Cheng Chin, and Steven Chu. Observation of low-field feshbach resonances in collisions of cesium atoms. *Physical review letters*, 82(7):1406, 1999.
- [82] F. Werner, L. Tarruell, and Y. Castin. Number of closed-channel molecules in the BEC-BCS crossover. *European Physical Journal B*, 68(3):401–415, 2009.
- [83] Cheng-Hsun Wu, Jee Woo Park, Peyman Ahmadi, Sebastian Will, and Martin W Zwierlein. Ultracold fermionic feshbach molecules of na 23 k 40. *Physical review letters*, 109(8):085301, 2012.
- [84] Cheng Hsun Wu, Jee Woo Park, Peyman Ahmadi, Sebastian Will, and Martin W. Zwierlein. Ultracold fermionic Feshbach molecules of Na23K40. *Phys. Rev. Lett.*, 109(8):085301, 2012.
- [85] Xin Xie, Michael J Van de Graaff, Roman Chapurin, Matthew D Frye, Jeremy M Hutson, José P D’Incao, Paul S Julienne, Jun Ye, and Eric A Cornell. Observation of efimov universality across a nonuniversal feshbach resonance in k 39. *Physical Review Letters*, 125(24):243401, 2020.
- [86] Zhenjie Yan, Parth B. Patel, Biswaroop Mukherjee, Richard J. Fletcher, Julian Struck, and Martin W. Zwierlein. Boiling a Unitary Fermi Liquid. *Phys. Rev. Lett.*, 122(9):093401, 2019.
- [87] Zoe Z. Yan, Yiqi Ni, Carsten Robens, and Martin W. Zwierlein. Bose polarons near quantum criticality. *Science*, 368(6487):190–194, 2020.
- [88] Huan Yang, De-Chao Zhang, Lan Liu, Ya-Xiong Liu, Jue Nan, Bo Zhao, and Jian-Wei Pan. Observation of magnetically tunable feshbach resonances in ultracold 23na40k+ 40k collisions. *Science*, 363(6424):261–264, 2019.

- [89] LP Yatsenko, BW Shore, and K Bergmann. Detrimental consequences of small rapid laser fluctuations on stimulated raman adiabatic passage. *Physical Review A*, 89(1):013831, 2014.
- [90] Shuhei M. Yoshida, Shimpei Endo, Jesper Levinsen, and Meera M. Parish. Universality of an impurity in a bose-einstein condensate. *Phys. Rev. X*, 8:011024, Feb 2018.
- [91] Hui Zhai. *Ultracold Atomic Physics*. Cambridge University Press, feb 2021.